Nonlinear Mechanics of MEMS Rectangular Microplates under Electrostatic Actuation

Dissertation by

Shahid Saghir

In Partial Fulfillment of the Requirements

For the Degree of

Doctor of Philosophy

King Abdullah University of Science and Technology, Thuwal,

Kingdom of Saudi Arabia

The dissertation of Shahid Saghir is approved by the examination committee

Committee Member: Prof. Stefano Lenci

Committee Member: Prof. Taous Meriem Laleg

Committee Member: Prof. Mohammad I. Younis

Committee Chairperson: Prof. Sigurdur Thoroddsen

ABSTRACT

Nonlinear Mechanics of MEMS Rectangular Microplates under Electrostatic Actuation

Shahid Saghir

The first objective of the dissertation is to develop a suitable reduced order model capable of investigating the nonlinear mechanical behavior of von-Karman plates under electrostatic actuation. The second objective is to investigate the nonlinear static and dynamic behavior of rectangular microplates under small and large actuating forces.

In the first part, we present and compare various approaches to develop reduced order models for the nonlinear von-Karman rectangular microplates actuated by nonlinear electrostatic forces. The reduced-order models aim to investigate the static and dynamic behavior of the plate under small and large actuation forces. A fully clamped microplate is considered. Different types of basis functions are used in conjunction with the Galerkin method to discretize the governing equations. First we investigate the convergence with the number of modes retained in the model. Then for validation purpose, a comparison of the static results is made with the results calculated by a nonlinear finite element model. The linear eigenvalue problem for the plate under the electrostatic force is solved for a wide range of voltages up to pull-in.

In the second part, we present an investigation of the static and dynamic behavior of a fully clamped microplate. We investigate the effect of different non-dimensional design

parameters on the static response. The forced-vibration response of the plate is then investigated when the plate is excited by a harmonic AC load superimposed to a DC load. The dynamic behavior is examined near the primary and secondary (superharmonic and subharmonic) resonances. The microplate shows a strong hardening behavior due to the cubic nonlinearity of midplane stretching. However, the behavior switches to softening as the DC load is increased. Next, near-square plates are studied to understand the effect of geometric imperfections of microplates.

In the final part of the dissertation, we investigate the mechanical behavior of initially curved microplates. Microplates often experience an initial curvature imperfection, due to the micro fabrication process, which affects significantly their mechanical behavior. In this case a clamped-free-clamped-free microplate is considered. We validate the reduced order model by comparing the calculated static behavior and the fundamental natural frequency with those computed by a finite element model. As case studies, we consider two commonly encountered profiles of the initial curvature imperfection and study their effects on both the static and dynamic responses of the microplates.

Next, an initially curved microplate made of silicon nitride is studied. The static behaviour of the microplate is investigated when applying a DC voltage. Then, the dynamic behaviour of the microplate is examined under the application of a harmonic AC voltage, superimposed to a DC voltage. Simulation results calculated by the reduced order model are compared with experimental data for model validation purpose, which show good agreement.

DEDICATION

To my parents, Hameeda Bibi and Muhammad Shafi (Late)

To my wife Atika and our daughters Shehar, Mehar, and Jannat.

ACKNOWLEDGMENTS

I would like to take this opportunity to express my deep gratitude and thanks to King Abdullah (late), the benefactor, who founded this beacon of hope (KAUST) on the shores of Red Sea, which has provided me with the best research facilities and conducive environment to pursue my higher studies and conduct PhD research.

I'm deeply obliged to my PhD advisor Prof. Mohammad Ibrahim Younis, who has supported me greatly to conduct PhD research and teach me complex ideas with great patience and kindness. He has been a source of endless encouragement and support to advance my research and academic skills to highest level. Indeed I feel blessed to be his student and work with him. Through all these years he has been a great teacher, a kind advisor, and a good friend.

I would like to thank my committee members Prof. Sigurdur Thoroddsen, Prof. Taous Meriem, and Prof. Stefano Lenci, for their support and encouragement. I also participated in the courses taught by Prof. Meriem and Prof. Siggi, which greatly helped me develop my academic skills. My special thanks go to Prof. Ali H. Nayfeh, who provided me vital help to understand some complex ideas involved in my research.

I'm thankful to my friends and lab colleagues Nizar Jaber, Feras Alfosail, Saad Ilyas, Sherif Tella, and Amal Hajjaj for their sincere friendship and support. I highly appreciate the help and support from Saad Ilyas and Nizar Jaber to conduct the experimental work. I greatly appreciate the fruitful discussions with Feras Alfosail and Sherif Tella to understand complex ideas. My thanks also go to Dr. Abdallah Ramini, Dr. Mohammed L.

Bellaredj, Dr. Nouha Alcheikh, Dr. Lakshmoji Kosuru, Dr. Karumbaiah C. Nanaiah, and Dr. Syed Kazmi, for their friendship, support and encouragement. Especially I'm thankful to Dr. Mohammed L. Bellaredj for helping me to complete experimental part of my dissertation research.

My deepest gratitude goes to my parents for believing in me and believing that I deserve better education. My mother has been the greatest source of strength and support for me. I highly appreciate her patience, sacrifice, and prayers for my success. My sincere thanks also go to my sisters, who are source of endless love and support, and to my brothers, who supported me greatly during my higher studies. Finally I would like to deeply thank my wife Atika for her sacrifice, patience, and support. I'm also thankful to my daughters Shehar, Mehar, and Jannat, whose love has been the greatest source of motivation throughout my PhD studies.

TABLE OF CONTENTS

Examination Committee Approval 2
ABSTRACT....3
DEDICATION....5
ACKNOWLEDGMENTS 6
TABLE OF CONTENTS....8
LIST OF FIGURES 11
LIST OF TABLES....15
Chapter 1 Introduction 16
1.1. Introduction and Background 16
1.2. Literature Review....18
1.2.1. Flat Plates....18
1.2.2. Initially Curved Plates....21
1.2.3. Solutions Methods 23
1.3. Dissertation Objectives 23
1.4. Dissertation Contributions 25
1.5. Dissertation Organization 26
Chapter 2 Nonlinear von-Karman Analysis of Thin Plates 28
2.1. Thin Flat Plates 29
2.2. Initially Curved Imperfect Plates 36
Chapter 3 Approaches for Reduced Order Modeling of Electrically Actuated von-Karman Microplates....43
3.1. Introduction....44
3.2. Problem Formulation 44

3.3. Reduced Order Models 48
3.3.1. Model I 49
3.3.2. Model II 50
3.3.3. Model III 51
3.3.4. Model IV 52
3.3.5. Model V 53
3.4. Static Analysis 54
3.5. Model Validation 55
3.6. Dynamic Analysis 59
Chapter 4 An Investigation of the Static and Dynamic Behavior of Electrically Actuated Rectangular Microplates 65
4.1. Introduction 66
4.2. Static Analysis 67
4.3. Dynamic Analysis 68
4.3.1. Primary Resonance 69
4.3.2. Secondary Resonances 72
4.3.3. Dynamic Behavior of Imperfect Square Plates 77
Chapter 5 Initially Curved Micro-plates under Electrostatic Actuation 80
5.1. Introduction 81
5.2. Problem Formulation 81
5.3. Reduced Order Model 84
5.4. Results 86
5.4.1. Static Results 87
5.4.2. Dynamic Results 90
Chapter 6 Initially Curved Microplates under Electrostatic Actuation: Experimental Case Study and Model Validation 95

6.1. Introduction 95

6.2. Experiment 96

6.3. Theory 101

Chapter 7 Summary, Conclusions, and Future Work 106

7.1. Summary and Conclusions 106

7.1.1. Approaches for Reduced Order Modeling of Electrically Actuated von-Karman Microplates 106

7.1.2. An Investigation of the Static and Dynamic Behavior of Electrically Actuated Rectangular Microplates 108

7.1.3. Initially Curved Micro-plates under Electrostatic Actuation 109

7.1.4. Initially Curved Microplates under Electrostatic Actuation: Experimental Case Study and Model Validation 110

7.2. Future Work Directions 110

REFERENCES 113

APPENDIX 119

LIST OF FIGURES

Figure 2.1: A schematic diagram of an electrostatically actuated thin microplate. 29

Figure 2.2: A schematic diagram of an electrically actuated initially curved clamped-free-clamped-free microplate. 37

Figure 3.1: A schematic diagram of an electrically actuated fully clamped microplate... 44

Figure 3.2: Convergence of the static results with the number of transversal mode shapes retained in the reduced order models. Variation of the maximum non-dimensional deflection $W_{\max}$ at the center of the microplate with the electrostatic voltage parameter $\alpha_2 V_{dc}^{\ 2}$ when $\alpha = 1$, and $\alpha_1 = 1$: (a) model I, (b) model II, (c) model III, (d) model IV, (e) model V..... 57

Figure 3.3: A comparison of the maximum deflection $W_{\max}$ at the center of the plate, calculated by the reduced order models with the results obtained from FE model implemented in COMSOL for various values of V_{dc}, until the pull-in instability: (a) model I, (b) model II, (c) model III, (d) model IV, (e) model V. 58

Figure 3.4: The non-dimensional fundamental natural frequency ($\lambda = \omega a^2 \sqrt{\frac{\rho}{D}}$) of a square microplate for different levels of V_{dc} until pull-in (stars). Comparison with the results computed by the FE model implemented in COMSOL (diamonds): (a) model II, (b) model III, (c) model IV, (d) model V..... 60

Figure 3.5: Frequency response curves near the non-dimensional fundamental natural frequency, maximum non-dimensional deflection $W_{\max}\left(a/2, b/2\right)$ of the microplate against actuating frequency Ω. Response is captured at $V_{dc} = 1\text{V}$ and (a) $V_{ac} = 0.01\text{V}$, (b) $V_{ac} = 1\text{V}$, when $\alpha = 1$, $\alpha_1 = 1, \alpha_2 = 1$ and a quality factor $Q = 1000$. 62

Figure 4.1: Variation of the maximum non-dimensional deflection $W_{\max}$ at the center of the microplate with the electrostatic voltage parameter $\alpha_2 V_{dc}^{\ 2}$ until pull-in for various values of aspect ratio α when $\alpha_1 = 1$. 67

Figure 4.2: Variation of the non-dimensional deflection $W_{\max}$ at the center of the microplate with the electrostatic voltage parameter $\alpha_2 V_{dc}^{\ 2}$ until pull-in for various values of α_1 when $\alpha = 1$..... 68

Figure 4.3: Time history response of the microplate. (a) Transient response. (b) Steady state response. 69

Figure 4.4: Maximum non-dimensional deflection $W_{\max}$ at the center of the microplate against the actuating frequency Ω when actuated at $V_{dc} = 3\text{V}$ and various values of V_{ac} while quality factor $Q = 250$; (F) forward frequency sweep, (B) backward frequency sweep..... 70

Figure 4.5: Maximum non-dimensional deflection $W_{\max}$ at the center of the microplate against the actuating frequency Ω when actuated at $V_{dc} = 7\text{V}$ and various values of V_{ac} while quality factor $Q = 250$..... 71

Figure 4.6: Frequency response curves near super-harmonic resonance, $\frac{\omega_1}{3}$ of the fundamental natural frequency. Maximum non-dimensional deflection $W_{\max}$ at the center of the microplate against the actuating frequency Ω when actuated at $V_{dc} = 9\text{V}$ and various values of V_{ac} while quality factor $Q = 250$..... 73

Figure 4.7: Frequency response curves near super-harmonic resonance, $\frac{\omega_1}{3}$ of the fundamental natural frequency. Maximum non-dimensional deflection $W_{\max}$ at the center of the microplate against the actuating frequency Ω when actuated at $V_{dc} = 10\text{V}$ and various values of V_{ac} while quality factor $Q = 250$..... 74

Figure 4.8: Phase portraits for the lower and upper stable branches of the Figure 4.6 for $V_{ac} = 2.3\text{V}$; (a) $\Omega = 11.12$, (b) $\Omega = 11.176$, (c) $\Omega = 11.178$, (d) $\Omega = 11.194$..... 75

Figure 4.9: Phase portraits for the lower and upper stable branches of the Figure 4.6 for $V_{ac} = 2.4\text{V}$; (a) $\Omega = 11.12$, (b) $\Omega = 11.138$, (c) $\Omega = 11.14$, (d) $\Omega = 11.204$..... 76

Figure 4.10: Frequency response curves near sub-harmonic resonance near $2\omega_1$. Maximum non-dimensional deflection $W_{\max}$ at the center of the microplate against the actuating frequency Ω for a quality factor $Q = 250$..... 78

Figure 4.11: Dynamic behavior of an imperfect square plate near the second symmetric-symmetric mode of vibration when actuated at $V_{dc} = 1\text{V}$, $V_{ac} = 0.3\text{V}$ with a quality factor $Q = 1000$..... 79

Figure 5.1: Convergence of the static response with the number of transverse modes retained in the reduced order model. Variation of the maximum non-dimensional deflection $W_{\max}$ at the center of the plate with the electrostatic voltage parameter $\alpha_2 V_{dc}^{\,2}$ when $\alpha = 1$ and $\alpha_1 = 1$..... 88

Figure 5.2: Variation of the DC voltage V_{pull} at pull-in with the initial imperfection calculated by the reduced order model for curvature profiles w_{01} and w_{02}. Results

calculated by the FE model are also compared with the results of the reduced order model for profile w_{01}. 89

Figure 5.3: Variation of the non-dimensional fundamental natural frequency $\omega_{non} = \omega a^2 \sqrt{\frac{\rho}{D}}$ with the initial imperfection $w_{0\max}$. Results calculated by the FE model are also compared with the results of the reduced order model for profile w_{01}. 91

Figure 5.4: Frequency response curves showing the linear responses of the microplate for various values of initial curvature imperfection for profile w_{01} and w_{02} when the microplate is actuated by a $V_{ac} = 1\text{V}$ superimposed to a $V_{dc} = 1\text{V}$, and a quality factor $Q = 1000$ 92

Figure 5.5: Variation of the maximum non-dimensional deflection $W_{\max}$ at the center of the plate with the actuation frequency Ω for various values of initial curvature imperfection for profile w_{01} when $V_{ac} = 5\text{V}$, $V_{dc} = 5\text{V}$, and quality factor $Q = 1000$ ... 93

Figure 5.6: Variation of the maximum non-dimensional deflection $W_{\max}$ at the center of the plate with the actuation frequency Ω for various values of initial curvature imperfection for profile w_{02} when $V_{ac} = 5\text{V}$, $V_{dc} = 5\text{V}$, and quality factor $Q = 1000$ 93

Figure 5.7: Frequency response curves depicting the transition from hardening to softening response of the microplate with increasing V_{dc} with $V_{ac} = 1$. 94

Figure 6.1: (a) Optical microscope view of the fabricated microplate, (b) deflection profile along the length of the microplate, and (c) deflection profile along the width of the microplate. 97

Figure 6.2: Experimental setup showing the Micro-System Analyzer MSA-500, a vacuum chamber, a vacuum pump and data acquisition system DAQ. 98

Figure 6.3: The maximum deflection $W_{\max}$ measured at the center of the microplate against V_{dc} until pull-in, at a 3.3 mTorr chamber pressure. 99

Figure 6.4: The velocity response of the microplate to the white noise actuation signal at V_{dc}=5V, V_{ac}=10V and 3.3 mTorr chamber pressure. 99

Figure 6.5: Frequency response plots in the neighborhood of the fundamental natural frequency of the microplate at various combinations of applied loads at a 3.3 mTorr chamber pressure. 100

Figure 6.6: Plots of the assumed profile passing through the center of the microplate, (a) along the length of the microplate, (b) along the width of the microplate..... 102

Figure 6.7: The maximum deflection $W_{\max}$ at the center of the microplate against V_{dc} until the pull-in; calculated by the reduced order model accounting for initial curvature and measured experimentally. Results calculated by reduced order model for the flat plat are also shown for comparison. 103

Figure 6.8: Comparison of the dynamic responses in the neighborhood of the fundamental natural frequency, calculated by the reduced order model '+' with the experimentally measured results '*' at various combinations of applied voltages. 104

Figure 6.9: Comparison of the simulated dynamic response of a flat microplate '+' with the experimentally measured response of the microplate '*', which has initial curvature imperfection. 105

LIST OF TABLES

Table 3.1: Summary of convergence studies, number of transverse modes required for convergence and the value of the non-dimensional parameter $\alpha_2 V_{dc}^{\ 2}$ at the pull-in instability..... 55

Table 3.2: A comparison of the time taken by the FE model implemented in COMSOL and the reduced order models to solve the system under an electrostatic DC voltage. 59

Chapter 1

Introduction

1.1. Introduction and Background

Micro-Electro-Mechanical Systems (MEMS) devices are prevalent in many fields from biomedical engineering [1-3] to automotive engineering [4, 5] and aerospace engineering to communications systems [6]. They have received a lot of attention during the last two decades due to their small size, low power consumption, and low cost due to batch fabrication with the existing micro fabrication techniques [7].

MEMS devices are usually actuated by electrostatic, piezoelectric, electrothermal or electromagnetic methods, with the electrostatic is considered most commonly used actuation method [8, 9]. Electrostatic actuation is realized by a parallel plate capacitor; where a flexible structure is suspended over a stationary electrode, which makes the other side of the parallel plate capacitor. The flexible structure is often an elastic microbeam or a microplate, which is made of a conductive material or coated with a conductive material to render conductive properties. It deflects towards stationary electrode under the application of an external voltage load due to the electrostatic force, which is balanced by the elastic resistance of the structure. By increasing the applied voltage, the electrostatic force increases and thus the deflection of the suspended structure also increases. But there is a limit to the applied voltage beyond which the elastic resistive forces of the structure

are unable to balance the external electrostatic load, and the flexible structure becomes unstable and collapses on the stationary electrode. This instability is called pull-in instability and the limiting voltage is called pull-in voltage [10, 11]. In some cases this phenomenon limits the operation of the MEMS devices while in others it is desirable, for example in RF switches.

MEMS devices are commonly made up of electrically actuated flexible microbeams and microplates [8, 12-24]. These are used in various applications, such as micropumps in micro fluidics, biomedical and cooling applications [15-17, 25-27] , microphones [19-21], pressure sensors [28, 29], mass sensors [22, 23] , and resonators [24, 30] to realize sensors and microswitches [31, 32]. These underlying structures often undergo curvature imperfections during the micro fabrication process due to residual stresses.

Accurate modeling and simulation of the mechanical behavior of such structures under the applied nonlinear electrostatic force is required to predict the response prior to the experimental testing and actual use of the device. Accurate models can guide the design engineer through the design process; reducing the design time on one hand and on the other hand can help to improve the existing devices. Nevertheless modeling of MEMS devices is not a trivial task. It poses several challenges, such as inherent nonlinearities and microscale instabilities. Nonlinearities include geometric nonlinearities, the nonlinear electrostatic force, and squeeze film damping [7].

It is common to study the mechanical behavior of MEMS using linear theory [13, 33, 34]; which is applicable only for small deflections. Since in MEMS, structures often undergo large deflection, linear theory becomes inaccurate. Common modeling approaches

include lumped mass models and the Finite Element Method (FEM) [12, 35-37]. Lumped mass models give rough estimate of the response only. FEM based software tools are accurate but computationally expensive, especially when it comes to study the nonlinear dynamic behavior. Differential quadrature method (DQM) have been utilized to solve the governing differential equations [32, 38, 39]. On the other hand Reduced Order Models (ROM) based on the Galerkin approach have gained popularity during the last decades because of their accuracy and low computational cost [11, 40-43]. They have the capability to reveal the effect of different design parameters very conveniently.

1.2. Literature Review

In this section, we summarize the main contributions to the modeling and simulation of mechanical behavior of electrostatically actuated structures, mainly rectangular microplates. Further we also discuss the various modeling and solutions methods.

1.2.1. Flat Plates

Most of the MEMS modeling works can be categorized into two classes. In the first class, the underlying structures are assumed to behave linearly, and hence a linear plate or beam theory are used to model them [13, 27, 33, 34, 44-46]. In the second class, the geometric nonlinearity is accounted for via nonlinear plate theories, such as von-Karman or Mindlin theories [12, 40, 47-49]. Recently, the modified couple stress theory has been used to model the size dependent behavior of microplates [50, 51].

Among the previous works on microplates, Machauf et al. [13] studied the characteristics of an electrostatically actuated micropump. They used the linear plate theory to model the mechanical motion of the pump diaphragm. A ROM was used to predict the performance of the pump. Chao and co-workers [33] used the linear plate theory to model the fully clamped thin plate under electrostatic pressure. They employed a reduced order model to develop an analytical expression for the pull in voltage of the flexible thin plate in the applications of microphones and switches. Nayfeh and Younis [34] used the linear plate theory to model squeeze film damping in microplates. A compressible Reynolds's equation was used to model the squeeze film damping effect. A combination of perturbation and FEM was used to solve for the structural mode shapes, the pressure distribution, the natural frequencies, and the quality factors. Theoretically calculated quality factors were found in good agreement with the experimental data. Bertarelli et al. [27] investigated a circular diaphragm micropump under electric actuation using a linear plate theory and a FE model. They analyzed the behavior of the micropump under quasi static and dynamic electric loading. Ahmad and Pratap [44] investigated the static response of a clamped circular plate under electrostatic load using the Galerkin method. Porfiri [45] investigated the small vibrations of a parallel array of identical microplates deflected under electric loading. Porfiri [45] showed that the vibrational properties can be tuned by properly selecting the DC voltage across the adjacent microplates. Srinivas [46] investigated the static and dynamic pull-in of simply supported microplates using a closed form solution and compared the results with those of a Galerkin approximation.

Ng et al. [12] performed dynamic analysis of microplates under electrostatic forces. They used the BEM to solve the Laplace equation for the electric potential to calculate the

charge density and the corresponding electric force. The first order shear deformation theory (FSDT) was used to model the plate motion and FEM was utilized to discretize the governing equations. Mukherjee et al. [52] and Telukunta et al. [37] used a fully Lagrangian approach to analyze the coupled electro-mechanical field of a MEMS microplate. They employed FEM for the analysis of the mechanical deformations in the plate and the BEM to obtain the electric field exterior to the plate.

Vogl and Nayfeh [47] presented an analytical ROM based on the Galerkin method for fully clamped electrostatically actuated circular plates. The model accounted for the geometric nonlinearity and residual stresses. Faris et al [25] presented a model for a micropump based on electrostatically actuated annular plates. The model predicts the deflection accurately for any voltage up to the pull-in voltage. Mohammadi et al. [39] investigated the pull-in instability of electrostatically actuated circular microplates. They used the strain gradient elasticity theory to account for the size effects. A generalized differential quadrature method (GDQ) was used to solve the governing differential equations. Zhao et al. [40] presented a ROM model based on the Galerkin method for electrostatically actuated rectangular microplates. The model accounts for the nonlinearities due to electric force and midplane stretching through the von-Karman strains. They investigated the static deflection under the applied DC voltage. Natural frequencies and mode shapes were calculated around the deflected position. Zand and Ahmadian [35, 53] investigated the pull-in and vibrational behavior of single and multilayer microplates under electric actuation and squeeze film damping. They used a combination of FEM and finite difference method (FDM) to solve the system of equations.

Fu and Zhang [54] investigated the active control of the nonlinear static and dynamic responses of piezoelectric viscoelastic microplates actuated electrically. They employed the nonlinear von-Karman equations of the plate and used the Galerkin method to discretize the equations. Karimzade et al. [55] studied the nonlinear pull-in instability of a fully clamped microplate with movable base. They solved the governing equation using the extended Kantorovich method and the Galerkin approximation technique.

In recent years, the modified couple stress theory has attracted several researchers for nonlinear analysis of micro structures [50, 51, 56-58]. Gholipour et al. [51] investigated the in-plane and out-of-plane size dependent nonlinear dynamics of microplates resting on elastic foundation. Farokhi and Ghayesh [56] investigated the dynamic behavior of geometrically imperfect microplates.

1.2.2. Initially Curved Plates

Initially deflected microstructures have been investigated extensively in the literature for structures other than microplates, mainly microbeams and micro arches. For instance Vangbo [59] investigated theoretically the snap-through of a doubly clamped beam. Ouakad and Younis [60] studied the dynamic behavior of clamped- clamped micro arches under electric actuation. Krylov et al. [61] presented the theoretical and experimental investigation of the pull-in behavior of an initially curved doubly clamped microbeam actuated by a distributed electrostatic force. Ruzziconi et al. [62] investigated the dynamic behavior of an imperfect clamped–clamped microbeam subjected to electrostatic and electrodynamic actuation.

Numerous works have been reported on the studies of initially imperfect plates at the large scale. Celep [63, 64] made the first attempt to investigate the dynamic behavior of imperfect plates. They conducted a free vibration analysis of such plates with various boundary conditions. They concluded that the static and dynamic behaviors of the plates are very much dependent on the size of the initial imperfection. Yamaki et al. [65, 66] presented theoretical analyses and experimental results for the nonlinear vibrations of a fully clamped rectangular plate with initial deflection and initial edge displacement. The dynamic analog of Marguerre equations [65, 66] was used and the steady state solutions were captured by applying the Galerkin method and the harmonic balance method. Marin et al. [67] investigated the nonlinear response of simply supported initially deformed plates under harmonically varying in-plane edge loading. Lin and Chen [68] investigated the large amplitude vibrations of simply supported, initially imperfect, transversely isotropic, and moderately thick plates. They used the assumed mode shapes as basis function with the Galerkin procedure to discretize the governing equations and the Runge-Kutta method for solving the discretized system of equations. They concluded that the vibration frequencies are very much dependent on the initial imperfection of the plate and the large amplitude behavior may change drastically from hardening to softening depending on the initial imperfection. Ostiguy et al. [69] studied the effect of geometric imperfections on the dynamic response of simply supported plates subjected to periodic in-plane forces. Liu and Yeh [70] studied the nonlinear flexural vibrations of an initially imperfect, orthotropic, and moderately thick plates with various edge conditions. They found that the fundamental natural frequencies are significantly influenced by the initial imperfection. Alijani and Amabili [71] investigated the large amplitude vibration of

completely free imperfect rectangular plates. They used the nonlinear higher-order shear deformation theory for the analysis of the plate response to transverse harmonic excitation near the fundamental mode vibration. Chen et al. [72, 73] derived the governing equation for initially imperfect isotropic plates under arbitrary initial stresses using the modified von-Karman strains. The Galerkin procedure is used for the discretization of the nonlinear governing equations and the Runge-Kutta method is used for solving the discretized system of nonlinear ordinary differential equations to obtain nonlinear and linear vibration frequencies. Huang [74] studied the large amplitude vibrations of imperfect plates using the Lindstedt's perturbation technique and the Runge-Kutta method.

1.2.3. Solutions Methods

The solution methods reported in literature include Finite Element Method (FEM) [12, 35-37], Boundary Element Method (BEM), Differential Quadrature Method (DQM) [32, 38, 39], and Runge Kutta method. FEM based software tools are computationally expensive and may not be suitable for complicated nonlinear dynamic analysis. Reduced order models on the other hand, based on the Galerkin method, are computationally efficient and are capable to perform parametric studies to reveal the effect of different design parameters [11, 40, 47]. Also they can be implemented in sophisticated nonlinear dynamics tools, such as shooting [75, 76].

1.3. Dissertation Objectives

The objectives of the dissertation are:

- To investigate the various approaches to develop a reduced order model based on the Galerkin procedure capable to investigate the static and dynamic behavior of von-Karman rectangular plates under small and large electrostatic forces. Also we will study the accuracy of the reduced order models by comparing the static and natural frequency results with the similar results calculated by finite element models.

- To investigate the nonlinear mechanics of von-Karman microplates under electrostatic actuation. We will study the dynamic response by exciting the microplates near the primary and secondary resonances; super-harmonic and sub-harmonic by generating the frequency response curves. We will also study the dynamic behavior of an imperfect square microplate. Such an imperfection comes practically when fabricating a square plate, which then due to unavoidable fabrication imperfections, will come as a near square plate.

- To develop the reduced order model for initially curved microplates. It is common for the microplate to undergo initial curvature imperfection due to residual stresses caused by the micro fabrication process. Such plates are essentially different from perfectly flat plates and cannot be modeled using flat plates' models.

- To simulate the mechanical behavior of initially curved microplates under electrostatic actuation. We will study the effect of various initial curvature profiles on the static and dynamic behavior of such plates.

- To conduct experiments to measure the static and dynamic responses of an initially curved silicon nitride microplate. We will validate the simulation results by the experimentally measured data.

1.4. Dissertation Contributions

The contributions of the dissertations are:

- Various approaches to develop a reduced order model based on the Galerkin method are presented for von-Karman plates. The accuracy of the reduced order models is studied by comparing the static and natural frequency results with results calculated by finite element models.

- The static and dynamic behaviors of a fully clamped microplate under small and large electrostatic actuation have been investigated and presented.

- The dynamic behavior of an imperfect square plate is presented.

- A dynamic analogue of von-Karman equations for initially curved plates is presented.

- The static and dynamic behavior of initially curved microplates under electrostatic actuation has been investigated and presented. Effects of two commonly encountered initial curvature profiles on mechanical behavior are also presented.

- Reduced order model has been validated by comparing the simulation results with experimentally measured data.

1.5. Dissertation Organization

In Chapter1, general introduction, background, and organization of the dissertation are described. In Chapter 2, we present derivation of the dynamic analogue of the von-Karman equations governing the motion of thin plates using the Hamiltonian principle. The equations account for the midplane stretching and electrostatic forcing nonlinearities.

In Chapter 3, we present various approaches to develop reduced order models for the von-Karman equations to investigate the static and the dynamic behavior when actuated electrostatically. The convergence of the static results with the number of transversal modes retained in the model is presented. We also compare the static results and Eigen value results calculated by these reduced order models with similar results computed by a finite element model implemented in COMSOL Multiphysics, a commercial software. This comparison reveals the accuracy of the models.

In Chapter 4, we present the simulations results for the static and dynamic behavior of a fully clamped microplate when actuated electrostatically. Effect of various non-dimensional design parameters on the static response is presented. Dynamic behavior of the microplate is investigated in the neighborhood of primary resonance by generating frequency response curves. Moreover, cases of dynamic behavior near secondary resonances are also presented. Two case studies of dynamic responses near the super-harmonic resonance of order three and a subharmonic resonance of order one half are presented. We also present the dynamic response of an imperfect square microplate.

In Chapter 5, we present the modeling and simulation of the mechanical behavior of initially curved microplates under electrostatic actuation. We consider two commonly encountered profiles of initial curvature imperfection. To validate the model, we compare the natural frequency and static deflection under electrostatic load calculated by the reduced order model with similar results calculated by a finite element model implemented in COMSOL Multiphysics. An investigation of the effect of the curvature profile on the static and dynamic behavior is also presented.

In Chapter 6, we present the experimentally measured static and dynamic responses of a microplate made of Silicone Nitride. The plate is found to be initially curved by an optical interferometry profiler. Simulation results based on the model presented in Chapter 5 are compared with the experimentally measured static and dynamic response data for model validation purpose. In Chapter 7, a summary of the dissertation is presented along with the main conclusions and recommendations for future work directions.

Chapter 2

Nonlinear von-Karman Analysis of Thin Plates

In this chapter, we derive a dynamic analogue of the nonlinear von-Karman equations and boundary conditions governing the motion of thin isotropic plates, when actuated by an electrostatic force (Figure 2.1). We limit our consideration to flat and initially curved rectangular plates. To derive the equations, we use a combination of Kirchhoff hypothesis and the von-Karman strains. The assumptions of Kirchhoff hypothesis are as follows [77-79]:

(1) The deflection of the midplane is small compared with the thickness of the plate. The slope of the deflected surface is therefore very small and the square of the slope is a negligible quantity in comparison with unity.

(2) The middle plane remains unstrained and neutral during bending.

(3) The straight lines, initially normal to the midplane, remain straight and normal to the middle surface during the deformation and the length of such elements is not altered. This means that the vertical shear strains ε_{13}, ε_{23} and the normal strain ε_{33} are negligible and can be omitted.

(4) The stress normal to the midplane, σ_{33} is small compared with the other stress components and may be neglected in the stress–strain relations.

When the transverse deflection of the midplane is large compared with the thickness of the plate, as in the case of thin von-Karman plates, assumptions (1) and (2) are no longer applicable because the midplane is stretched.

2.1. Thin Flat Plates

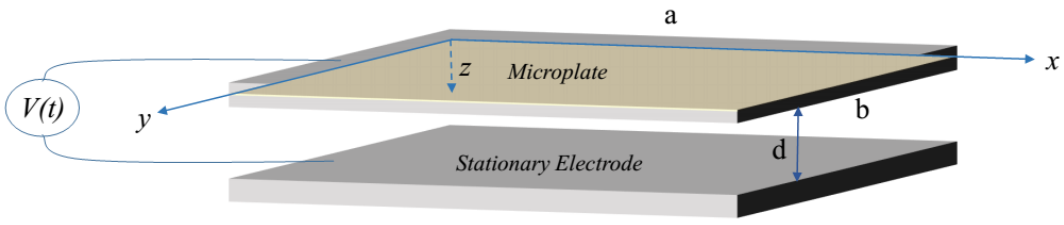

Figure 2.1: A schematic diagram of an electrostatically actuated thin microplate.

In this section, we consider a flat rectangular thin microplate in the domain $0 \le x \le a$ and $0 \le y \le b$, as shown in Figure 2.1. The plate has a constant thickness *h* and a reference, *xyz* Cartesian coordinate system, *xy*-plane being the middle plane of the plate and the *z* axis being normal to that plane and is directed downwards. We denote the displacement components of a point in the middle plane by *u, v* and *w* along *x, y* and *z* direction, respectively. Displacements of an arbitrary point are denoted by $\bar{u}, \bar{v}$ and $\bar{w}$, and are given by

$$\bar{u} = u - z\frac{\partial \bar{w}}{\partial x}\ , \quad \bar{v} = v - z\frac{\partial \bar{w}}{\partial y}, \quad \bar{w} = w \tag{2.1}$$

The von-Karman nonlinear strains are given by

$$\varepsilon_{11} = e_1 - z\frac{\partial^2 w}{\partial x^2}\ ,\quad \varepsilon_{22} = e_2 - z\frac{\partial^2 w}{\partial y^2}\ ,\quad \varepsilon_{12} = \gamma_{12} - 2z\frac{\partial^2 w}{\partial y \partial x}$$

$$\text{and} \qquad \varepsilon_{13} = \varepsilon_{23} = \varepsilon_{33} = 0 \tag{2.2}$$

where e_1, e_2 and γ_{12} are middle plane strain components and are given as

$$e_1 = \frac{\partial u}{\partial x} + \frac{1}{2}\left(\frac{\partial w}{\partial x}\right)^2 ,$$

$$e_2 = \frac{\partial v}{\partial y} + \frac{1}{2}\left(\frac{\partial w}{\partial y}\right)^2 ,$$

$$\gamma_{12} = \frac{\partial u}{\partial y} + \frac{\partial v}{\partial x} + \frac{\partial w}{\partial x}\frac{\partial w}{\partial y}. \tag{2.3}$$

In the absence of body forces, the extended Hamiltonian principle can be written as

$$\int_{t_1}^{t_2} \left(\delta T - \delta U + \delta W_e + \delta W_{nc}\right) dt = 0 \tag{2.4}$$

where δW_{nc} denotes the variation of non-conservative energy W_{nc} , which is problem dependent. Non-conservative damping force can be inserted into the equations of motion after the variational principle has been invoked [80]. Variations of kinetic energy *T*, strain energy *U* and electrostatic potential energy W_e are given as

$$\delta T = -\int_z \int_A \rho \ddot{\mathbf{D}}.\delta \mathbf{D}\, dA dz \tag{2.5}$$

$$\delta U = \int_z \int_A \left(\sigma_{11}\delta\varepsilon_{11} + \sigma_{22}\delta\varepsilon_{22} + \sigma_{33}\delta\varepsilon_{33} + \sigma_{12}\delta\varepsilon_{12} + \sigma_{13}\delta\varepsilon_{13} + \sigma_{23}\delta\varepsilon_{23} \right) dAdz \quad (2.6)$$

$$\delta W_e = \int_A \frac{\varepsilon\, V(t)^2}{2\left(d - \bar{w}\right)^2} \delta w dA \quad (2.7)$$

where ρ is the mass density, **D** denotes the displacement vector of an arbitrary point of differential plate element under observation, A denotes the undeformed area of the reference plane, σ_{ij} and ε_{ij} are the Jaumann stresses and the strains, respectively, d is the parallel plate capacitor gap, ε is the dielectric constant of the plate material and $V(t)$ is the applied voltage.

The displacement vector **D** is given by

$$\mathbf{D} = \bar{u}\mathbf{i} + \bar{v}\mathbf{j} + \bar{w}\mathbf{k} \quad (2.8)$$

where **i, j** and **k** are the unit vectors along the *x,y* and *z* axis, respectively. Substituting equation (2.1) into (2.8) and taking time derivative twice and spatial variation, we obtain

$$\ddot{\mathbf{D}} = \left(\ddot{u} - z\ddot{w}_x\right)\mathbf{i} + \left(\ddot{v} - z\ddot{w}_y\right)\mathbf{j} + \ddot{w}\mathbf{k} \quad (2.9)$$

$$\delta\mathbf{D} = \left(\delta u - z\delta w_x\right)\mathbf{i} + \left(\delta v - z\delta w_y\right)\mathbf{j} + \delta w\mathbf{k}\,. \quad (2.10)$$

Substituting equations (2.9) and (2.10) into equation (2.5) and integrating over the thickness from $z = -h/2$ to $z = h/2$ yields

$$\delta T = -\int_A \left(I_0\ddot{u} - I_1\ddot{w}_x\right)\delta u + \left(I_0\ddot{v} - I_1\ddot{w}_y\right)\delta v + I_0\ddot{w}\delta w + \left(I_2\ddot{w}_x - I_1\ddot{u}\right)\delta w_x + \left(I_2\ddot{w}_y - I_1\ddot{v}\right)\delta w_y dA \quad (2.11)$$

where

$$\{I_0, I_1, I_2\} = \int_z \rho\{1, z, z^2\}\, dz \tag{2.12}$$

and we note that $I_1 = 0$ due to homogeneous assumption. By performing partial integration and dropping the terms involving I_1, equation (2.11) can be written as

$$\begin{aligned}\delta T = &-\int_A I_0 \ddot{u}\delta u + I_0 \ddot{v}\delta v + \left\{I_0 \ddot{w} - I_2 \ddot{w}_{xx} - I_2 \ddot{w}_{yy}\right\}\delta w dA \\ &-\int_y I_2 \ddot{w}_x \Big]_{x=0}^{x=a} \delta w dy - \int_y I_2 \ddot{w}_y \Big]_{y=0}^{y=b} \delta w dx\end{aligned} \tag{2.13}$$

Substituting equations (2.2) and (2.3) into equation (2.6) yields

$$\delta U = \int_z \int_A \begin{bmatrix} \sigma_{11}\left(\delta u_x + w_x \delta w_x - z\delta w_{xx}\right) + \sigma_{22}\left(\delta v_y + w_y \delta w_y - z\delta w_{yy}\right) \\ +\sigma_{12}\left(\delta u_y + \delta v_x + w_x \delta w_y + w_y \delta w_x - 2z\delta w_{xy}\right) \end{bmatrix} dA dz\,. \tag{2.14}$$

Now integrating equation (2.14) over the plate thickness from $z = -h/2$ to $z = h/2$, we get

$$\delta U = \int_A \begin{bmatrix} N_1\left(\delta u_x + w_x \delta w_x\right) + N_{12}\left(\delta u_y + \delta v_x + w_x \delta w_y + w_y \delta w_x\right) \\ +N_2\left(\delta v_y + w_y \delta w_y\right) - M_1 \delta w_{xx} - M_2 \delta w_{yy} - 2M_{12}\delta w_{xy} \end{bmatrix} dA \tag{2.15}$$

where the stress resultants N_i and moments M_i are defined as

$$\{N_1, N_2, N_{12}\} = \int_z \{\sigma_{11}, \sigma_{22}, \sigma_{12}\}\, dz\,,$$

$$\{M_1, M_2, M_{12}\} = \int_z z\{\sigma_{11}, \sigma_{22}, \sigma_{12}\}\, dz\,. \tag{2.16}$$

By performing partial integration, equation (2.15) can be written as

$$\begin{aligned}\delta U = -\int_A \Big[& \left(N_{1x} + N_{12y}\right)\delta u + \left(N_{2y} + N_{12x}\right)\delta v \\ & + \left\{M_{1xx} + M_{2yy} + 2M_{12xy} + \left(N_1 w_x + N_{12} w_y\right)_x + \left(N_2 w_y + N_{12} w_x\right)_y\right\}\delta w \Big] dA \\ & + \int_y \Big[N_1 \delta u + N_{12}\delta v + \left(M_{1x} + 2N_{12y} + N_1 w_x + N_{12} w_y\right)\delta w - M_1 \delta w_x \Big]_{x=0}^{x=a} dy \\ & + \int_x \Big[N_{12}\delta u + N_2 \delta v + \left(M_{2y} + 2N_{12x} + N_2 w_y + N_{12} w_x\right)\delta w - M_2 \delta w_y \Big]_{y=0}^{y=b} dx \\ & - 2M_{12}\delta w\Big]_{(x,y)=(a,0),(0,b)}^{(x,y)=(0,0),(a,b)} dx\end{aligned} \tag{2.17}$$

Substituting equations (2.7), (2.13) and (2.17) into equation (2.4), the three equations of motion obtained from the integrand of the area integral by setting each of the coefficients of δu , δv and δw equal to zero are

$$N_{1x} + N_{12y} = I_0 \ddot{u} \tag{2.18}$$

$$N_{2y} + N_{12x} = I_0 \ddot{v} \tag{2.19}$$

$$M_{1xx} + M_{2yy} + 2M_{12xy} + \left(N_1 w_x + N_{12} w_y\right)_x + \left(N_2 w_y + N_{12} w_x\right)_y + \frac{\varepsilon\, V(t)^2}{2\left(d - \bar{w}\right)^2} = I_0 \ddot{w} - I_2 \ddot{w}_{xx} - I_2 \ddot{w}_{yy} \tag{2.20}$$

Equation (2.18) and (2.19) describe the inplane motion of the plate and, $I_0 \ddot{u}$ and $I_0 \ddot{v}$ are inplane inertia terms. Equation (2.20) describes the out-of-plane motion and three terms on the right hand side, being the inertia terms. First $I_0 \ddot{w}$ is the transverse inertia term, while $I_2 \ddot{w}_{xx}$ and $I_2 \ddot{w}_{yy}$ are rotatory inertia terms. The integrand of the line integral serves to establish the boundary conditions as follows:

Along x=0 and x=a

$$\delta u = 0 \qquad \text{or} \qquad N_1 = 0$$

$$\delta v = 0 \qquad \text{or} \qquad N_{12} = 0$$

$$\delta w = 0 \qquad \text{or} \qquad M_{1x} + 2M_{12y} + N_1 w_x + + N_{12} w_y + + I_2 \ddot{w}_x = 0$$

$$\delta w_x = 0 \qquad \text{or} \qquad M_1 = 0 \ . \tag{2.21}$$

Along y=0 and x=b

$$\delta u = 0 \qquad \text{or} \qquad N_{12} = 0$$

$$\delta v = 0 \qquad \text{or} \qquad N_2 = 0$$

$$\delta w = 0 \qquad \text{or} \qquad M_{2y} + 2M_{12x} + N_{12} w_x + + N_2 w_y + + I_2 \ddot{w}_y = 0$$

$$\delta w_y = 0 \qquad \text{or} \qquad M_2 = 0 \ . \tag{2.22}$$

At (x,y)= (0,0), (a,b), (a,0), (0,b)

$$\delta w = 0 \qquad \text{or} \qquad M_{12} = 0 \ . \tag{2.23}$$

The stress-strain relations for an isotropic material taking the plane stress assumption for the thin plates under consideration are

$$\begin{Bmatrix} \sigma_{11} \\ \sigma_{22} \\ \sigma_{12} \end{Bmatrix} = \frac{E}{1-\upsilon^2} \begin{bmatrix} 1 & \upsilon & 0 \\ \upsilon & 1 & 0 \\ 0 & 0 & (1-\upsilon)/2 \end{bmatrix} \begin{Bmatrix} \varepsilon_{11} \\ \varepsilon_{22} \\ \varepsilon_{12} \end{Bmatrix} \tag{2.24}$$

Substituting equations (2.24), (2.2) and (2.3) into equation (2.16) and performing the integration, we get the expressions for stress resultants N_i and moments M_i as

$$N_1 = \frac{Eh}{1-\upsilon^2}\left[\frac{\partial u}{\partial x} + \frac{1}{2}\left(\frac{\partial w}{\partial x}\right)^2 + \upsilon\left(\frac{\partial v}{\partial y} + \frac{1}{2}\left(\frac{\partial w}{\partial y}\right)^2\right)\right] + N_1^i \tag{2.25}$$

$$N_2 = \frac{Eh}{1-\upsilon^2}\left[\upsilon\left(\frac{\partial u}{\partial x} + \frac{1}{2}\left(\frac{\partial w}{\partial x}\right)^2\right) + \frac{\partial v}{\partial y} + \frac{1}{2}\left(\frac{\partial w}{\partial y}\right)^2\right] + N_2^i \tag{2.26}$$

$$N_{12} = \frac{Eh}{2(1+\upsilon)}\left[\frac{\partial u}{\partial y} + \frac{\partial v}{\partial x} + \frac{\partial w}{\partial x}\frac{\partial w}{\partial y}\right] + N_{12}^i \tag{2.27}$$

$$M_1 = -D\left[\frac{\partial^2 w}{\partial x^2} + \upsilon\frac{\partial^2 w}{\partial y^2}\right] \tag{2.28}$$

$$M_2 = -D\left[\upsilon\frac{\partial^2 w}{\partial x^2} + \frac{\partial^2 w}{\partial y^2}\right] \tag{2.29}$$

$$M_{12} = -D(1-\upsilon)\frac{\partial^2 w}{\partial x \partial y} \tag{2.30}$$

In the relations (2.25) to (2.30) υ and E are the Poisson's ratio and Young's modulus of elasticity, respectively, D is the flexural rigidity of the plate expressed as $\frac{Eh^3}{12(1-\upsilon^2)}$ and the terms with superscript *i* stand for the inplane applied edge loads. By substituting equations (2.25)-(2.30) into the equations of motion (2.18)-(2.20), ignoring the inplane and rotatory inertia terms since they have negligible effect on the transverse motion, and

inserting a non-conservative damping force term f_d into equation (2.20), the governing equations can be written as

$$\frac{\partial^2 u}{\partial x^2}+\frac{1}{2}(1+\upsilon)\frac{\partial^2 v}{\partial x\partial y}+\frac{1}{2}(1-\upsilon)\frac{\partial^2 u}{\partial y^2}+\left(\frac{\partial w}{\partial x}\frac{\partial^2 w}{\partial x^2}\right)+\frac{1}{2}(1+\upsilon)\left(\frac{\partial w}{\partial y}\frac{\partial^2 w}{\partial x\partial y}\right)+\frac{1}{2}(1-\upsilon)\left(\frac{\partial w}{\partial x}\frac{\partial^2 w}{\partial y^2}\right)=0 \tag{2.31}$$

$$\frac{\partial^2 v}{\partial y^2}+\frac{1}{2}(1+\upsilon)\frac{\partial^2 u}{\partial x\partial y}+\frac{1}{2}(1-\upsilon)\frac{\partial^2 v}{\partial x^2}+\left(\frac{\partial w}{\partial y}\frac{\partial^2 w}{\partial y^2}\right)+\frac{1}{2}(1+\upsilon)\left(\frac{\partial w}{\partial x}\frac{\partial^2 w}{\partial x\partial y}\right)+\frac{1}{2}(1-\upsilon)\left(\frac{\partial w}{\partial y}\frac{\partial^2 w}{\partial x^2}\right)=0 \tag{2.32}$$

$$\begin{aligned}&\frac{h^2}{12}\nabla^4 w+\frac{\rho(1-\upsilon^2)}{Eh}\frac{\partial^2 w}{\partial t^2}+\frac{(1-\upsilon^2)}{E\,h}f_d=\frac{(1-\upsilon^2)}{E\,h}\frac{\varepsilon\,V(t)^2}{2\,(d-\bar{w})^2}+\frac{(1-\upsilon^2)}{Eh}\left(N_1^i\frac{\partial^2 w}{\partial x^2}+2N_{12}^i\frac{\partial^2 w}{\partial x\partial y}+N_2^i\frac{\partial^2 w}{\partial y^2}\right)\\&+\frac{\partial u}{\partial x}\left(\frac{\partial^2 w}{\partial x^2}+\upsilon\frac{\partial^2 w}{\partial y^2}\right)+\frac{\partial v}{\partial y}\left(\upsilon\frac{\partial^2 w}{\partial x^2}+\frac{\partial^2 w}{\partial y^2}\right)+\frac{1}{2}\left(\frac{\partial w}{\partial x}\right)^2\left(\frac{\partial^2 w}{\partial x^2}+\upsilon\frac{\partial^2 w}{\partial y^2}\right)+\frac{1}{2}\left(\frac{\partial w}{\partial y}\right)^2\left(\upsilon\frac{\partial^2 w}{\partial x^2}+\frac{\partial^2 w}{\partial y^2}\right)\\&+(1-\upsilon)\frac{\partial^2 w}{\partial x\partial y}\left(\frac{\partial u}{\partial y}+\frac{\partial v}{\partial x}+\frac{\partial w}{\partial x}\frac{\partial w}{\partial y}\right)\end{aligned} \tag{2.33}$$

where ∇^4 is the bi-harmonic operator expressed as $\nabla^4=\frac{\partial^4}{\partial x^4}+2\frac{\partial^4}{\partial x^2\partial y^2}+\frac{\partial^4}{\partial y^4}$. The applied voltage $V(t)$ is either a DC voltage V_{dc} for static analysis or an AC voltage V_{ac} superimposed to V_{dc}, i.e. $V(t)=V_{dc}+V_{ac}Sin(\Omega t)$, where Ω is the actuating frequency. The non-conservative damping force f_d is expressed as $c\frac{\partial w}{\partial t}$, where c is the viscous damping coefficient.

2.2. Initially Curved Imperfect Plates

In this section, we consider an initially curved rectangular plate having an initial curvature imperfection $w_0(x,y)$ and in the domain $0\le x\le a$ and $0\le y\le b$, as shown in Figure 2.2.

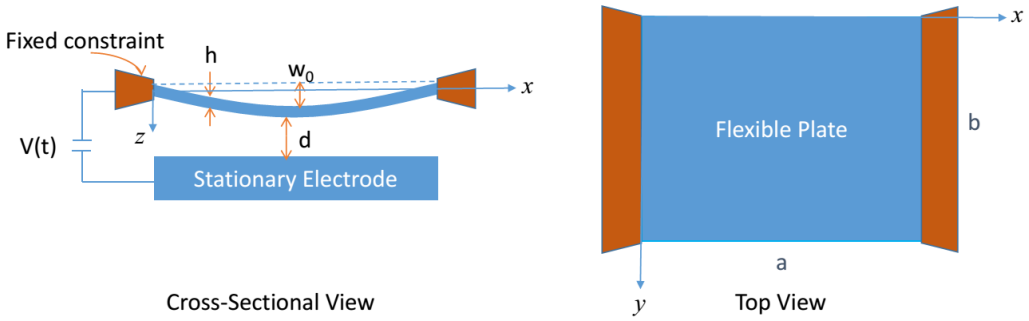

Figure 2.2: A schematic diagram of an electrically actuated initially curved clamped-free-clamped-free microplate.

We use the modified von-Karman strains for an initially curved plate along with the Kirchhoff hypothesis to derive the governing equations of motion. We denote the displacement components of a point in the middle plane by *u*, *v* and *w* along *x*, *y* and *z* direction, respectively. Displacements of an arbitrary point are denoted by $\bar{u}, \bar{v}$ and $\bar{w}$, and are given by

$$\bar{u} = u - z\frac{\partial \bar{w}}{\partial x}\ , \quad \bar{v} = v - z\frac{\partial \bar{w}}{\partial y}, \quad \bar{w} = w \tag{2.34}$$

The modified von-Karman nonlinear strains for an initially curved plate are given by

$$\varepsilon_{11} = e_1 - z\frac{\partial^2 w}{\partial x^2}\ , \quad \varepsilon_{22} = e_2 - z\frac{\partial^2 w}{\partial y^2}, \quad \varepsilon_{12} = \gamma_{12} - 2z\frac{\partial^2 w}{\partial y \partial x}$$

and $$\varepsilon_{13} = \varepsilon_{23} = \varepsilon_{33} = 0 \tag{2.35}$$

where e_1, e_2 and γ_{12} are the middle plane strain components and are expressed as

$$e_1 = \frac{\partial u}{\partial x} + \frac{1}{2}\left(\frac{\partial w}{\partial x}\right)^2 + \frac{\partial w}{\partial x}\frac{\partial w_0}{\partial x} \ ,$$

$$e_2 = \frac{\partial v}{\partial y} + \frac{1}{2}\left(\frac{\partial w}{\partial y}\right)^2 + \frac{\partial w}{\partial y}\frac{\partial w_0}{\partial y} \ ,$$

$$\gamma_{12} = \frac{\partial u}{\partial y} + \frac{\partial v}{\partial x} + \frac{\partial w}{\partial x}\frac{\partial w}{\partial y} + \frac{\partial w_0}{\partial x}\frac{\partial w}{\partial y} + \frac{\partial w}{\partial x}\frac{\partial w_0}{\partial y} \ . \tag{2.36}$$

In this case variation of the strain energy, by substituting equations (2.35) and (2.36) into equation (2.6), is given as

$$\delta U = \int_z \iint_A \left[\begin{array}{l} \sigma_{11}\left(\delta u_x + w_x \delta w_x + w_{0x}\delta w_x - z\delta w_{xx}\right) + \sigma_{22}\left(\delta v_y + w_y \delta w_y + w_{0y}\delta w_y - z\delta w_{yy}\right) \\ +\sigma_{12}\left(\delta u_y + \delta v_x + w_x \delta w_y + w_y \delta w_x + w_{0x}\delta w_y + w_{0y}\delta w_x - 2z\delta w_{xy}\right) \end{array} \right] dA dz \ . \tag{2.37}$$

Now integrating equation (2.37) over the plate thickness from $z = -h/2$ to $z = h/2$, we get

$$\delta U = \int_A \left[\begin{array}{l} N_1\left(\delta u_x + w_x \delta w_x + w_{0x}\delta w_x\right) + N_{12}\left(\delta u_y + \delta v_x + w_x \delta w_y + w_y \delta w_x + w_{0x}\delta w_y + w_{0y}\delta w_x\right) \\ +N_2\left(\delta v_y + w_y \delta w_y + w_{0y}\delta w_y\right) - M_1 \delta w_{xx} - M_2 \delta w_{yy} - 2M_{12}\delta w_{xy} \end{array} \right] dA \tag{2.38}$$

where the stress resultants N_i and moments M_i are defined as in (2.16). By performing partial integration, equation (2.38) can be written as

$$\delta U = -\int_A \Big[\left(N_{1x} + N_{12y} \right) \delta u + \left(N_{2y} + N_{12x} \right) \delta v + \left\{ \begin{matrix} M_{1xx} + M_{2yy} + 2M_{12xy} + \left(N_1 w_x + N_{12} w_y \right)_x + \left(N_2 w_y + N_{12} w_x \right)_y \\ + \left(N_1 w_{0x} + N_{12} w_{0y} \right)_x + \left(N_2 w_{0y} + N_{12} w_{0x} \right)_y \end{matrix} \right\} \delta w \Big] dA$$
$$+ \int_y \Big[N_1 \delta u + N_{12} \delta v + \left(M_{1x} + 2N_{12y} + N_1 w_x + N_{12} w_y + N_1 w_{0x} + N_{12} w_{0y} \right) \delta w - M_1 \delta w_x \Big]_{x=0}^{x=a} dy$$
$$+ \int_x \Big[N_{12} \delta u + N_2 \delta v + \left(M_{2y} + 2N_{12x} + N_2 w_y + N_{12} w_x + N_2 w_{0y} + N_{12} w_{0x} \right) \delta w - M_2 \delta w_y \Big]_{y=0}^{y=b} dx$$
$$-2M_{12} \delta w \Big]_{(x,y)=(a,0),(0,b)}^{(x,y)=(0,0),(a,b)} dx \tag{2.39}$$

Substituting equations (2.7), (2.13) and (2.40) into equation (2.4), the three equations of motion obtained from the integrand of the area integral by setting each of the coefficients of δu, δv and δw equal to zero are

$$N_{1x} + N_{12y} = I_0 \ddot{u} \tag{2.40}$$

$$N_{2y} + N_{12x} = I_0 \ddot{v} \tag{2.41}$$

$$M_{1xx} + M_{2yy} + 2M_{12xy} + \left(N_1 w_x + N_{12} w_y \right)_x + \left(N_2 w_y + N_{12} w_x \right)_y +$$
$$\left(N_1 w_{0x} + N_{12} w_{0y} \right)_x + \left(N_2 w_{0y} + N_{12} w_{0x} \right)_y + \frac{\varepsilon \, V(t)^2}{2 \left(d - \bar{w} \right)^2} = I_0 \ddot{w} - I_2 \ddot{w}_{xx} - I_2 \ddot{w}_{yy} \tag{2.42}$$

Equations (2.40) and (2.41) describe the inplane motion and equation (2.42) describes the out-of-plane motion. The integrand of the line integral serves to establish the boundary conditions.

Substituting equation (2.24), (2.35) and (2.36) into equation (2.16) and performing the integration, we get the expressions for stress resultants N_i and moments M_i as

$$N_1 = \frac{Eh}{1-\upsilon^2}\left[\frac{\partial u}{\partial x} + \frac{1}{2}\left(\frac{\partial w}{\partial x}\right)^2 + \frac{\partial w}{\partial x}\frac{\partial w_0}{\partial x} + \upsilon\left(\frac{\partial v}{\partial y} + \frac{1}{2}\left(\frac{\partial w}{\partial y}\right)^2 + \frac{\partial w}{\partial y}\frac{\partial w_0}{\partial y}\right)\right] + N_1^i \tag{2.43}$$

$$N_2 = \frac{Eh}{1-\upsilon^2}\left[\upsilon\left(\frac{\partial u}{\partial x} + \frac{1}{2}\left(\frac{\partial w}{\partial x}\right)^2 + \frac{\partial w}{\partial x}\frac{\partial w_0}{\partial x}\right) + \frac{\partial v}{\partial y} + \frac{1}{2}\left(\frac{\partial w}{\partial y}\right)^2 + \frac{\partial w}{\partial y}\frac{\partial w_0}{\partial y}\right] + N_2^i \tag{2.44}$$

$$N_{12} = \frac{Eh}{2(1+\upsilon)}\left[\frac{\partial u}{\partial y} + \frac{\partial v}{\partial x} + \frac{\partial w}{\partial x}\frac{\partial w}{\partial y} + \frac{\partial w_0}{\partial x}\frac{\partial w}{\partial y} + \frac{\partial w}{\partial x}\frac{\partial w_0}{\partial y}\right] + N_{12}^i \tag{2.45}$$

$$M_1 = -D\left[\frac{\partial^2 w}{\partial x^2} + \upsilon\frac{\partial^2 w}{\partial y^2}\right] \tag{2.46}$$

$$M_2 = -D\left[\upsilon\frac{\partial^2 w}{\partial x^2} + \frac{\partial^2 w}{\partial y^2}\right] \tag{2.47}$$

$$M_{12} = -D(1-\upsilon)\frac{\partial^2 w}{\partial x \partial y} \tag{2.48}$$

By substituting equations (2.43)-(2.48) into the equations of motion (2.40)-(2.42), ignoring the inplane and rotatory inertia terms since they have negligible effect on transverse motion, and inserting a non-conservative damping force term f_d into equation (2.48), the governing equations can be written as follows:

$$\begin{aligned}&\frac{\partial^2 u}{\partial x^2} + \frac{1}{2}(1+\upsilon)\frac{\partial^2 v}{\partial x \partial y} + \frac{1}{2}(1-\upsilon)\frac{\partial^2 u}{\partial y^2} + \left(\frac{\partial w}{\partial x}\frac{\partial^2 w}{\partial x^2} + \frac{\partial w_0}{\partial x}\frac{\partial^2 w}{\partial x^2} + \frac{\partial w}{\partial x}\frac{\partial^2 w_0}{\partial x^2}\right)\\ &+\frac{1}{2}(1+\upsilon)\left(\frac{\partial w}{\partial y}\frac{\partial^2 w}{\partial x \partial y} + \frac{\partial w_0}{\partial y}\frac{\partial^2 w}{\partial x \partial y} + \frac{\partial w}{\partial y}\frac{\partial^2 w_0}{\partial x \partial y}\right) + \frac{1}{2}(1-\upsilon)\left(\frac{\partial w}{\partial x}\frac{\partial^2 w}{\partial y^2} + \frac{\partial w_0}{\partial x}\frac{\partial^2 w}{\partial y^2} + \frac{\partial w}{\partial x}\frac{\partial^2 w_0}{\partial y^2}\right) = 0\end{aligned} \tag{2.49}$$

$$\frac{\partial^2 v}{\partial y^2}+\frac{1}{2}(1+\upsilon)\frac{\partial^2 u}{\partial x\partial y}+\frac{1}{2}(1-\upsilon)\frac{\partial^2 v}{\partial x^2}+\left(\frac{\partial w}{\partial y}\frac{\partial^2 w}{\partial y^2}+\frac{\partial w_0}{\partial y}\frac{\partial^2 w}{\partial y^2}+\frac{\partial w}{\partial y}\frac{\partial^2 w_0}{\partial y^2}\right)$$
$$+\frac{1}{2}(1+\upsilon)\left(\frac{\partial w}{\partial x}\frac{\partial^2 w}{\partial x\partial y}+\frac{\partial w_0}{\partial x}\frac{\partial^2 w}{\partial x\partial y}+\frac{\partial w}{\partial x}\frac{\partial^2 w_0}{\partial x\partial y}\right)+\frac{1}{2}(1-\upsilon)\left(\frac{\partial w}{\partial y}\frac{\partial^2 w}{\partial x^2}+\frac{\partial w_0}{\partial y}\frac{\partial^2 w}{\partial x^2}+\frac{\partial w}{\partial y}\frac{\partial^2 w_0}{\partial x^2}\right)=0 \tag{2.50}$$

$$\frac{h^2}{12}\nabla^4 w+\frac{\rho(1-\upsilon^2)}{Eh}\frac{\partial^2 w}{\partial t^2}+\frac{(1-\upsilon^2)}{E\,h}f_d=\frac{(1-\upsilon^2)}{E\,h}\frac{\varepsilon\,V(t)^2}{2\,(d-\bar{w})^2}+\frac{(1-\upsilon^2)}{Eh}\left(N_1^i\frac{\partial^2 w}{\partial x^2}+2N_{12}^i\frac{\partial^2 w}{\partial x\partial y}+N_2^i\frac{\partial^2 w}{\partial y^2}\right)$$
$$+\frac{\partial u}{\partial x}\left(\frac{\partial^2 w}{\partial x^2}+\upsilon\frac{\partial^2 w}{\partial y^2}\right)+\frac{\partial v}{\partial y}\left(\upsilon\frac{\partial^2 w}{\partial x^2}+\frac{\partial^2 w}{\partial y^2}\right)+(1-\upsilon)\left(\frac{\partial u}{\partial y}+\frac{\partial v}{\partial x}\right)\frac{\partial^2 w}{\partial x\partial y}$$
$$+\frac{1}{2}\left(\frac{\partial w}{\partial x}\right)^2\left(\frac{\partial^2 w}{\partial x^2}+\upsilon\frac{\partial^2 w}{\partial y^2}\right)+\left(\frac{\partial w}{\partial x}\frac{\partial w_0}{\partial x}\right)\left(\frac{\partial^2 w}{\partial x^2}+\upsilon\frac{\partial^2 w}{\partial y^2}\right)+\frac{1}{2}\left(\frac{\partial w}{\partial y}\right)^2\left(\upsilon\frac{\partial^2 w}{\partial x^2}+\frac{\partial^2 w}{\partial y^2}\right)$$
$$+\left(\frac{\partial w}{\partial y}\frac{\partial w_0}{\partial y}\right)\left(\upsilon\frac{\partial^2 w}{\partial x^2}+\frac{\partial^2 w}{\partial y^2}\right)+(1-\upsilon)\left(\frac{\partial w}{\partial x}\frac{\partial w}{\partial y}\frac{\partial^2 w}{\partial x\partial y}+\frac{\partial w_0}{\partial x}\frac{\partial w}{\partial y}\frac{\partial^2 w}{\partial x\partial y}+\frac{\partial w}{\partial x}\frac{\partial w_0}{\partial y}\frac{\partial^2 w}{\partial x\partial y}\right)$$
$$+\frac{\partial u}{\partial x}\left(\frac{\partial^2 w_0}{\partial x^2}+\upsilon\frac{\partial^2 w_0}{\partial y^2}\right)+\frac{\partial v}{\partial y}\left(\upsilon\frac{\partial^2 w_0}{\partial x^2}+\frac{\partial^2 w_0}{\partial y^2}\right)+(1-\upsilon)\left(\frac{\partial u}{\partial y}+\frac{\partial v}{\partial x}\right)\frac{\partial^2 w_0}{\partial x\partial y}$$
$$+\frac{1}{2}\left(\frac{\partial w}{\partial x}\right)^2\left(\frac{\partial^2 w_0}{\partial x^2}+\upsilon\frac{\partial^2 w_0}{\partial y^2}\right)+\left(\frac{\partial w}{\partial x}\frac{\partial w_0}{\partial x}\right)\left(\frac{\partial^2 w_0}{\partial x^2}+\upsilon\frac{\partial^2 w_0}{\partial y^2}\right)+\frac{1}{2}\left(\frac{\partial w}{\partial y}\right)^2\left(\upsilon\frac{\partial^2 w_0}{\partial x^2}+\frac{\partial^2 w_0}{\partial y^2}\right)$$
$$+\left(\frac{\partial w}{\partial y}\frac{\partial w_0}{\partial y}\right)\left(\upsilon\frac{\partial^2 w_0}{\partial x^2}+\frac{\partial^2 w_0}{\partial y^2}\right)+(1-\upsilon)\left(\frac{\partial w}{\partial x}\frac{\partial w}{\partial y}\frac{\partial^2 w_0}{\partial x\partial y}+\frac{\partial w_0}{\partial x}\frac{\partial w}{\partial y}\frac{\partial^2 w_0}{\partial x\partial y}+\frac{\partial w}{\partial x}\frac{\partial w_0}{\partial y}\frac{\partial^2 w_0}{\partial x\partial y}\right) \tag{2.51}$$

The associated boundary conditions for the case of a clamped-free-clamped-free plate (Figure 2.2) are

Clamped edges at $x=0$ *and* $x=a$

$$u=0 \tag{2.52}$$

$$v=0 \tag{2.53}$$

$$w=0 \tag{2.54}$$

$$\frac{\partial w}{\partial x}=0 \tag{2.55}$$

Free edges at $y=0$ *and* $y=b$

$$\frac{\partial v}{\partial y}+\upsilon\frac{\partial u}{\partial x}+\frac{1}{2}\left[\left(\frac{\partial w}{\partial y}\right)^2+\upsilon\left(\frac{\partial w}{\partial x}\right)^2\right]=0 \tag{2.56}$$

$$\frac{\partial u}{\partial y}+\frac{\partial v}{\partial x}+\frac{\partial w}{\partial x}\frac{\partial w}{\partial y}=0 \tag{2.57}$$

$$\frac{\partial^2 w}{\partial y^2}+\upsilon\frac{\partial^2 w}{\partial x^2}=0 \tag{2.58}$$

$$\frac{\partial^3 w}{\partial y^3}+\left(2-\upsilon\right)\frac{\partial^3 w}{\partial y\partial x^2}=0 \tag{2.59}$$

Chapter 3

Approaches for Reduced Order Modeling of Electrically Actuated von-Karman Microplates

In this chapter, we present and compare various approaches to develop reduced order models for the nonlinear von-Karman rectangular microplates actuated by nonlinear electrostatic forces. The reduced-order models aim to investigate the static and dynamic behavior of the plate under small and large actuation forces. A fully clamped microplate is considered. Different types of basis functions are used in conjunction with the Galerkin method to discretize the governing equations. First we investigate the convergence with the number of modes retained in the model. Then for validation purpose, a comparison of the static results is made with the results calculated by a nonlinear finite element model. The linear eigenvalue problem for the plate under the electrostatic force is solved for a wide range of voltages up to pull-in. Results among the various reduced-order modes are compared and are also validated by comparing to results of the finite-element model. Further, the reduced order models are employed to capture the forced dynamic response of the microplate under small and large vibration amplitudes. Comparison of the different approaches also is made for this case.

3.1. Introduction

We consider a fully clamped planar microplate as shown in Figure 3.1. The model accounts for the geometric nonlinearity as well as the nonlinearity due to the electrostatic force. Different types of basis functions are used in conjunction with the Galerkin method to discretize the governing equations.

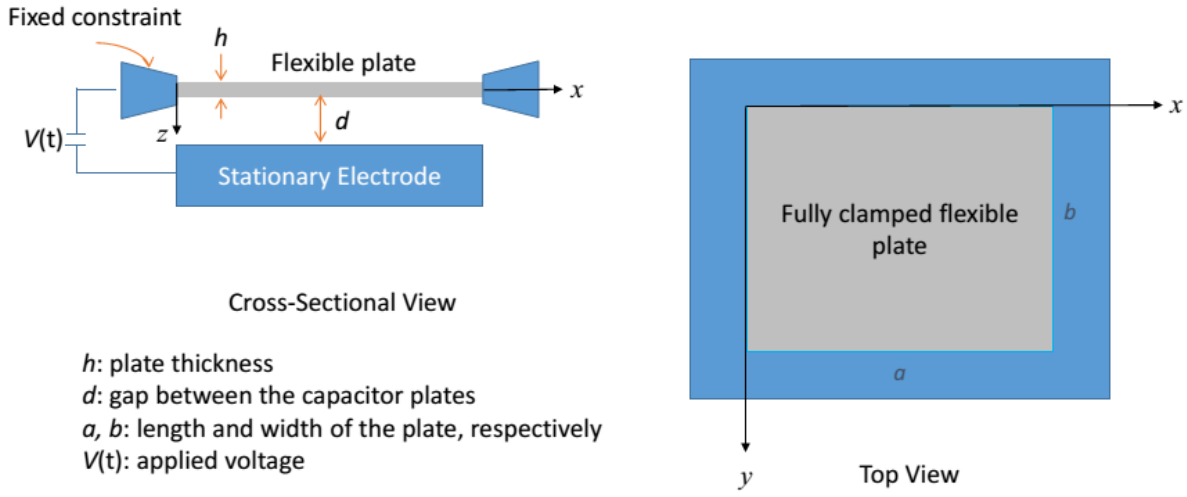

Figure 3.1: A schematic diagram of an electrically actuated fully clamped microplate.

3.2. Problem Formulation

We adopt the dynamic version of the von-Karman equations (2.31)-(2.33) to describe the plate motion. Associated boundary conditions for a fully clamped plate (Figure 3.1) are

Clamped edges at $x=0$ *and* $x=a$

$$u = 0 \tag{3.1}$$

$$v = 0 \tag{3.2}$$

$$w = 0 \tag{3.3}$$

$$\frac{\partial w}{\partial x} = 0 \tag{3.4}$$

Clamped edges at $y=0$ *and* $y=b$

$$u = 0 \tag{3.5}$$

$$v = 0 \tag{3.6}$$

$$w = 0 \tag{3.7}$$

$$\frac{\partial w}{\partial y} = 0 \tag{3.8}$$

For convenience, we introduce the non-dimensional variables (denoted by hats);

$$\hat{x} = \frac{x}{a} \ , \ \ \hat{y} = \frac{y}{b} \ , \ \ \hat{w} = \frac{w}{d} \ , \ \ \hat{u} = \frac{au}{d^2} \ , \ \ \hat{v} = \frac{av}{d^2} \ , \ \ \hat{t} = \frac{t}{T} \tag{3.9}$$

Substituting equation (3.9) into equations (2.31)-(2.33) and dropping the hats we get the following equations:

$$\frac{\partial^2 u}{\partial x^2} + \frac{(1+\upsilon)}{2\alpha}\frac{\partial^2 v}{\partial x \partial y} + \frac{(1-\upsilon)}{2\alpha^2}\frac{\partial^2 u}{\partial y^2} + \frac{\partial w}{\partial x}\frac{\partial^2 w}{\partial x^2} + \frac{(1+\upsilon)}{2\alpha^2}\frac{\partial w}{\partial y}\frac{\partial^2 w}{\partial x \partial y} + \frac{(1-\upsilon)}{2\alpha^2}\frac{\partial w}{\partial x}\frac{\partial^2 w}{\partial y^2} = 0 \tag{3.10}$$

$$\frac{\partial^2 v}{\partial y^2}+\frac{(1+\upsilon)\alpha}{2}\frac{\partial^2 u}{\partial x\partial y}+\frac{(1-\upsilon)\alpha^2}{2}\frac{\partial^2 v}{\partial x^2}+\frac{1}{\alpha}\frac{\partial w}{\partial y}\frac{\partial^2 w}{\partial y^2}+\frac{(1+\upsilon)\alpha}{2}\frac{\partial w}{\partial x}\frac{\partial^2 w}{\partial x\partial y}+\frac{(1-\upsilon)}{2}\frac{\partial w}{\partial y}\frac{\partial^2 w}{\partial x^2}=0 \tag{3.11}$$

$$\begin{aligned}&\frac{\partial^4 w}{\partial x^4}+\frac{2}{\alpha^2}\frac{\partial^4 w}{\partial x^2\partial y^2}+\frac{1}{\alpha^4}\frac{\partial^4 w}{\partial y^4}+\frac{\partial^2 w}{\partial t^2}+\hat{c}\frac{\partial w}{\partial t}=\alpha_2\frac{V(t)^2}{(1-w)^2}+3\alpha_0^2\left\{\hat{N}_1\frac{\partial^2 w}{\partial x^2}+\frac{2}{\alpha}\hat{N}_{12}\frac{\partial^2 w}{\partial x\partial y}+\frac{1}{\alpha^2}\hat{N}_2\frac{\partial^2 w}{\partial y^2}\right\}\\&+12\alpha_1^2\left\{\frac{\partial u}{\partial x}\left(\frac{\partial^2 w}{\partial x^2}+\frac{\upsilon}{\alpha^2}\frac{\partial^2 w}{\partial y^2}\right)+\frac{1}{\alpha}\frac{\partial v}{\partial y}\left(\upsilon\frac{\partial^2 w}{\partial x^2}+\frac{1}{\alpha^2}\frac{\partial^2 w}{\partial y^2}\right)+(1-\upsilon)\left(\frac{1}{\alpha}\frac{\partial u}{\partial y}+\frac{\partial v}{\partial x}\right)\frac{1}{\alpha}\frac{\partial^2 w}{\partial x\partial y}\right\}\\&+12\alpha_1^2\left\{\frac{1}{2}\left(\frac{\partial w}{\partial x}\right)^2\left(\frac{\partial^2 w}{\partial x^2}+\frac{\upsilon}{\alpha^2}\frac{\partial^2 w}{\partial y^2}\right)+\frac{1}{2\alpha^2}\left(\frac{\partial w}{\partial y}\right)^2\left(\upsilon\frac{\partial^2 w}{\partial x^2}+\frac{1}{\alpha^2}\frac{\partial^2 w}{\partial y^2}\right)+\frac{(1-\upsilon)}{\alpha^2}\left(\frac{\partial w}{\partial x}\frac{\partial w}{\partial y}\frac{\partial^2 w}{\partial x\partial y}\right)\right\}\end{aligned} \tag{3.12}$$

The parameters appearing in equations (3.10)-(3.12) are

$$\alpha=\frac{b}{a}\ ,\quad \alpha_0=\frac{a}{h}\ ,\quad \alpha_1=\frac{d}{h}\ ,\quad \alpha_2=\frac{6\left(1-\upsilon^2\right)}{E\,h^3 d^3}\varepsilon\,a^4\ ,\quad \hat{c}=\frac{ca^4}{TD}\ \text{ and }\ \hat{N}_j=\frac{\left(1-\upsilon^2\right)}{Eh}N_J^i \tag{3.13}$$

where T is the characteristic time expressed as $T=\sqrt{\frac{\rho a^4}{D}}$

The boundary conditions for the non-dimensional equations are:

Clamped edges at x=0 and x=1

$$u=0 \tag{3.14}$$

$$v=0 \tag{3.15}$$

$$w=0 \tag{3.16}$$

$$\frac{\partial w}{\partial x}=0 \tag{3.17}$$

Clamped edges at y=0 and y=1

$$u = 0 \tag{3.18}$$

$$v = 0 \tag{3.19}$$

$$w = 0 \tag{3.20}$$

$$\frac{\partial w}{\partial y} = 0 \tag{3.21}$$

For the purpose of solving for the eigenvalues of the plate, we linearize the non-dimensional governing equations (3.10)-(3.12) around the deflected position due to the DC electrostatic load. Towards this, we express the microplate response as the sum of the static components w_s, u_s and v_s and the dynamic components w_d, u_d and v_d

$$w = w_s + w_d \tag{3.22}$$

$$u = u_s + u_d \tag{3.23}$$

$$v = v_s + v_d \tag{3.24}$$

Now, by plugging equations (3.22)-(3.24) into equations (3.10)-(3.12), cancelling the equilibrium terms and retaining only linear terms in u_d, v_d and w_d, we obtain

$$\begin{aligned}&\frac{\partial^2 u_d}{\partial x^2} + \frac{(1+\upsilon)}{2\alpha}\frac{\partial^2 v_d}{\partial x \partial y} + \frac{(1-\upsilon)}{2\alpha^2}\frac{\partial^2 u_d}{\partial y^2} + \frac{\partial w_s}{\partial x}\frac{\partial^2 w_d}{\partial x^2} + \frac{\partial w_d}{\partial x}\frac{\partial^2 w_s}{\partial x^2} + \frac{(1+\upsilon)}{2\alpha^2}\left(\frac{\partial w_s}{\partial y}\frac{\partial^2 w_d}{\partial x \partial y} + \frac{\partial w_d}{\partial y}\frac{\partial^2 w_s}{\partial x \partial y}\right) \\ &+ \frac{(1-\upsilon)}{2\alpha^2}\left(\frac{\partial w_s}{\partial x}\frac{\partial^2 w_d}{\partial y^2} + \frac{\partial w_d}{\partial x}\frac{\partial^2 w_s}{\partial y^2}\right) = 0\end{aligned} \tag{3.25}$$

$$\frac{\partial^2 v_d}{\partial y^2}+\frac{(1+\upsilon)\alpha}{2}\frac{\partial^2 u_d}{\partial x\partial y}+\frac{(1-\upsilon)\alpha^2}{2}\frac{\partial^2 v_d}{\partial x^2}+\frac{1}{\alpha}\left(\frac{\partial w_s}{\partial y}\frac{\partial^2 w_d}{\partial y^2}+\frac{\partial w_d}{\partial y}\frac{\partial^2 w_s}{\partial y^2}\right)+\frac{(1+\upsilon)\alpha}{2}\left(\frac{\partial w_s}{\partial x}\frac{\partial^2 w_d}{\partial x\partial y}+\frac{\partial w_d}{\partial x}\frac{\partial^2 w_s}{\partial x\partial y}\right)$$
$$+\frac{(1-\upsilon)}{2}\left(\frac{\partial w_s}{\partial y}\frac{\partial^2 w_d}{\partial x^2}+\frac{\partial w_d}{\partial y}\frac{\partial^2 w_s}{\partial x^2}\right)=0 \tag{3.26}$$

$$\frac{\partial^4 w_d}{\partial x^4}+\frac{2}{\alpha^2}\frac{\partial^4 w_d}{\partial x^2\partial y^2}+\frac{1}{\alpha^4}\frac{\partial^4 w_d}{\partial y^4}+\frac{\partial w_d}{\partial t^2}=2\alpha_2\frac{V(t)^2 w_d}{(1-w_s)^3}+3\alpha_0^2\left\{\hat{N}_1\frac{\partial^2 w_d}{\partial x^2}+\frac{2}{\alpha}\hat{N}_{12}\frac{\partial^2 w_d}{\partial x\partial y}+\frac{1}{\alpha^2}\hat{N}_2\frac{\partial^2 w_d}{\partial y^2}\right\}$$
$$+12\alpha_1^2\left\{\begin{array}{l}\frac{\partial u_s}{\partial x}\left(\frac{\partial^2 w_d}{\partial x^2}+\frac{\upsilon}{\alpha^2}\frac{\partial^2 w_d}{\partial y^2}\right)+\frac{\partial u_d}{\partial x}\left(\frac{\partial^2 w_s}{\partial x^2}+\frac{\upsilon}{\alpha^2}\frac{\partial^2 w_s}{\partial y^2}\right)\\ +\frac{1}{\alpha}\frac{\partial v_s}{\partial y}\left(\upsilon\frac{\partial^2 w_d}{\partial x^2}+\frac{1}{\alpha^2}\frac{\partial^2 w_d}{\partial y^2}\right)+\frac{1}{\alpha}\frac{\partial v_d}{\partial y}\left(\upsilon\frac{\partial^2 w_s}{\partial x^2}+\frac{1}{\alpha^2}\frac{\partial^2 w_s}{\partial y^2}\right)\\ +(1-\upsilon)\left(\frac{1}{\alpha}\frac{\partial u_s}{\partial y}+\frac{\partial v_s}{\partial x}\right)\frac{1}{\alpha}\frac{\partial^2 w_d}{\partial x\partial y}+(1-\upsilon)\left(\frac{1}{\alpha}\frac{\partial u_d}{\partial y}+\frac{\partial v_d}{\partial x}\right)\frac{1}{\alpha}\frac{\partial^2 w_s}{\partial x\partial y}\end{array}\right\}$$
$$+12\alpha_1^2\left\{\begin{array}{l}\frac{1}{2}\left(\frac{\partial w_s}{\partial x}\right)^2\left(\frac{\partial^2 w_d}{\partial x^2}+\frac{\upsilon}{\alpha^2}\frac{\partial^2 w_d}{\partial y^2}\right)+\left(\frac{\partial w_s}{\partial x}\right)\left(\frac{\partial w_d}{\partial x}\right)\left(\frac{\partial^2 w_s}{\partial x^2}+\frac{\upsilon}{\alpha^2}\frac{\partial^2 w_s}{\partial y^2}\right)\\ +\frac{1}{2\alpha^2}\left(\frac{\partial w_s}{\partial y}\right)^2\left(\upsilon\frac{\partial^2 w_d}{\partial x^2}+\frac{1}{\alpha^2}\frac{\partial^2 w_d}{\partial y^2}\right)+\frac{1}{2\alpha^2}\left(\frac{\partial w_s}{\partial y}\right)\left(\frac{\partial w_d}{\partial y}\right)\left(\upsilon\frac{\partial^2 w_s}{\partial x^2}+\frac{1}{\alpha^2}\frac{\partial^2 w_s}{\partial y^2}\right)\\ +\frac{(1-\upsilon)}{\alpha^2}\left(\frac{\partial w_s}{\partial x}\frac{\partial w_s}{\partial y}\frac{\partial^2 w_d}{\partial x\partial y}\right)+\frac{(1-\upsilon)}{\alpha^2}\left(\frac{\partial w_s}{\partial x}\frac{\partial w_d}{\partial y}\frac{\partial^2 w_s}{\partial x\partial y}\right)+\frac{(1-\upsilon)}{\alpha^2}\left(\frac{\partial w_d}{\partial x}\frac{\partial w_s}{\partial y}\frac{\partial^2 w_s}{\partial x\partial y}\right)\end{array}\right\} \tag{3.27}$$

Equations (3.25)-(3.27) are the linearized governing equations of a microplate initially deflected by an electrostatic DC load. These equations are not suitable for analyzing large amplitude vibration of the plates; and hence will be only used to determine the eigenvalues under the action of the electrostatic forces. The forced vibration analysis will be based on the full nonlinear equations (3.10)-(3.12).

3.3. Reduced Order Models

In this section we discuss the various approaches to develop the reduced order model for the governing equations.

3.3.1. Model I

In the first approach we develop a semi-reduced order model (semi-ROM) of the governing equations (3.10)-(3.12). The governing equation of the out-of-plane motion, equation (3.12), is reduced into a finite-degree-of-freedom system using the Galerkin method. We use the product of beam mode shapes along x and y as basis functions in the Galerkin procedure. Hence, we express the out-of-plane deflection w as

$$w = \sum_{i=1}^{m} q_i(t)\phi_i^{j,k}(x,y) \tag{3.28}$$

where $\phi_i^{j,k}(x,y)$ are the basis functions constructed by taking product of the clamped-clamped beam modes; jth mode along x and kth mode along y axis, $j,k = 1,3,5\ldots$, and $q_i(t)$ are the unknown time dependent coefficients. We multiply equation (3.12) by $(1-w)^2$ to incorporate the electric force term exactly and simplify dealing with the electrostatic force term. Substituting equation (3.28) into equation (3.12), multiplying by $\phi_i^{j,k}(x,y)$ and integrating over the plate domain we obtain a discretized form of the out-of-plane equation of motion. The result is a system of nonlinear ordinary differential equations (ODEs) in the time dependent coefficients $q_i(t)$, coupled with the in-plane partial differential equations (3.10) and (3.11).

This semi-ROM is solved iteratively using a combination of the Runge Kutta method along with the method of lines. The numerical method of lines is a technique for solving partial differential equations by discretizing in all but one dimension and then integrating

the semi-discrete problem as a system of ODEs or DAEs [81]. The solution method of model I is outlined in the following:

1. First we put $u = 0$ and $v = 0$ into the system of discretized ODEs, apply the direct voltage V_{dc} and solve for the out-of-plane deflection w.
2. Next plug the deflection w into equations (3.10) and (3.11) and solve them for u and v.
3. Next the solution for u and v is substituted into the system of ODEs to solve for the deflection w under an applied voltage V_{dc}.
4. Repeat the procedure until a converged solution for w is obtained.

This model can work well for static simulations. However, it is not convenient for dynamic analysis due to its iterative nature.

3.3.2. Model II

In the second approach we develop a full ROM of the governing equations (3.10)-(3.12). The difference between this model and model I is that we discretize all three equations of motion using beam mode shapes. The Galerkin procedure for the out-of-plane motion, equation (3.12), is the same as described in model I. To discretize equations (3.10) and (3.11) of the in-plane motion, we express the in-plane displacements u and v as

$$u = q_u(t)\phi^{2,1}(x, y) \tag{3.29}$$

$$v = q_v(t)\phi^{1,2}(x, y) \tag{3.30}$$

where $\phi^{2,1}(x, y)$ and $\phi^{1,2}(x, y)$ are the shape-functions constructed by multiplying mode shapes of a clamped-clamped beam; where the first superscript refers to the mode along

the x axis and the second superscript refers to the mode along the y axis, $q_u(t)$ and $q_v(t)$ are the corresponding time dependent coefficients. Substituting equations (3.29) and (3.30) into equations (3.10) and (3.11), respectively, multiplying by $\phi^{2,1}(x,y)$ and $\phi^{1,2}(x,y)$, respectively, and integrating over the plate domain we get a set of algebraic equations in the time dependent coefficients $q_u(t)$ and $q_v(t)$. This set of algebraic equations combined with the system of nonlinear ODEs produced in model I constitute the full ROM of the governing equations. Numerical integration of the system of differential algebraic equations (DAEs) can be performed using the Runge Kutta method to obtain a solution for the time dependent coefficients $q_i(t)$, $q_u(t)$ and $q_v(t)$, which are substituted back into equations (3.28)-(3.30) to get w, u and v.

3.3.3. Model III

In the third model, we use the mode shapes of the plate calculated using a FEM analysis as the basis functions in the Galerkin procedure. We use the commercial software COMSOL [82] to obtain the mode shapes of the plate. Accordingly, we express the displacement variables w, u and v as

$$w = \sum_{i=1}^{m} q_i(t)\phi_i(x,y) \tag{3.31}$$

$$u = q_u(t)\psi_u(x,y) \tag{3.32}$$

$$v = q_v(t)\psi_v(x,y) \tag{3.33}$$

where $\phi_i(x,y)$ are out-of-plane mode shapes of the plate while $\psi_u(x,y)$ and $\psi_v(x,y)$ are the in-plane mode shapes and $q_i(t)$, $q_u(t)$ and $q_v(t)$ are the corresponding unknown time

dependent coefficients. Equation (3.12) is multiplied by $(1-w)^2$ to treat the electric force term in its exact form. Substituting equations (3.31)-(3.33) into equations (3.10)-(3.12), multiplying equation (3.12) by $\phi_i(x,y)$ and equations (3.10) and (3.11) by $\psi_u(x,y)$ and $\psi_v(x,y)$, respectively, and integrating over the domain we get the reduced order model of the governing equations. The reduced order model comprises of a system of differential algebraic equations (DAEs) in the unknown time dependent coefficients $q_i(t)$, $q_u(t)$ and $q_v(t)$, which as before can be solved for $q_i(t)$, $q_u(t)$ and $q_v(t)$ using the Runge Kutta method.

3.3.4. Model IV

This model is similar to model III; the deflection and in-plane displacement variables w, u and v are expressed as in equations (3.31)-(3.33). In this model $\phi_i(x,y)$ are the same out-of-plane mode shapes of the plate, obtained using FEM, while $\psi_u(x,y)$ and $\psi_v(x,y)$ are the shape functions for the in-plane displacements u and v. Here, we do not use regular mode shapes for the in-plane displacement. Instead, we make use of the fact that the in-plane inertia is negligible, and hence, obtain instead, in-plane shape functions from FEM assuming the plate is deflected by a uniform transverse pressure. Both mode shapes $\phi_i(x,y)$ and shape functions $\psi_u(x,y)$ and $\psi_v(x,y)$ are obtained using the FEM Software COMSOL. A mesh convergence test is run to choose a suitable mesh. Results of the mesh convergence test and the mode shapes of the plate along with the in-plane displacement shape functions are given in the Appendix. Other than the basis functions,

the Galerkin procedure is the same as in model III and the resulting ROM consists of DAEs as well.

3.3.5. Model V

This approach follows the method outlined in [83]. In this approach, the out-of-plane deflection w is expressed as in equation (3.31). Substituting equation (3.31) into equations (3.10) and (3.11) we obtain the following equations:

$$\frac{\partial^2 u}{\partial x^2}+\frac{(1+\upsilon)}{2\alpha}\frac{\partial^2 v}{\partial x\partial y}+\frac{(1-\upsilon)}{2\alpha^2}\frac{\partial^2 u}{\partial y^2}+\sum_{k,l}q_k q_l\left[\left(\frac{\partial\phi_k}{\partial x}\frac{\partial^2\phi_l}{\partial x^2}+\frac{(1+\upsilon)}{2\alpha^2}\frac{\partial\phi_k}{\partial y}\frac{\partial^2\phi_l}{\partial x\partial y}\right)+\frac{(1-\upsilon)}{2\alpha^2}\left(\frac{\partial\phi_k}{\partial x}\frac{\partial^2\phi_l}{\partial y^2}\right)\right]=0 \tag{3.34}$$

$$\frac{\partial^2 v}{\partial y^2}+\frac{(1+\upsilon)\alpha}{2}\frac{\partial^2 u}{\partial x\partial y}+\frac{(1-\upsilon)\alpha^2}{2}\frac{\partial^2 v}{\partial x^2}+\sum_{k,l}q_k q_l\left[\left(\frac{1}{\alpha}\frac{\partial\phi_k}{\partial y}\frac{\partial^2\phi_l}{\partial y^2}+\frac{(1+\upsilon)\alpha}{2}\frac{\partial\phi_k}{\partial x}\frac{\partial^2\phi_l}{\partial x\partial y}\right)+\frac{(1-\upsilon)}{2}\left(\frac{\partial\phi_k}{\partial y}\frac{\partial^2\phi_l}{\partial x^2}\right)\right]=0 \tag{3.35}$$

Equations (3.34) and (3.35) are nonhomogeneous coupled linear PDEs in u and v. Since these equations are linear in *u* and *v*, the principle of superposition can be used to determine the solution for u and v in the form [83]

$$u=\sum_{k,l}q_k q_l u^{kl} \tag{3.36}$$

$$v=\sum_{k,l}q_k q_l v^{kl} \tag{3.37}$$

where the superscript kl denotes the in-plane displacements u^{kl} and v^{kl} caused by the loads f_x^{kl} and f_y^{kl} defined as

$$f_x^{kl}=\left(\frac{\partial\phi_k}{\partial x}\frac{\partial^2\phi_l}{\partial x^2}+\frac{(1+\upsilon)}{2\alpha^2}\frac{\partial\phi_k}{\partial y}\frac{\partial^2\phi_l}{\partial x\partial y}\right)+\frac{(1-\upsilon)}{2\alpha^2}\left(\frac{\partial\phi_k}{\partial x}\frac{\partial^2\phi_l}{\partial y^2}\right) \tag{3.38}$$

$$f_y^{kl}=\left(\frac{1}{\alpha}\frac{\partial\phi_k}{\partial y}\frac{\partial^2\phi_l}{\partial y^2}+\frac{(1+\upsilon)\alpha}{2}\frac{\partial\phi_k}{\partial x}\frac{\partial^2\phi_l}{\partial x\partial y}\right)+\frac{(1-\upsilon)}{2}\left(\frac{\partial\phi_k}{\partial y}\frac{\partial^2\phi_l}{\partial x^2}\right) \tag{3.39}$$

Equation (3.12) is multiplied by $(1-w)^2$ to treat the electric force term exactly with no approximation. Now by substituting equations (3.31), (3.36), and (3.37) into equation (3.12), multiplying by $\phi_i(x,y)$ and integrating over the plate domain we get the reduced order model for the governing equations. The reduced order model consists of a system of nonlinear coupled ODEs in $q_i(t)$. This system of ODEs is solved for $q_i(t)$ numerically using the Runge Kutta method and is substituted back into equation (3.31), (3.36), and (3.37) to obtain w, u and v, respectively.

3.4. Static Analysis

To calculate the static deflection of the microplate under a DC load, $V(t)$ is replaced by V_{dc}. We then drop the time derivatives in all the models and the time dependent unknown coefficient $q_i(t)$ in the semi-ROM, and $q_i(t)$, $q_u(t)$ and $q_v(t)$ in all the other models are written as constant coefficients q_i, q_u and q_v. This results in a system of nonlinear algebraic equations, which is numerically solved for q_i in case of the semi-ROM and q_i, q_u and q_v in all the other models. Then equation (3.28) or equation (3.31) is used to find the transverse deflection.

First we study the convergence of the static results with the number of transverse modes, $\phi_i(x,y)$ retained in the reduced order model when $\alpha = 1$ and $\alpha_1 = 1$. Figure 3.2 shows the stable solutions, the non-dimensional deflection $W_{\max}$ at the center of the plate against various values of $\alpha_2 V_{dc}^{\ 2}$. These convergence static results are based on non-dimensional parameters and hence are not specific to any plate of a particular geometry or material.

A summary of the convergence results for all the approaches is given in Table 3.1. Figure 3.2 indicates a classical behavior of electrostatically actuated microstructures, where the deflection slopes approaches infinity at the pull-in voltage, where the structure collapses to the substrate [7]. As clear from the figure and the table, Models I and II require in total six transversal mode shapes for convergence, while models III-V require four.

Table 3.1: Summary of convergence studies, number of transverse modes required for convergence and the value of the non-dimensional parameter $\alpha_2 V_{dc}^{\ 2}$ at the pull-in instability.

Model No.	No. of modes for convergence	Voltage parameter $\alpha_2 V_{dc}^{\ 2}$
Model I	6	188
Model II	6	191
Model III	4	186
Model IV	4	194
Model V	4	192

3.5. Model Validation

For validation purpose, the static response calculated by the reduced order models is compared with the results obtained from a FE model implemented in COMSOL [82]. The Electro-mechanics module of COMSOL was used to model the electrically actuated microplate. A mapped mesh with fifty divisions along each edge was used. The geometric and material parameters used are; $a = b = 300\mu\text{m}$, $h = 2\mu\text{m}$, $d = 2\mu\text{m}$, $E = 153\text{GPa}$ and $\upsilon = 0.23$. Since this is a geometrically nonlinear problem, geometric nonlinearity is activated before performing the analysis. Figure 3.3 shows the maximum

deflection $W_{\max}$ at the center of the microplate against V_{dc} up to the pull-in instability. The figure shows excellent agreement between the results calculated by the ROMs and the FE model except for model III. Model III predicts the pull-in of the microplate at a lower voltage. This means that it does not account for the cubic nonlinearity accurately and only captures the effect of midplane stretching partially. In other words, we can remark that the shape functions used to represent the in-plane displacements are not accurate enough to capture the full effect of midplane stretching. All the other models accurately predict the static response of the microplate.

Although accurate, models I and II require more computational effort as compared with models IV and V. Nevertheless they use easy-to-handle analytical functions as basis function in the discretization procedure. Model V calculates exact solution for the in-plane displacement u and v, hence requires more computational effort to integrate over the plate domain as compared with model IV, which approximates the solution through equations (3.32) and (3.33).

Reduced order models are known to be computationally efficient as compared with the full order finite element models. To highlight the advantage of using reduced order models over finite element model, we compare the time taken to solve the system when a DC voltage, $V_{dc} = 60\text{V}$ was applied. Results for this comparison are given in Table 3.2. One can note that the time taken by full order FE model is much higher than the reduced order model because it solves thousands of equations one for each degree of freedom [43].

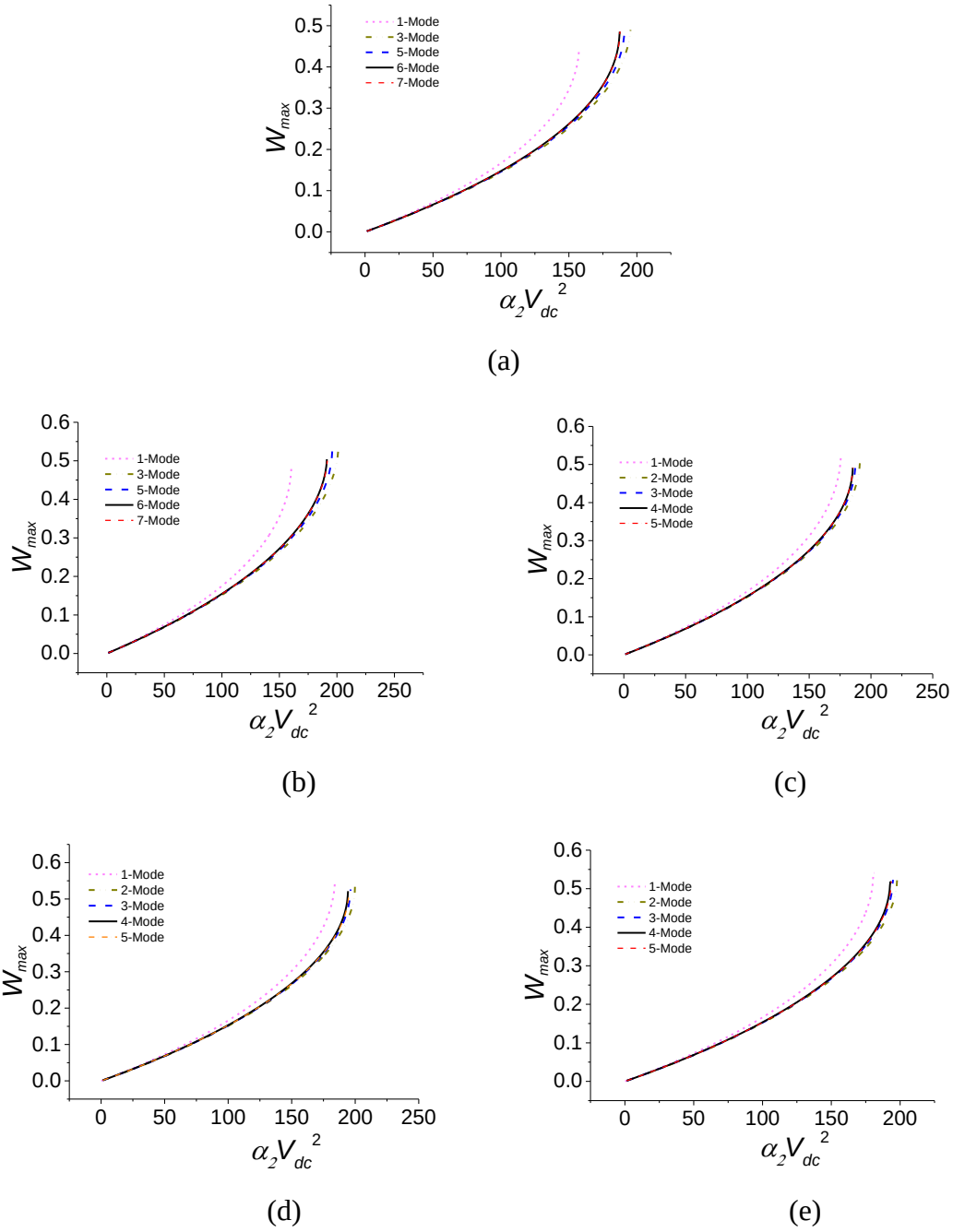

Figure 3.2: Convergence of the static results with the number of transversal mode shapes retained in the reduced order models. Variation of the maximum non-dimensional deflection $W_{\max}$ at the center of the microplate with the electrostatic voltage parameter $\alpha_2 V_{dc}^{\ 2}$ when $\alpha = 1$, and $\alpha_1 = 1$: (a) model I, (b) model II, (c) model III, (d) model IV, (e) model V.

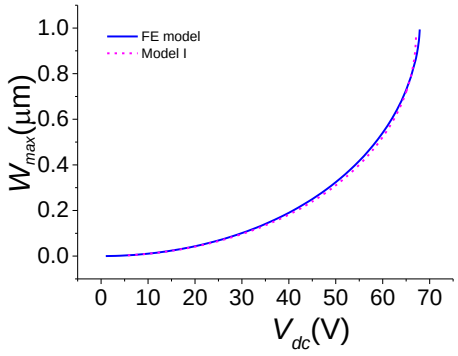

(a)

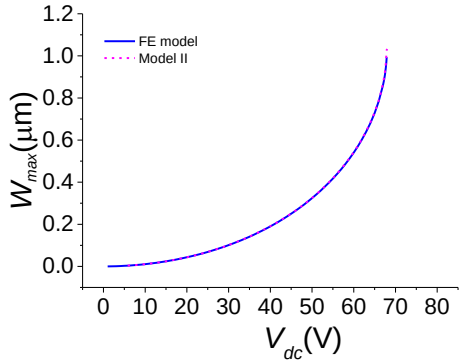

(b)

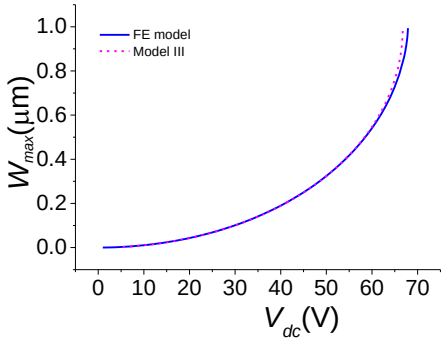

(c)

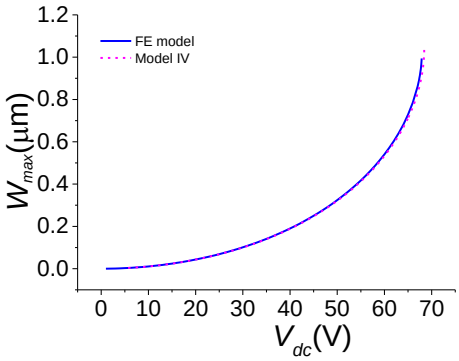

(d)

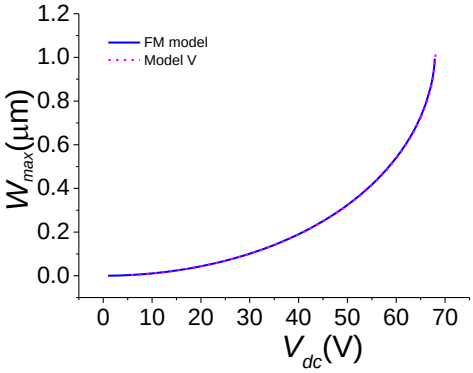

(e)

Figure 3.3: A comparison of the maximum deflection $W_{\max}$ at the center of the plate, calculated by the reduced order models with the results obtained from FE model implemented in COMSOL for various values of V_{dc}, until the pull-in instability: (a) model I, (b) model II, (c) model III, (d) model IV, (e) model V.

Table 3.2: A comparison of the time taken by the FE model implemented in COMSOL and the reduced order models to solve the system under an electrostatic DC voltage.

Model	Time taken (Seconds)
FE model	125
Model II	0.140
Model III	0.046
Model IV	0.046
Model V	0.031

3.6. Dynamic Analysis

First we present the Eigen frequency analysis of the microplate when deflected under the DC voltage V_{dc} . The approaches presented in models II-V are used in conjunction with equations (3.25)-(3.27) to calculate the linear natural frequency of the microplate at different levels of initial deflection w_s under the electrostatic voltage V_{dc} , until the pull-in instability. The results are compared in Figure 3.4 with the natural frequencies calculated by the FE model implemented in COMSOL. Model I is not included in the analysis due to its iterative nature. Results calculated by the ROMs show good agreement with the ones calculated by FEM model except for model III, which shows significant deviation. This result agrees with the static results and confirms the remark that model III does not account accurately for the cubic nonlinearity due to midplane stretching and that the shape functions used to represent the in-plane displacements are not accurate enough to capture the full effect of midplane stretching.

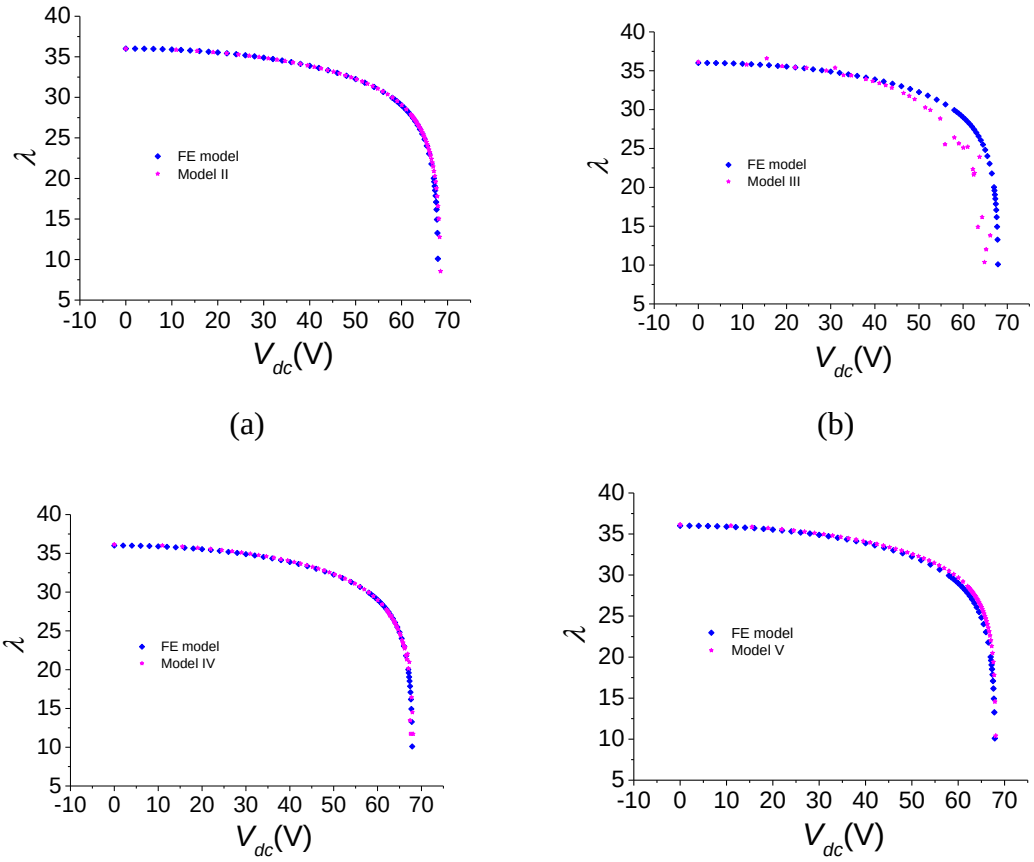

Figure 3.4: The non-dimensional fundamental natural frequency ($\lambda = \omega a^2 \sqrt{\frac{\rho}{D}}$) of a square microplate for different levels of V_{dc} until pull-in (stars). Comparison with the results computed by the FE model implemented in COMSOL (diamonds): (a) model II, (b) model III, (c) model IV, (d) model V.

Models II, IV and V accurately predict the non-dimensional natural frequencies of the microplate. Although accurate, model II entails more computational effort as compared with models IV and V, since it requires more modes for convergence. However it employs easy-to-use analytical functions as basis functions in the Galerkin discretization procedure. Model IV approximates the solution for the in-plane displacements u and v

through equations (3.32) and (3.33) while model V calculates exact solution, hence requires more computational effort to integrate over the plate domain. Nonetheless model V is easily adaptable to the microplates with other boundary conditions e.g. clamped-free-clamped-free (CFCF). Moreover one can note that the natural frequency decreases with the increase of the applied DC voltage and drops rapidly near the pull-in instability, finally falling to zero at the pull-in instability. This is due to the softening nature of the electrostatic force, here by softening we mean that the natural frequency decreases with increase of the electrostatic load. The decrease in the natural frequency of the plate with the increase in the DC load means that its elastic restoring force is weakening, and hence reaches eventually to zero when the natural frequency vanishes.

Next we present the dynamic response of the microplate calculated by models II-V, when actuated with small and large electrostatic forces. Frequency response curves are generated by actuating the microplate by a harmonic load of amplitude V_{ac} superimposed to V_{dc} load, i.e., $V(\mathrm{t}) = V_{dc} + V_{ac} Sin(\Omega \mathrm{t})$. The Runge Kutta method is used to perform long time numerical integration to solve the system of governing equations to obtain a stable steady solution. A stable steady solution is captured such that the transient response is not contributing to the solution. We fix the non-dimensional parameters as $\alpha = 1$, $\alpha_1 = 1$, and $\alpha_2 = 1$, and assume that the in-plane external forces are zero i.e. $N_{xx} = N_{xy} = N_{yy} = 0$. To get a linear response, we actuate the microplate at a small load of $V_{dc} = 1\mathrm{V}$ and a harmonic load of $V_{ac} = 0.01\mathrm{V}$. For the large vibration response we use $V_{ac} = 1\mathrm{V}$ while V_{dc} is kept the same. Figure 3.5 shows a comparison of the dynamic responses calculated by models II-

V using frequency response curves for the small and large amplitude vibrations of the microplate.

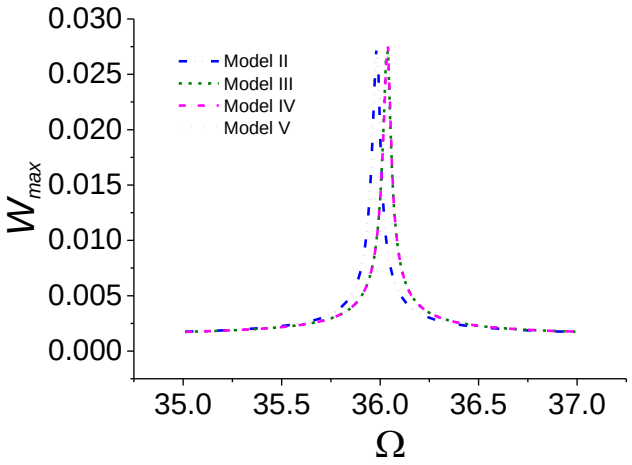

(a)

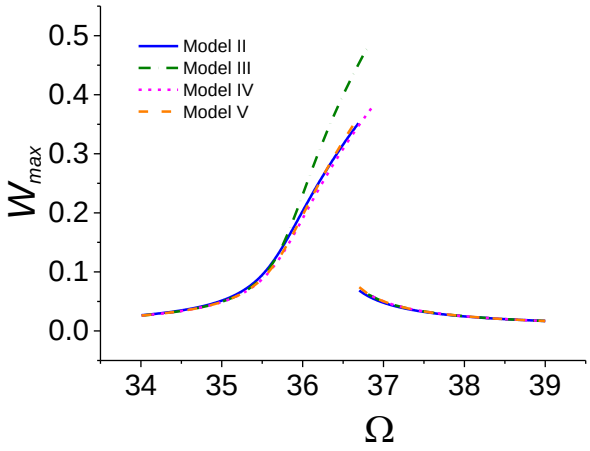

(b)

Figure 3.5: Frequency response curves near the non-dimensional fundamental natural frequency, maximum non-dimensional deflection $W_{\max}\left(a/2, b/2\right)$ of the microplate against actuating frequency Ω. Response is captured at $V_{dc}=1\text{V}$ and (a) $V_{ac}=0.01\text{V}$, (b) $V_{ac}=1\text{V}$, when $\alpha=1$, $\alpha_1=1, \alpha_2=1$ and a quality factor $Q=1000$.

All the models show good agreement when actuated at small electrostatic loads (Figure 3.5A). All the models show the linear response very close to each other, model II shows a slight difference of less than 1% from other models. This small difference from other models appears due to the different kind of shape functions used in this model, which seems not of good accuracy.

Model III shows a significant deviation from the other models (Figure 3.5B), which show excellent agreement when actuated at large electrostatic loads. This agrees with the static and natural frequency results and ratifies the remark that model III does not account accurately for the cubic nonlinearity. For small actuating forces (Figure 3.5a), all the models show a resonance near the fundamental natural frequency of the plate. The geometric nonlinearity is not activated, and in this regime, the linear plate theory can be used. When large electrostatic loads are used to actuate the large amplitude vibrations of the plate (Figure 3.5b), the geometric nonlinearity due to midplane stretching is activated. The plate shows strong hardening behavior due to the geometric nonlinearity, where the nonlinear resonances appear at higher frequencies. All the models capture the nonlinear hardening responses of the plate accurately except model III, which fails to capture the nonlinearity accurately. In this regime, the linear plate theory fails and only a model that accounts for the geometric nonlinearity can capture the plate response accurately.

Although it sounds appropriate to use any of the models II, IV and V for the investigation of large amplitude vibrations of microplates, we believe that model V is the most accurate one since it calculates the exact solution for midplane stretching while for all the other models we approximate the in-plane displacements using some kind of shape

functions. Moreover it can be used with confidence for microplates with other boundary conditions for example a clamped-free-clamped-free (CFCF) microplate. For such a case the other models may not be used with the same shape functions. So model V is more rigorous and versatile and can be used for a microplate with any kind of boundary conditions.

Chapter 4

An Investigation of the Static and Dynamic Behavior of Electrically Actuated Rectangular Microplates

In this chapter, we present an investigation of the static and dynamic behavior of the nonlinear von-Karman plates when actuated by the nonlinear electrostatic forces. The investigation is based on a reduced order model developed using the Galerkin method, which rely on mode shapes and in-plane shape functions extracted using a finite element method. In this study, a fully clamped microplate is considered. We investigate the static behavior and the effect of different non-dimensional design parameters. The static results are validated by comparison with the results calculated by a finite element model. The forced-vibration response of the plate is then investigated when the plate is excited by a harmonic AC load superimposed to a DC load. The dynamic behavior is examined near the primary and secondary (superharmonic and subharmonic) resonances. The microplate shows a strong hardening behavior due to the cubic nonlinearity of midplane stretching. However, the behavior switches to softening as the DC load is increased. Finally, near-square plates are studied to understand the effect of geometric imperfections of microplates.

4.1. Introduction

In Chapter 3 we have investigated various approaches to develop reduced order model. In this chapter we study the static and dynamic behavior of fully clamped rectangular plates under electrostatic actuation. We use the reduced order model IV presented in Chapter 3 for this investigation. The reduced order model is based on the von-Karman equations of the plate, in which all three equations of the plate motion are discretized using the Galerkin method. For validation purpose, we compare the static results computed by the reduced order model with the results calculated using the FEM software COMSOL [82]. Further the reduced order model is employed to investigate the nonlinear, large amplitude vibration behavior of the plates. Understanding the nonlinear behavior of microplates when actuated by large electrostatic loading or when undergoing large motion is fundamental to the development of the next generation microplates-based MEMS devices.

We use the problem formulation and reduced order model IV presented in Chapter 3. The reduced order model is based on the dynamic analogue of nonlinear von-Karman equations of thin plate.

The reduced order model, which consist of DAEs is solved for the unknown time dependent coefficients $q_i(t)$, $q_u(t)$ and $q_v(t)$. Toward this, we solve equations (3.10) and (3.11) for $q_u(t)$ and $q_v(t)$ in terms of $q_i(t)$ and then substitute the results into equation (3.12). This equation is then integrated in time using Runge Kutta. These coefficients are substituted back into equations (3.31)-(3.33) to get the displacements w, u and v.

4.2. Static Analysis

Convergence study of the static results with the number of transverse modes, $\phi_i(x,y)$ retained in the reduced order model was performed in Chapter 3 and it was found that four transverse modes are sufficient to get reasonably accurate result. Moreover the model was also validated by comparing results with the results obtained by FE model.

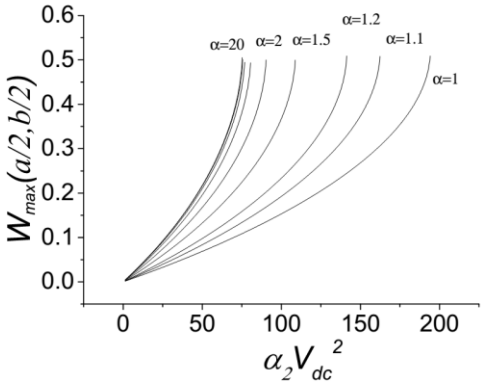

Figure 4.1: Variation of the maximum non-dimensional deflection $W_{\max}$ at the center of the microplate with the electrostatic voltage parameter $\alpha_2 V_{dc}^2$ until pull-in for various values of aspect ratio α when $\alpha_1 = 1$.

Here we investigate the effect of different non-dimensional parameters on the static response of the plate. Figure 4.1 shows the maximum non-dimensional deflection $W_{\max}$ against $\alpha_2 V_{dc}^2$ for various values of the aspect ratio α with fixed value of $\alpha_1 = 1$. By increasing α, the maximum deflection almost remains constant, but the voltage instability threshold (pull-in) decreases and saturates near $\alpha_2 V_{dc}^2 = 75$ as the aspect ratio α approaches ∞. Figure 4.2 shows the variation of $W_{\max}$ with $\alpha_2 V_{dc}^2$ until pull-in

occurs for various values of α_1 while $\alpha = 1$ (square plate). We notice that the maximum non-dimensional deflection $W_{\max}$ as well as the voltage parameter $\alpha_2 V_{dc}^{\ 2}$ are reduced for $\alpha_1 < 1$, while for $\alpha_1 > 1$ both quantities increase and $W_{\max}$ seems to stabilize near 0.7 at $\alpha_1 \geq 3$.

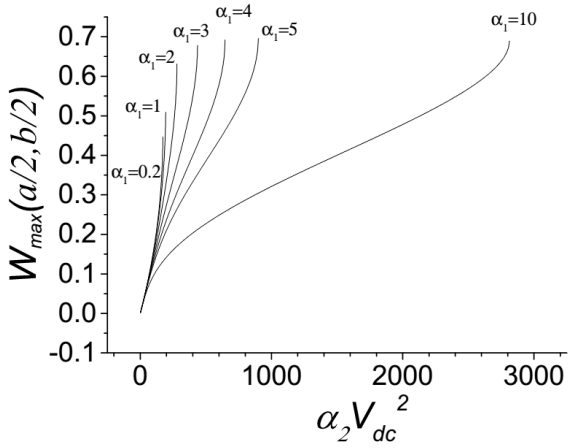

Figure 4.2: Variation of the non-dimensional deflection $W_{\max}$ at the center of the microplate with the electrostatic voltage parameter $\alpha_2 V_{dc}^{\ 2}$ until pull-in for various values of α_1 when $\alpha = 1$.

4.3. Dynamic Analysis

In this section we investigate the dynamic response of the square microplate at primary, super-harmonic of order three, and sub-harmonic of order two resonances of the fundamental mode. We analyze the dynamics of the microplate by generating frequency response curves. The Runge Kutta method is used to perform long time numerical integration to solve the system of DAEs. The stable steady-state solution is captured after

making sure that the transient response is no longer contributing to the response. Figure 4.3 shows the time history of the dynamic response of the microplate when actuated at a DC voltage $V_{dc} = 3\text{V}$ and an AC voltage $V_{ac} = 0.1\text{V}$ and $\Omega = 35.1$. Figure 4.3a depicts the diminishing transient response, while Figure 4.3b shows the stable steady-state response. We use steady-state responses similar to Figure 4.3b to construct the frequency response curves.

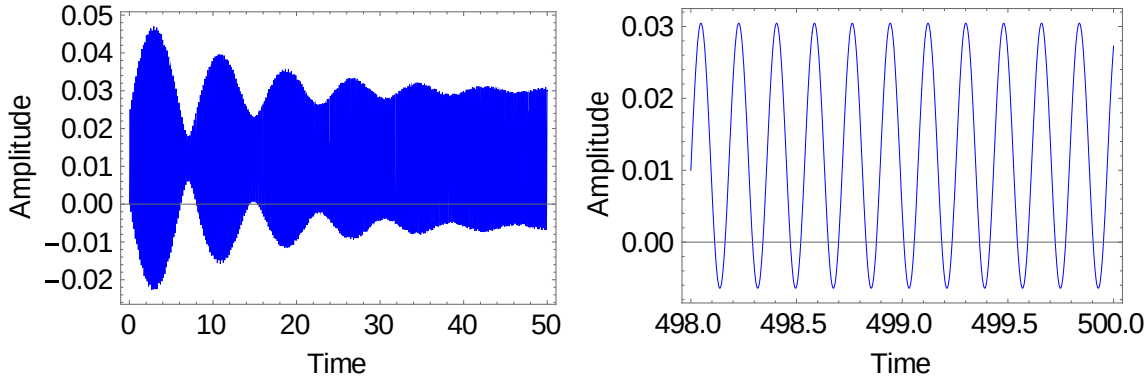

(a) (b)

Figure 4.3: Time history response of the microplate. (a) Transient response. (b) Steady state response.

4.3.1. Primary Resonance

To investigate the dynamic response at primary resonance, we fix $\alpha = 1$, $\alpha_1 = 1, \alpha_2 = 1$ and assume that the in-plane external forces are zero i.e. $\hat{N}_1 = \hat{N}_{12} = \hat{N}_2 = 0$. With the above parameters the static pull-in voltage for the microplate is near 14 Volts. We investigate the nonlinear dynamic behavior of the microplate near primary resonance at a small harmonic AC voltage, V_{ac} superimposed to a DC voltage, V_{dc} , i.e., $V(\text{t}) = V_{dc} + V_{ac} Sin(\Omega \text{t})$. Figure 4.4 shows the nonlinear response of the microplate when actuated at $V_{dc} = 3\text{V}$ for

various values of V_{ac} near primary resonance, which for the linear plate is near 36. The quality factor is fixed at $Q = 250$, which is related to the damping coefficient by $c = \frac{\omega_1}{Q}$ [84]. Our choice of a constant value of Q means that we assumed negligible effect of squeeze-film damping, which is reasonable assumption assuming that the microplate is placed inside a vacuum chamber and is operated at reduced pressure. Otherwise, squeeze-film damping can have strong effect on the dynamics of microplates and needs to be modeled using Reynolds equation and a structural-fluidic model [7, 48].

Figure 4.4 shows the maximum non-dimensional deflection $W_{\max}$ at the center of the microplate against the non-dimensional frequency.

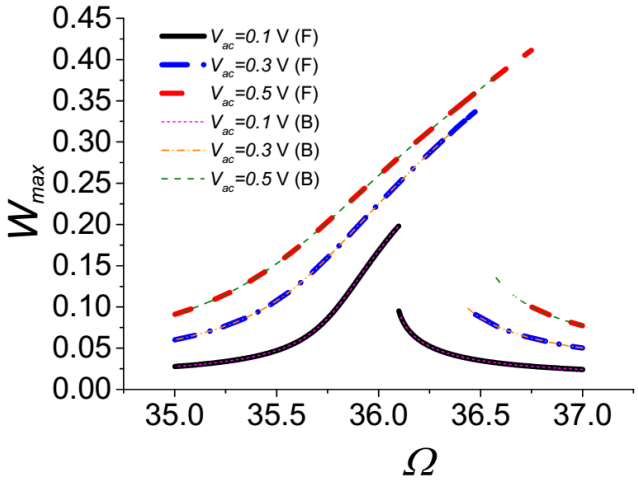

Figure 4.4: Maximum non-dimensional deflection $W_{\max}$ at the center of the microplate against the actuating frequency Ω when actuated at $V_{dc} = 3\text{V}$ and various values of V_{ac} while quality factor $Q = 250$; (F) forward frequency sweep, (B) backward frequency sweep.

The microplate exhibits strong hardening effect due to the cubic nonlinearity, which comes into play due to midplane stretching. The hysteresis in the curves is captured by performing forward and backward frequency sweeps. Nonlinear resonance peaks occur near $\Omega = 36.15$ for $V_{ac} = 0.1\text{V}$ while it is at $\Omega = 36.6$ for $V_{ac} = 0.3\text{V}$ and $\Omega = 36.9$ for $V_{ac} = 0.5\text{V}$. Further we notice that there exist multiple stable solutions over some range of frequency and amplitude jumps from higher to lower or lower to higher values depending on the type of frequency sweep.

Figure 4.5 shows the frequency response curves of the microplate when actuated at $V_{dc} = 7\text{V}$ for various values of V_{ac} with a quality factor $Q = 250$. An overlap of stable solutions exists when actuated at $V_{ac} = 0.2\text{V}$ contrary to the responses at $V_{ac} = 0.4\text{V}$ and $V_{ac} = 0.6\text{V}$, respectively.

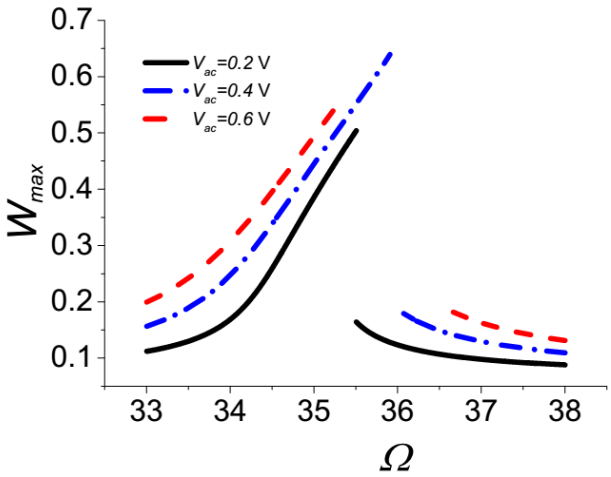

Figure 4.5: Maximum non-dimensional deflection $W_{\max}$ at the center of the microplate against the actuating frequency Ω when actuated at $V_{dc} = 7\text{V}$ and various values of V_{ac} while quality factor $Q = 250$.

A gap between the two stable solutions starts to emerge in the case of $V_{ac} = 0.4\text{V}$ by the forward and backward frequency sweeps. This gap might indicate that the microplate becomes unstable at that actuating voltage and pulls on the stationary electrode. This kind of instability is called dynamic pull-in instability, which usually occurs at a lower DC load superimposed to a small harmonic load [7, 24, 84, 85]. Another possibility exists, especially in the case of $V_{ac} = 0.4\text{V}$, that this gap is created due to the numerical divergence of the time integration scheme, due to its inability to find suitable initial conditions that lead to a stable periodic orbit. In other words, this might indicate highly fractal behavior, which usually gets stronger as the system approaches the dynamic pull-in regime [85] .To confirm if this divergence is due to fractal behavior or due to pull-in exactly, one should resort to other numerical techniques to find periodic motions, such as shooting and finite difference methods as well as basin of attraction analysis [7, 84]. The response on the other hand for the case of $V_{ac} = 0.6\text{V}$ is most likely an indication of a pull-in band, since as reported in [84], further increase in V_{ac} widens the pull-in band gap between the stable solutions and makes the upper stable branches terminated at lower values [84].

4.3.2. Secondary Resonances

Due to the cubic nonlinearity from midplane stretching and quadratic nonlinearity of the electrostatic force, the plate is expected to exhibit several secondary resonances [7, 86]. These include super harmonic resonances near one-third and one-half the fundamental natural frequency as well as subharmonic resonances near twice and three times the fundamental natural frequency. As case studies, in this paper, we investigate the dynamic

response of the microplate near the super-harmonic resonance of order three and then near the subharmonic resonance of order half. We use the non-dimensional parameters of Section 4.4.1.

A. Super-harmonic Resonance at $\frac{\omega_1}{3}$

The generated frequency response curves reveal some interesting phenomena in this case. First, Figure 4.6 shows the response at $V_{dc} = 9\text{V}$ for various values of V_{ac}.

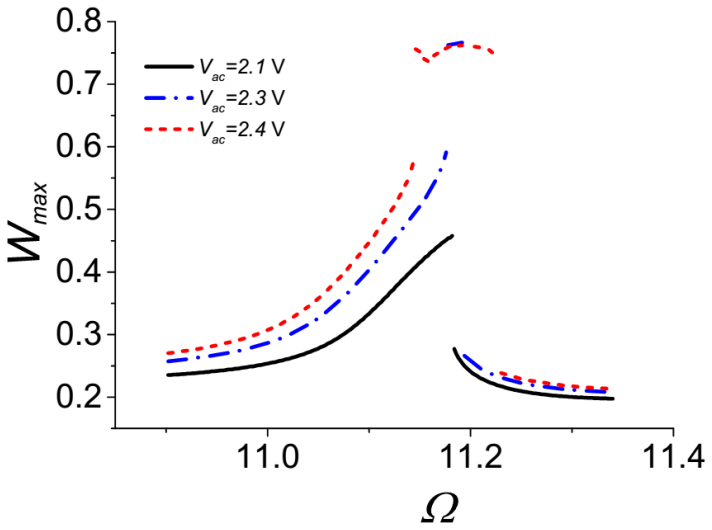

Figure 4.6: Frequency response curves near super-harmonic resonance, $\frac{\omega_1}{3}$ of the fundamental natural frequency. Maximum non-dimensional deflection $W_{\max}$ at the center of the microplate against the actuating frequency Ω when actuated at $V_{dc} = 9\text{V}$ and various values of V_{ac} while quality factor $Q = 250$.

The response at $V_{ac} = 2.1\text{V}$ shows a clear hardening behavior. Now increasing the AC voltage to $V_{ac} = 2.3\text{V}$ and $V_{ac} = 2.4\text{V}$, the microplate becomes unstable and jumps to another stable state with higher amplitude of vibration near $W_{\max} = 0.77$.

This behavior is contrary to the one near primary resonance where the microplate jumps onto the stationary electrode as dynamic pull-in. This can be due to the fact that the response is in the verge of shifting from hardening to softening effect. This is clarified in Figure 4.7, which shows the frequency responses at $V_{dc} = 10\text{V}$ for various V_{ac}. Figure 4.6 and Figure 4.7 depict the transition from hardening to softening behavior.

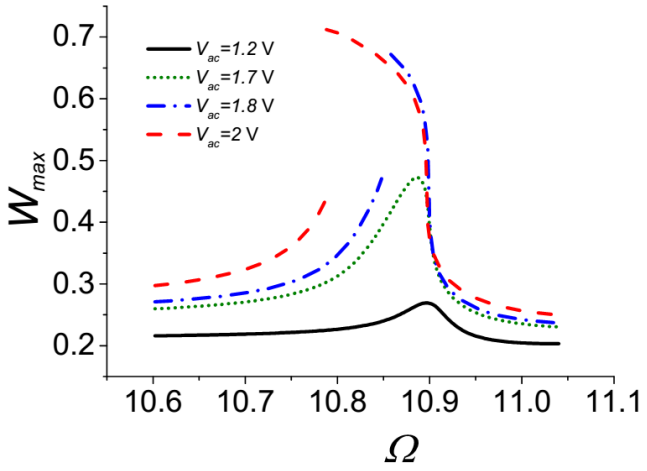

Figure 4.7: Frequency response curves near super-harmonic resonance, $\frac{\omega_1}{3}$ of the fundamental natural frequency. Maximum non-dimensional deflection $W_{\max}$ at the center of the microplate against the actuating frequency Ω when actuated at $V_{dc} = 10\text{V}$ and various values of V_{ac} while quality factor $Q = 250$.

This is expected with the increase of the DC voltage, which tends to change the effective nonlinearity of the system. Essentially, the effective nonlinearity is dominated by the midplane stretching (positive cubic in nature) for low value of DC voltage, and thus the plate exhibits hardening behavior. On the other hand, the electrostatic nonlinearities (quadratic in nature) dominate the overall nonlinearities leading to softening behavior at higher values of DC voltage [7, 87]. This observed behavior is expected also for the primary resonance case. Next, we investigate the amplitude jumps in Figure 4.6 by plotting phase portraits of the response near terminal points of the lower and upper stable branches. Figure 4.8 and 4.9 show the periodic orbits of the stable branches at $V_{ac} = 2.3\text{V}$ and $V_{ac} = 2.4\text{V}$, respectively.

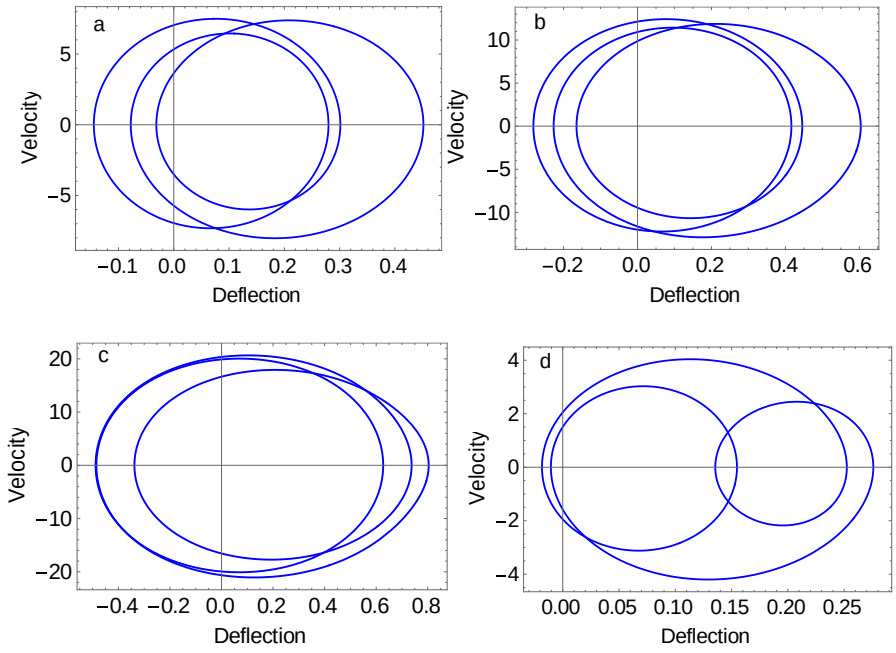

Figure 4.8: Phase portraits for the lower and upper stable branches of the Figure 4.6 for $V_{ac} = 2.3\text{V}$; (a) $\Omega = 11.12$, (b) $\Omega = 11.176$, (c) $\Omega = 11.178$, (d) $\Omega = 11.194$.

Figure 4.8 shows that the orbit size increases as the actuation frequency increases until the maximum value of deflection amplitude $W_{\max} \approx 0.6$ is reached near the terminal point of the lower stable branch at $\Omega = 11.176$. Beyond this point, we note that the plate jumps to a higher amplitude of vibration, $W_{\max} \approx 0.8$ at $\Omega = 11.178$. The plate jumps back to a lower amplitude of vibration, $W_{\max} \approx 0.27$ at $\Omega = 11.194$. A similar response is depicted in Figure 4.9 for a higher AC load.

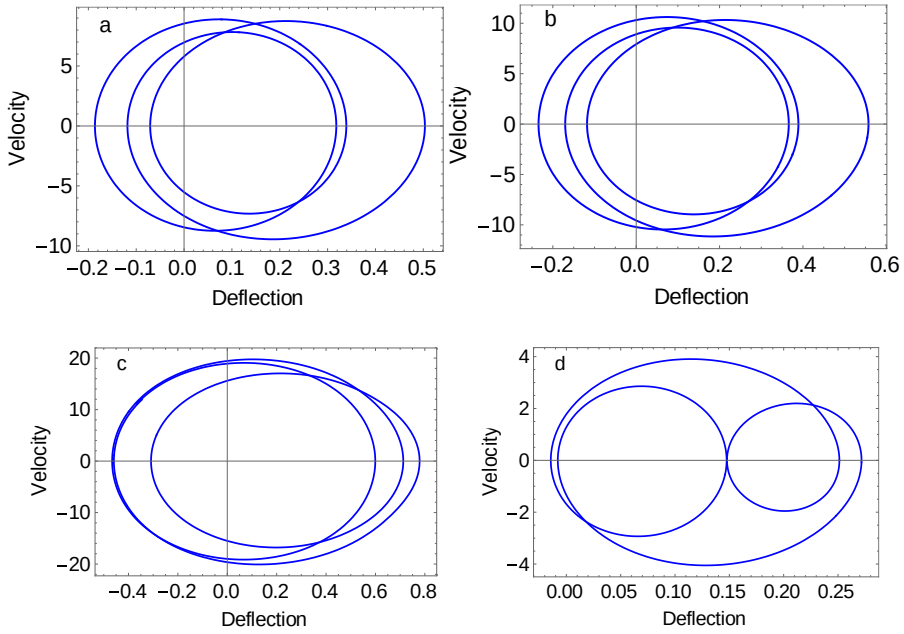

Figure 4.9: Phase portraits for the lower and upper stable branches of the Figure 4.6 for $V_{ac} = 2.4\text{V}$; (a) $\Omega = 11.12$, (b) $\Omega = 11.138$, (c) $\Omega = 11.14$, (d) $\Omega = 11.204$.

A. Sub-harmonic Resonance at $2\omega_1$

In this section we investigate the dynamic response of the plate near sub-harmonic resonance of order one half. Figure 4.10a shows, as expected, a hardening response. This

hardening behavior shifts to softening behavior by further increasing the DC voltage. During this transition, Figure 4.10b, an upper discrete dynamical solution is created of relatively large amplitude (near W_{max} =0.8), similar to the observed behavior in Figure 4.6. Figure 4.10c shows softening behavior at a higher value of DC voltage. The upper stable branch in the case of softening behavior stays high with significantly large amplitude as compared with lower branches for a considerably large band of actuation frequency.

4.3.3. Dynamic Behavior of Imperfect Square Plates

Next, we investigate the dynamic behavior of imperfect square plates near the second symmetric-symmetric mode, which corresponds to symmetric-symmetric degenerate modes of square plates [88-91]. By imperfect square microplate we mean that α is close to 1. Such an imperfection comes practically when fabricating a square plate, which then due to unavoidable fabrication imperfections, will come as a near square plate. We actuate the microplate at small DC and AC voltages. Non-dimensional parameters remain the same as in Section 4.3.1 except α, which we change slightly to introduce the imperfection. A square microplate exhibits degenerate mode due to the symmetrical geometry. Figure 4.11a shows the response of a perfect square plate, i.e., $\alpha = 1$ while Figures 4.11b-d show the responses when α is slightly varied ($\alpha = 0.999$, $\alpha = 0.995$, and $\alpha = 0.99$).

It is shown that slightly varying the value of α breaks the geometrical symmetry and hence the degenerate modes become distinct modes of vibration at distinct frequencies. As a consequence two corresponding resonances appear very close to each other.

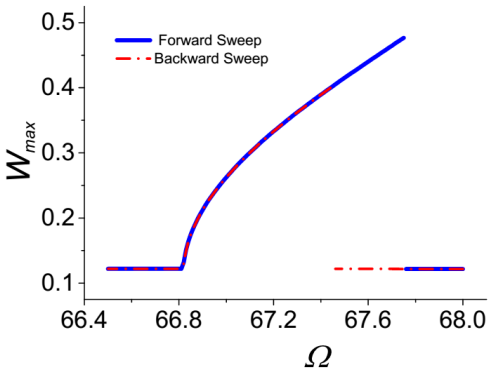

(a) $V_{dc} = 9\text{V}$ and $V_{ac} = 0.5\text{V}$.

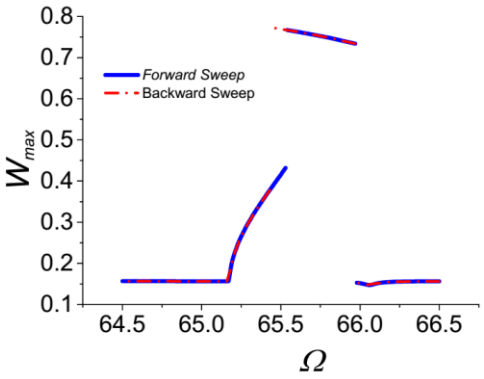

(b) $V_{dc} = 10\text{V}$ and $V_{ac} = 0.5\text{V}$.

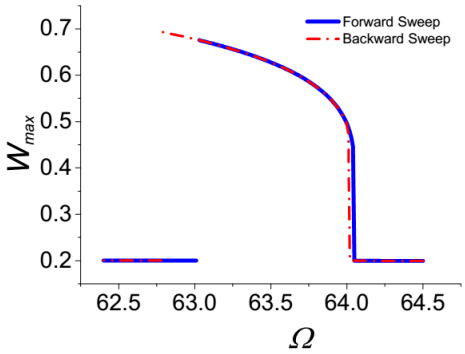

(c) $V_{dc} = 11\text{V}$ and $V_{ac} = 0.5\text{V}$.

Figure 4.10: Frequency response curves near sub-harmonic resonance near $2\omega_1$. Maximum non-dimensional deflection $W_{\max}$ at the center of the microplate against the actuating frequency Ω for a quality factor $Q = 250$.

These neighboring resonances are of interest, for instance, for mass sensing MEMS applications. It is noticed that for very small imperfections the amplitude of the new resonance is very small. By further increasing the imperfection, the amplitudes of both resonances become the same but are smaller than the one with the ideal square plate. This

is because we are reducing width of plate (b) while keeping the length (a) constant, to get imperfections, which in return causes higher stiffness of the microplate and hence lower the amplitude of vibration.

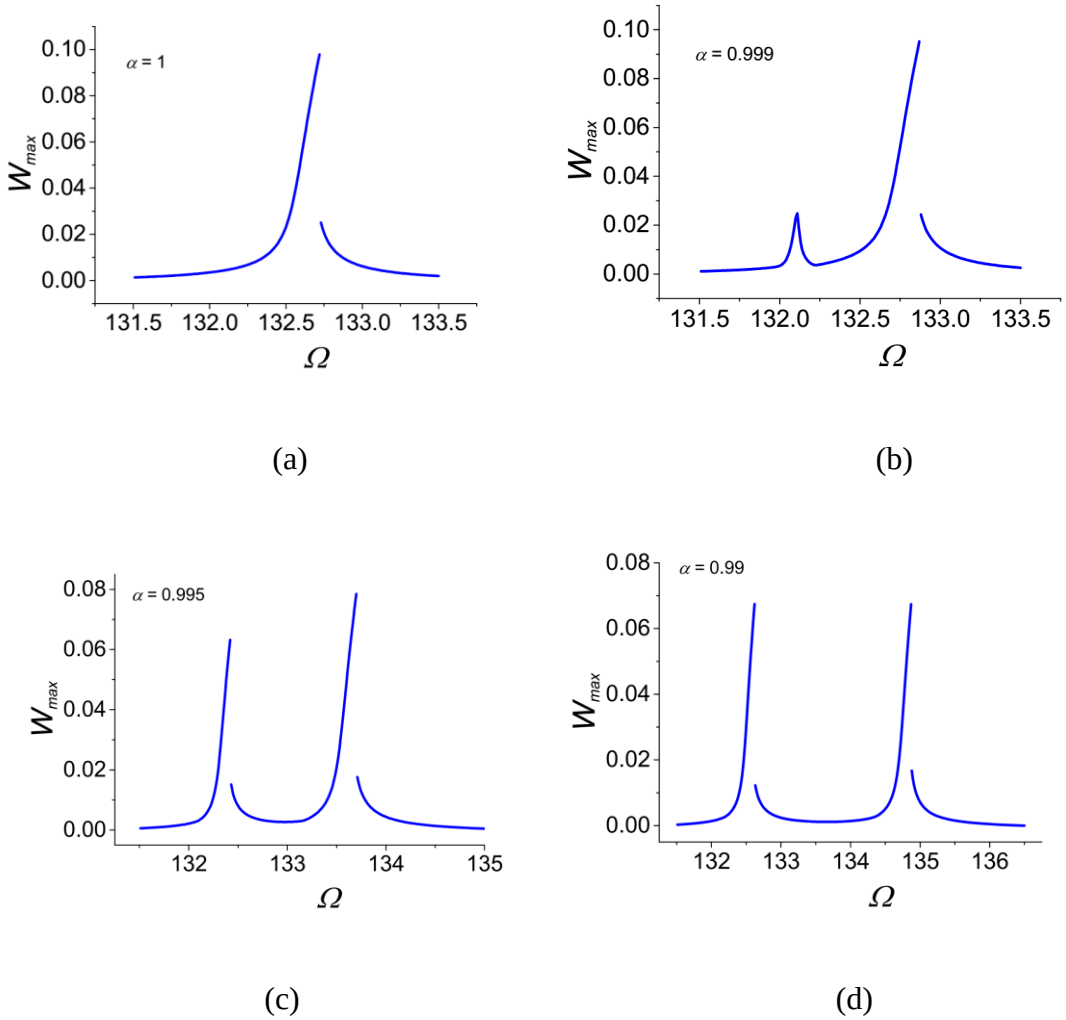

Figure 4.11: Dynamic behavior of an imperfect square plate near the second symmetric-symmetric mode of vibration when actuated at $V_{dc} = 1\text{V}$, $V_{ac} = 0.3\text{V}$ with a quality factor $Q = 1000$.

Chapter 5

Initially Curved Micro-plates under Electrostatic Actuation

In this chapter, we investigate the mechanical behavior of initially curved microplates under electrostatic actuation. It is common for microplates to undergo an initial curvature imperfection, due to the micro fabrication process, which affects significantly their mechanical behavior. Here, we develop a reduced order model based on the Galerkin procedure to simulate the static and dynamic behavior of the microplate. We investigate the convergence of static results with the number of modes retained in the reduced order model. We validate the reduced order model by comparing the calculated static behavior and the fundamental natural frequency with those computed by a finite element model. The static behaviour of the microplate is investigated when applying a DC voltage. Then, the dynamic behaviour of the microplate is examined under the application of a harmonic AC voltage superimposed to a DC voltage. As case studies, we consider two different profiles of the initial curvature imperfection and study their effects on both the static and dynamic responses of the microplates.

5.1. Introduction

MEMS devices are commonly made up of microbeams and microplates [8, 12-24]. These are used in various applications, such as micropumps in micro fluidics, biomedical and cooling applications [15-17, 25-27] , microphones [19-21], mass sensors [22, 23] and resonators [24, 30] to realize sensors and microswitches [31, 32]. These underlying structures undergo imperfections during the micro fabrication process due to residual stresses. To model such structures, accurate models are needed, which properly account for this initial imperfection.

We investigate next the effect of initial curvature profile on the static and dynamic behavior of the plate. Towards this, we consider two commonly encountered profiles of initial curvature and compare their effects on static behavior, eigen frequencies and dynamic behavior. Also we compare the results obtained from reduced order model with the results from a FE model for some cases to validate the model.

5.2. Problem Formulation

In this chapter, we consider a clamped-free-clamped-free (CFCF) rectangular microplate having an initial curvature imperfection $w_0(x, y)$ and in the domain $0 \le x \le a$ and $0 \le y \le b$, as shown in Figure 2.2. The problem was formulated in Chapter 2, where the governing equations (2.49)-(2.51) were derived using the modified von-Karman strains. The associated boundary conditions are given in equations (2.52)-(2.59).

For convenience, we introduce the non-dimensional variables (denoted by hats)

$$\hat{x}=\frac{x}{a}\ ,\ \ \hat{y}=\frac{y}{b}\ ,\ \ \hat{w}=\frac{w}{d}\ ,\ \ \hat{w}_0=\frac{w_0}{d}\ ,\ \ \hat{u}=\frac{au}{d^2}\ ,\ \ \hat{v}=\frac{av}{d^2}\ ,\ \ \ \hat{t}=\frac{t}{T} \tag{5.1}$$

Substituting equation (5.1) into equations (2.49)-(2.51) and dropping the hats, for convenience, we get the following equations:

$$\begin{aligned}&\frac{\partial^2 u}{\partial x^2}+\frac{(1+\upsilon)}{2\alpha}\frac{\partial^2 v}{\partial x\partial y}+\frac{(1-\upsilon)}{2\alpha^2}\frac{\partial^2 u}{\partial y^2}+\left(\frac{\partial w}{\partial x}\frac{\partial^2 w}{\partial x^2}+\frac{\partial w_0}{\partial x}\frac{\partial^2 w}{\partial x^2}+\frac{\partial w}{\partial x}\frac{\partial^2 w_0}{\partial x^2}\right)\\&+\frac{(1+\upsilon)}{2\alpha^2}\left(\frac{\partial w}{\partial y}\frac{\partial^2 w}{\partial x\partial y}+\frac{\partial w_0}{\partial y}\frac{\partial^2 w}{\partial x\partial y}+\frac{\partial w}{\partial y}\frac{\partial^2 w_0}{\partial x\partial y}\right)+\frac{(1-\upsilon)}{2\alpha^2}\left(\frac{\partial w}{\partial x}\frac{\partial^2 w}{\partial y^2}+\frac{\partial w_0}{\partial x}\frac{\partial^2 w}{\partial y^2}+\frac{\partial w}{\partial x}\frac{\partial^2 w_0}{\partial y^2}\right)=0\end{aligned} \tag{5.2}$$

$$\begin{aligned}&\frac{\partial^2 v}{\partial y^2}+\frac{(1+\upsilon)\alpha}{2}\frac{\partial^2 u}{\partial x\partial y}+\frac{(1-\upsilon)\alpha^2}{2}\frac{\partial^2 v}{\partial x^2}+\frac{1}{\alpha}\left(\frac{\partial w}{\partial y}\frac{\partial^2 w}{\partial y^2}+\frac{\partial w_0}{\partial y}\frac{\partial^2 w}{\partial y^2}+\frac{\partial w}{\partial y}\frac{\partial^2 w_0}{\partial y^2}\right)\\&+\frac{(1+\upsilon)\alpha}{2}\left(\frac{\partial w}{\partial x}\frac{\partial^2 w}{\partial x\partial y}+\frac{\partial w_0}{\partial x}\frac{\partial^2 w}{\partial x\partial y}+\frac{\partial w}{\partial x}\frac{\partial^2 w_0}{\partial x\partial y}\right)+\frac{(1-\upsilon)}{2}\left(\frac{\partial w}{\partial y}\frac{\partial^2 w}{\partial x^2}+\frac{\partial w_0}{\partial y}\frac{\partial^2 w}{\partial x^2}+\frac{\partial w}{\partial y}\frac{\partial^2 w_0}{\partial x^2}\right)=0\end{aligned} \tag{5.3}$$

$$\begin{aligned}&\frac{\partial^4 w}{\partial x^4}+\frac{2}{\alpha^2}\frac{\partial^4 w}{\partial x^2\partial y^2}+\frac{1}{\alpha^4}\frac{\partial^4 w}{\partial y^4}+\frac{\partial w}{\partial t^2}+\hat{c}\frac{\partial w}{\partial t}=\alpha_2\frac{V(t)^2}{(1-w)^2}+3\alpha_0^2\left\{\hat{N}_1^i\frac{\partial^2 w}{\partial x^2}+\frac{2}{\alpha}\hat{N}_{12}^i\frac{\partial^2 w}{\partial x\partial y}+\frac{1}{\alpha^2}\hat{N}_2^i\frac{\partial^2 w}{\partial y^2}\right\}\\&+12\alpha_1^2\left\{\frac{\partial u}{\partial x}\left(\frac{\partial^2 w}{\partial x^2}+\frac{\upsilon}{\alpha^2}\frac{\partial^2 w}{\partial y^2}\right)+\frac{1}{\alpha}\frac{\partial v}{\partial y}\left(\upsilon\frac{\partial^2 w}{\partial x^2}+\frac{1}{\alpha^2}\frac{\partial^2 w}{\partial y^2}\right)+(1-\upsilon)\left(\frac{1}{\alpha}\frac{\partial u}{\partial y}+\frac{\partial v}{\partial x}\right)\frac{1}{\alpha}\frac{\partial^2 w}{\partial x\partial y}\right\}\\&+12\alpha_1^2\left\{\begin{aligned}&\frac{1}{2}\left(\frac{\partial w}{\partial x}\right)^2\left(\frac{\partial^2 w}{\partial x^2}+\upsilon\frac{\partial^2 w}{\partial y^2}\right)+\left(\frac{\partial w}{\partial x}\frac{\partial w_0}{\partial x}\right)\left(\frac{\partial^2 w}{\partial x^2}+\upsilon\frac{\partial^2 w}{\partial y^2}\right)\\&+\frac{1}{2\alpha^2}\left(\frac{\partial w}{\partial y}\right)^2\left(\upsilon\frac{\partial^2 w}{\partial x^2}+\frac{1}{\alpha^2}\frac{\partial^2 w}{\partial y^2}\right)+\frac{1}{2\alpha^2}\left(\frac{\partial w}{\partial y}\frac{\partial w_0}{\partial y}\right)\left(\upsilon\frac{\partial^2 w}{\partial x^2}+\frac{1}{\alpha^2}\frac{\partial^2 w}{\partial y^2}\right)\\&+\frac{(1-\upsilon)}{\alpha^2}\left(\frac{\partial w}{\partial x}\frac{\partial w}{\partial y}\frac{\partial^2 w}{\partial x\partial y}+\frac{\partial w_0}{\partial x}\frac{\partial w}{\partial y}\frac{\partial^2 w}{\partial x\partial y}+\frac{\partial w}{\partial x}\frac{\partial w_0}{\partial y}\frac{\partial^2 w}{\partial x\partial y}\right)\end{aligned}\right\}\\&+12\alpha_1^2\left\{\frac{\partial u}{\partial x}\left(\frac{\partial^2 w_0}{\partial x^2}+\frac{\upsilon}{\alpha^2}\frac{\partial^2 w_0}{\partial y^2}\right)+\frac{1}{\alpha}\frac{\partial v}{\partial y}\left(\upsilon\frac{\partial^2 w_0}{\partial x^2}+\frac{1}{\alpha^2}\frac{\partial^2 w_0}{\partial y^2}\right)+(1-\upsilon)\left(\frac{1}{\alpha}\frac{\partial u}{\partial y}+\frac{\partial v}{\partial x}\right)\frac{1}{\alpha}\frac{\partial^2 w_0}{\partial x\partial y}\right\}\\&+12\alpha_1^2\left\{\begin{aligned}&\frac{1}{2}\left(\frac{\partial w}{\partial x}\right)^2\left(\frac{\partial^2 w_0}{\partial x^2}+\upsilon\frac{\partial^2 w_0}{\partial y^2}\right)+\left(\frac{\partial w}{\partial x}\frac{\partial w_0}{\partial x}\right)\left(\frac{\partial^2 w_0}{\partial x^2}+\upsilon\frac{\partial^2 w_0}{\partial y^2}\right)\\&+\frac{1}{2\alpha^2}\left(\frac{\partial w}{\partial y}\right)^2\left(\upsilon\frac{\partial^2 w_0}{\partial x^2}+\frac{1}{\alpha^2}\frac{\partial^2 w_0}{\partial y^2}\right)+\frac{1}{2\alpha^2}\left(\frac{\partial w}{\partial y}\frac{\partial w_0}{\partial y}\right)\left(\upsilon\frac{\partial^2 w_0}{\partial x^2}+\frac{1}{\alpha^2}\frac{\partial^2 w_0}{\partial y^2}\right)\\&+\frac{(1-\upsilon)}{\alpha^2}\left(\frac{\partial w}{\partial x}\frac{\partial w}{\partial y}\frac{\partial^2 w_0}{\partial x\partial y}+\frac{\partial w_0}{\partial x}\frac{\partial w}{\partial y}\frac{\partial^2 w_0}{\partial x\partial y}+\frac{\partial w}{\partial x}\frac{\partial w_0}{\partial y}\frac{\partial^2 w_0}{\partial x\partial y}\right)\end{aligned}\right\}\end{aligned} \tag{5.4}$$

The associated boundary conditions for the non-dimensional equations are

Clamped edges at $x=0$ *and* $x=1$

$$u = 0 \tag{5.5}$$

$$v = 0 \tag{5.6}$$

$$w = 0 \tag{5.7}$$

$$\frac{\partial w}{\partial x} = 0 \tag{5.8}$$

Free edges at $y=0$ *and* $y=1$

$$\frac{\partial v}{\partial y} + \alpha\upsilon\frac{\partial u}{\partial x} + \frac{1}{2}\left[\frac{1}{\alpha}\left(\frac{\partial w}{\partial y}\right)^2 + \alpha\upsilon\left(\frac{\partial w}{\partial x}\right)^2\right] = 0 \tag{5.9}$$

$$\frac{\partial u}{\partial y} + \alpha\frac{\partial v}{\partial x} + \frac{\partial w}{\partial x}\frac{\partial w}{\partial y} = 0 \tag{5.10}$$

$$\frac{\partial^2 w}{\partial y^2} + \alpha^2\upsilon\frac{\partial^2 w}{\partial x^2} = 0 \tag{5.11}$$

$$\frac{\partial^3 w}{\partial y^3} + \alpha^2\left(2-\upsilon\right)\frac{\partial^3 w}{\partial y\partial x^2} = 0 \tag{5.12}$$

The parameters appearing in equations (5.2)-(5.12) are

$$\alpha = \frac{b}{a},\ \ \alpha_0 = \frac{a}{h},\ \ \alpha_1 = \frac{d}{h},\ \ \alpha_2 = \frac{6\left(1-\upsilon^2\right)}{E\,h^3 d^3}\varepsilon\,a^4,\ \hat{c} = \frac{\hat{c}a^4}{TD} \text{ and } \hat{N}_j^i = \frac{\left(1-\upsilon^2\right)}{Eh}N_j^i. \tag{5.13}$$

5.3. Reduced Order Model

This approach follows the method outlined in [11, 43, 83] . In this approach, the out-of-plane deflection w is expressed as

$$w = \sum_{i=1}^{m} q_i(t)\phi_i(x,y) \tag{5.14}$$

where $\phi_i(x,y)$ are the out-of-plane mode shapes of the plate and $q_i(t)$ are the corresponding unknown time dependent coefficients. Substituting equation (5.14) into equations (5.2) and (5.3), we obtain the following equations:

$$\begin{aligned}&\frac{\partial^2 u}{\partial x^2}+\frac{(1+\upsilon)}{2\alpha}\frac{\partial^2 v}{\partial x\partial y}+\frac{(1-\upsilon)}{2\alpha^2}\frac{\partial^2 u}{\partial y^2}+\sum_{k,l} q_k q_l\left[\left(\frac{\partial\phi_k}{\partial x}\frac{\partial^2\phi_l}{\partial x^2}+\frac{(1+\upsilon)}{2\alpha^2}\frac{\partial\phi_k}{\partial y}\frac{\partial^2\phi_l}{\partial x\partial y}\right)+\frac{(1-\upsilon)}{2\alpha^2}\left(\frac{\partial\phi_k}{\partial x}\frac{\partial^2\phi_l}{\partial y^2}\right)\right]\\&+\sum_k q_k\left[\begin{array}{l}\left\{\left(\frac{\partial w_0}{\partial x}\frac{\partial^2\phi_k}{\partial x^2}+\frac{(1+\upsilon)}{2\alpha^2}\frac{\partial w_0}{\partial y}\frac{\partial^2\phi_k}{\partial x\partial y}\right)+\frac{(1-\upsilon)}{2\alpha^2}\left(\frac{\partial w_0}{\partial x}\frac{\partial^2\phi_k}{\partial y^2}\right)\right\}\\+\left\{\left(\frac{\partial\phi_k}{\partial x}\frac{\partial^2 w_0}{\partial x^2}+\frac{(1+\upsilon)}{2\alpha^2}\frac{\partial\phi_k}{\partial y}\frac{\partial^2 w_0}{\partial x\partial y}\right)+\frac{(1-\upsilon)}{2\alpha^2}\left(\frac{\partial\phi_k}{\partial x}\frac{\partial^2 w_0}{\partial y^2}\right)\right\}\end{array}\right]=0\end{aligned} \tag{5.15}$$

$$\begin{aligned}&\frac{\partial^2 v}{\partial y^2}+\frac{(1+\upsilon)\alpha}{2}\frac{\partial^2 u}{\partial x\partial y}+\frac{(1-\upsilon)\alpha^2}{2}\frac{\partial^2 v}{\partial x^2}+\sum_{k,l} q_k q_l\left[\left(\frac{1}{\alpha}\frac{\partial\phi_k}{\partial y}\frac{\partial^2\phi_l}{\partial y^2}+\frac{(1+\upsilon)\alpha}{2}\frac{\partial\phi_k}{\partial x}\frac{\partial^2\phi_l}{\partial x\partial y}\right)+\frac{(1-\upsilon)}{2}\left(\frac{\partial\phi_k}{\partial y}\frac{\partial^2\phi_l}{\partial x^2}\right)\right]\\&+\sum_k q_k\left[\begin{array}{l}\left\{\left(\frac{1}{\alpha}\frac{\partial w_0}{\partial y}\frac{\partial^2\phi_k}{\partial y^2}+\frac{(1+\upsilon)\alpha}{2}\frac{\partial w_0}{\partial x}\frac{\partial^2\phi_k}{\partial x\partial y}\right)+\frac{(1-\upsilon)}{2}\left(\frac{\partial w_0}{\partial y}\frac{\partial^2\phi_k}{\partial x^2}\right)\right\}\\+\left\{\left(\frac{1}{\alpha}\frac{\partial\phi_k}{\partial y}\frac{\partial^2 w_0}{\partial y^2}+\frac{(1+\upsilon)\alpha}{2}\frac{\partial\phi_k}{\partial x}\frac{\partial^2 w_0}{\partial x\partial y}\right)+\frac{(1-\upsilon)}{2}\left(\frac{\partial\phi_k}{\partial y}\frac{\partial^2 w_0}{\partial x^2}\right)\right\}\end{array}\right]=0\end{aligned} \tag{5.16}$$

Equations (5.15) and (5.16) are nonhomogeneous coupled linear PDEs in u and v . Since these equations are linear, the principle of superposition can be used to determine the solution for u and v in the form [83]

$$u = \sum_{k,l} q_k q_l u^{kl} + \sum_{k} q_k u^{k} \tag{5.17}$$

$$v = \sum_{k,l} q_k q_l v^{kl} + \sum_{k} q_k v^{k} \tag{5.18}$$

where the superscript kl denotes the in-plane displacements u^{kl} and v^{kl} caused by the loads f_x^{kl} and f_y^{kl} defined as

$$f_x^{kl} = \left(\frac{\partial \phi_k}{\partial x} \frac{\partial^2 \phi_l}{\partial x^2} + \frac{(1+\upsilon)}{2\alpha^2} \frac{\partial \phi_k}{\partial y} \frac{\partial^2 \phi_l}{\partial x \partial y} \right) + \frac{(1-\upsilon)}{2\alpha^2} \left(\frac{\partial \phi_k}{\partial x} \frac{\partial^2 \phi_l}{\partial y^2} \right) \tag{5.19}$$

$$f_y^{kl} = \left(\frac{1}{\alpha} \frac{\partial \phi_k}{\partial y} \frac{\partial^2 \phi_l}{\partial y^2} + \frac{(1+\upsilon)\alpha}{2} \frac{\partial \phi_k}{\partial x} \frac{\partial^2 \phi_l}{\partial x \partial y} \right) + \frac{(1-\upsilon)}{2} \left(\frac{\partial \phi_k}{\partial y} \frac{\partial^2 \phi_l}{\partial x^2} \right) \tag{5.20}$$

and similarly superscript k denotes the in-plane displacements u^k and v^k caused by the loads f_x^k and f_y^k defined as

$$f_x^k = \left[\begin{array}{l} \left\{ \left(\frac{\partial w_0}{\partial x} \frac{\partial^2 \phi_k}{\partial x^2} + \frac{(1+\upsilon)}{2\alpha^2} \frac{\partial w_0}{\partial y} \frac{\partial^2 \phi_k}{\partial x \partial y} \right) + \frac{(1-\upsilon)}{2\alpha^2} \left(\frac{\partial w_0}{\partial x} \frac{\partial^2 \phi_k}{\partial y^2} \right) \right\} \\ + \left\{ \left(\frac{\partial \phi_k}{\partial x} \frac{\partial^2 w_0}{\partial x^2} + \frac{(1+\upsilon)}{2\alpha^2} \frac{\partial \phi_k}{\partial y} \frac{\partial^2 w_0}{\partial x \partial y} \right) + \frac{(1-\upsilon)}{2\alpha^2} \left(\frac{\partial \phi_k}{\partial x} \frac{\partial^2 w_0}{\partial y^2} \right) \right\} \end{array} \right] \tag{5.21}$$

$$f_y^k = \left[\begin{array}{l} \left\{ \left(\frac{1}{\alpha} \frac{\partial w_0}{\partial y} \frac{\partial^2 \phi_k}{\partial y^2} + \frac{(1+\upsilon)\alpha}{2} \frac{\partial w_0}{\partial x} \frac{\partial^2 \phi_k}{\partial x \partial y} \right) + \frac{(1-\upsilon)}{2} \left(\frac{\partial w_0}{\partial y} \frac{\partial^2 \phi_k}{\partial x^2} \right) \right\} \\ + \left\{ \left(\frac{1}{\alpha} \frac{\partial \phi_k}{\partial y} \frac{\partial^2 w_0}{\partial y^2} + \frac{(1+\upsilon)\alpha}{2} \frac{\partial \phi_k}{\partial x} \frac{\partial^2 w_0}{\partial x \partial y} \right) + \frac{(1-\upsilon)}{2} \left(\frac{\partial \phi_k}{\partial y} \frac{\partial^2 w_0}{\partial x^2} \right) \right\} \end{array} \right] \tag{5.22}$$

Equation (5.4) is multiplied by $(1-w)^2$ to treat the electric force term exactly with no approximation. Now by substituting equations (5.14), (5.17) and (5.18) into equation (5.4), multiplying by $\phi_i(x, y)$ and integrating over the plate domain we get the reduced order model for the governing equations. The reduced order model consists of a system of nonlinear coupled ODEs in $q_i(t)$. This system of ODEs is solved for $q_i(t)$ numerically using the Runge Kutta method and is substituted back into equation (5.14), (5.17), and (5.18) to obtain w, u, and v respectively.

5.4. Results

In the following, we study the effect of the initial curvature on the static and dynamic behavior. The effect of initial curvature on fundamental natural frequency is also investigated. Toward this, we consider two profiles of initial curvature commonly encountered in micro fabricated structures:

$$w_{01} = w_{0\max}\left\{1-Cos^2(\pi x)\right\} \tag{5.23}$$

$$w_{02} = w_{0\max}\left[\left\{1-Cos^2(\pi x)\right\} Sin(\pi \mathrm{y})\right] \tag{5.24}$$

where $w_{0\max}$ is the maximum curvature at the center of the microplate. Profile w_{01} assumes variation in shape along the *x* axis only (cylindrical bending shape) while profile w_{02} assumes variation in shape along both *x* and *y* axis.

5.4.1. Static Results

First, we investigate the convergence of the static solution with the number of transversal modes of vibration retained in the reduced order model. We assume that no in-plane external forces are applied to the microplate, i.e., $\hat{N}_1^i = \hat{N}_{12}^i = \hat{N}_2^i = 0$. To calculate the static deflection of the microplate under a DC load, the time derivatives are dropped in the reduced order model, $V(\mathrm{t})$ is replaced with V_{dc}, and the time dependent unknown coefficients $q_i(t)$ are replaced with constant coefficients q_i. This results in a system of nonlinear algebraic equations, which is numerically solved for q_i. Then equation (5.14) is used to find the non-dimensional transversal deflection. The static response is calculated using various values of voltage parameter $\alpha_2 V_{dc}{}^2$ until the pull-in instability (which occurs when the electrostatic force overcomes the mechanical force from the structure [7]). Figure 5.1 shows the stable branch of the static response at the centre of the microplate against voltage until pull-in.

One can note that the deflection curve is limited by the pull-in instability, where the slope of the curve approaches infinity. As noted, three modes are sufficient to get a reasonably accurate solution. The convergence study is based on non-dimensional parameters, and hence is not specific to any plate of a particular geometry or material.

Next, we investigate the effect of the initial curvature profiles on the static response of the microplate. The length and width of the microplate are $a = 250\mu m$ and $b = 125\mu m$, respectively. The thickness of the microplate is $h = 1.75\mu m$ and the capacitor gap is $d = 2.5\mu m$. The material parameters used in this investigation are $E = 160\mathrm{GPa}$, $\nu = 0.25$

and $\rho = 2500\text{Kg/m}^3$. The static response is calculated using various values of DC voltage V_{dc} until the pull-in for various values of initial curvature imperfections. Figure 5.2 shows the variation of pull-in voltage threshold $V_{dc-pull}$ with the initial imperfection $w_{0\max}$ for the considered profiles w_{01} and w_{02}.

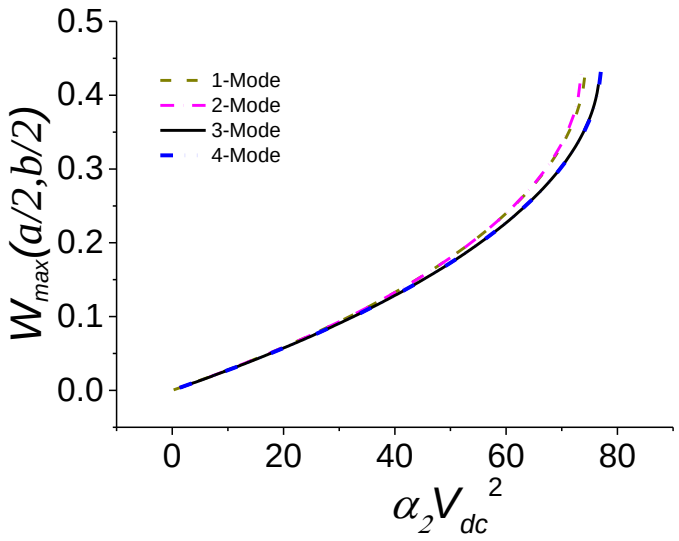

Figure 5.1: Convergence of the static response with the number of transverse modes retained in the reduced order model. Variation of the maximum non-dimensional deflection $W_{\max}$ at the center of the plate with the electrostatic voltage parameter $\alpha_2 V_{dc}^{\ 2}$ when $\alpha = 1$ and $\alpha_1 = 1$.

For validation purpose, similar results calculated by a finite element (FE) model implemented in COMSOL Multiphysics [82] are also shown for profile w_{01}. The Electromechanics module of COMSOL was used to model the electrically actuated microplate. A mapped mesh with 50 elements along the length and 25 along the width of the microplate was used. The geometric and material parameters used for the FE model

are the same as mentioned in this section. Since this is a geometrically nonlinear problem, the geometric nonlinearity is activated before performing the analysis. The results calculated by the reduced order model show good agreement, particularly for small values of imperfection. As the initial imperfection increases, the reduced order model results show deviation from the FE model results. This can be attributed to the use of mode shapes of a linear flat plate as basis functions in the reduced order model. To improve the accuracy for large curvatures, one may need to use mode shapes of a similarly curved plate or some other adequate basis functions.

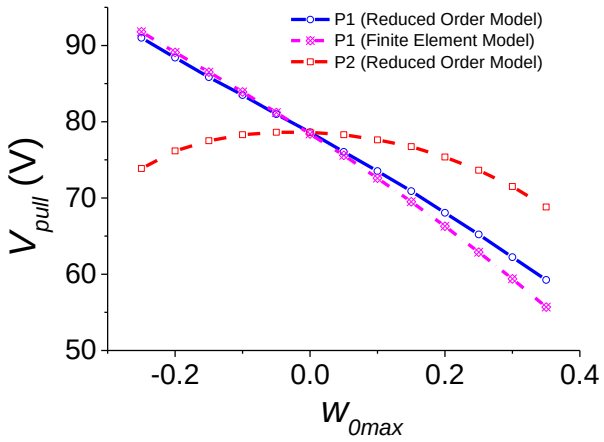

Figure 5.2: Variation of the DC voltage V_{pull} at pull-in with the initial imperfection calculated by the reduced order model for curvature profiles w_{01} and w_{02}. Results calculated by the FE model are also compared with the results of the reduced order model for profile w_{01}.

One can note that although both profiles affect the pull-in voltage, w_{01} shows a significantly large influence as compared to the effect of w_{02}. Moreover for profile w_{02},

the pull-in voltage reduces even when it is curved away from the other stationary electrode while for w_{01} the pull-in voltage varies almost linearly.

5.4.2. Dynamic Results

In this section, first we investigate the effect of the initial curvature profile on the free vibration of the microplate without application of any electrostatic load. Towards this, we drop the nonlinear terms in the reduced order model to solve the linear eigenvalue problem to get the natural frequency. Figure 5.3 shows the variation of non-dimensional natural frequency against the initial curvature $w_{0\max}$. We note that the natural frequency rises significantly with the increase of initial curvature of profile w_{01} but for curvature of profile w_{02}, it only rises slightly and then starts decreasing. It signifies that both profiles have significantly different effect on the natural frequency of the microplate. Lin and Chen [68] and Liu and Yeh [70] have remarked that fundamental natural frequencies are significantly influenced by the initial curvature.

For validation purpose, the natural frequency results calculated by the FE model implemented in COMSOL Multiphysics [82] are also shown for profile w_{01} in Figure 5.3a, which show excellent agreement with the results calculated by the reduced order model, thereby validating the current model.

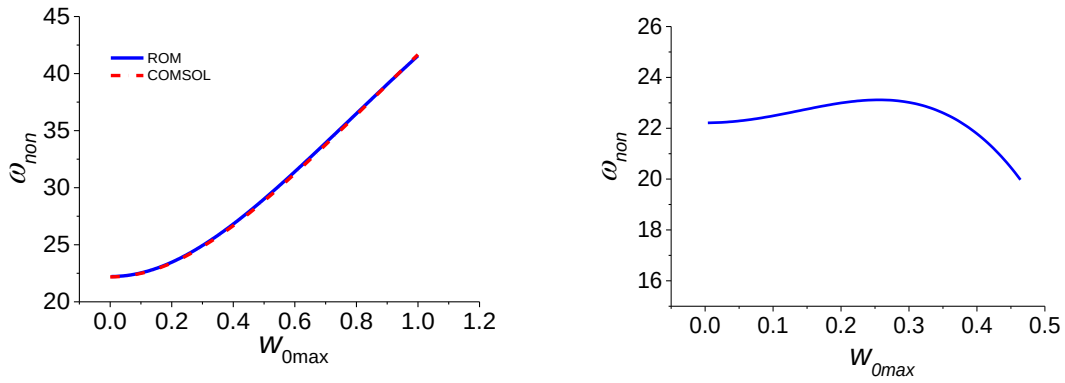

(a) w_{01} (b) w_{02}

Figure 5.3: Variation of the non-dimensional fundamental natural frequency $\omega_{non} = \omega a^2 \sqrt{\frac{\rho}{D}}$ with the initial imperfection $w_{0\max}$. Results calculated by the FE model are also compared with the results of the reduced order model for profile w_{01}.

Next, we investigate the effect of the initial curvature on the forced dynamic responses of the microplate. The dynamic behavior of the microplate is examined by generating frequency response curves in the neighborhood of the primary resonance under the application of a harmonic AC voltage superimposed to a DC voltage, i.e., $V(\mathrm{t}) = V_{dc} + V_{ac} Sin(\Omega \mathrm{t})$. The Runge Kutta method is used to perform long time numerical integration to solve the system of ODEs. The stable steady-state solution is captured after making sure that the transient response is no longer contributing to the response.

First, we study the effect of the initial curvature on the linear response of the microplate. A small AC voltage $V_{ac} = 1\mathrm{V}$ is superimposed to a small DC voltage $V_{dc} = 1\mathrm{V}$ to capture the linear response. Figure 5.4 shows the frequency response curves of the microplate

with curvature profiles w_{01} and w_{02} for various values of initial curvature $w_{0\max}$. One can note that for the profile w_{01} the resonance frequency increases with increasing the initial curvature and for $w_{0\max} = 0.4$, resonance frequency has increased about 22%. For w_{02}, the resonance frequency rises slightly with the initial curvature but then drops below the resonance of a flat plat.

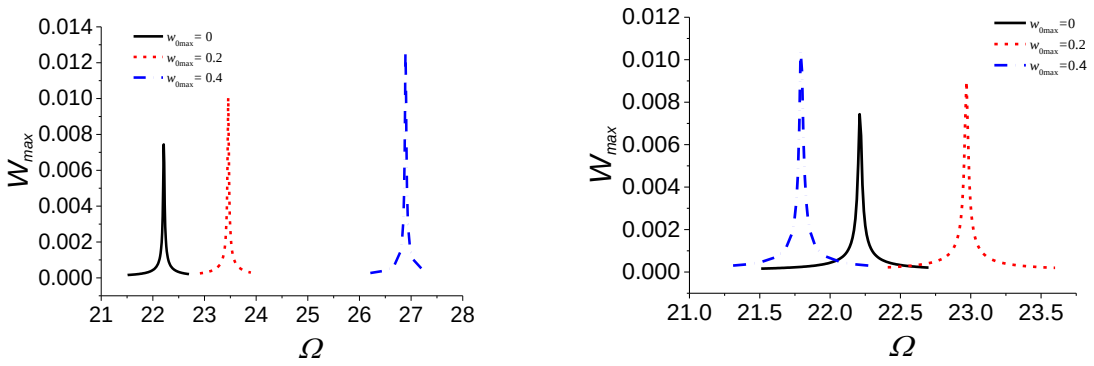

(a) w_{01} (b) w_{02}

Figure 5.4: Frequency response curves showing the linear responses of the microplate for various values of initial curvature imperfection for profile w_{01} and w_{02} when the microplate is actuated by a $V_{ac} = 1\text{V}$ superimposed to a $V_{dc} = 1\text{V}$, and a quality factor $Q = 1000$.

Next, we examine the effect of the initial curvature on the nonlinear large amplitude vibrations of the microplate. To capture the nonlinear large amplitude vibrations, we apply a harmonic AC voltage $V_{ac} = 5\text{V}$ superimposed to a DC voltage $V_{dc} = 5\text{V}$. Figures 5.5 and 5.6 show the frequency response curves for various values of initial curvature imperfection $w_{0\max}$ for profiles w_{01} and w_{02}.

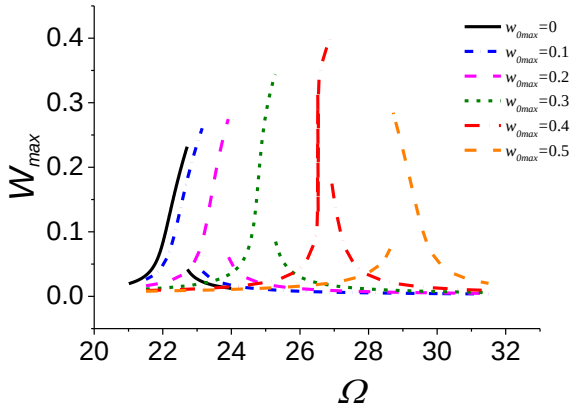

Figure 5.5: Variation of the maximum non-dimensional deflection $W_{\max}$ at the center of the plate with the actuation frequency Ω for various values of initial curvature imperfection for profile w_{01} when $V_{ac} = 5\text{V}$, $V_{dc} = 5\text{V}$, and quality factor $Q = 1000$.

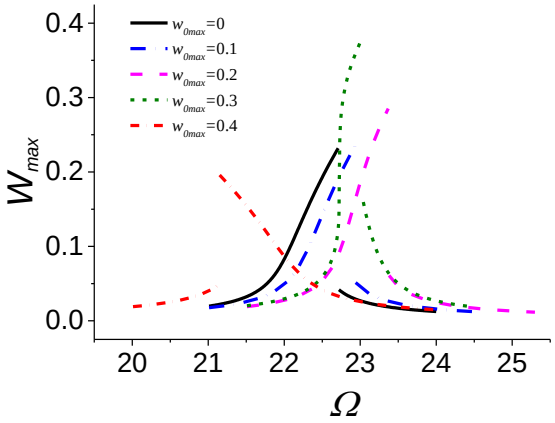

Figure 5.6: Variation of the maximum non-dimensional deflection $W_{\max}$ at the center of the plate with the actuation frequency Ω for various values of initial curvature imperfection for profile w_{02} when $V_{ac} = 5\text{V}$, $V_{dc} = 5\text{V}$, and quality factor $Q = 1000$.

The dynamic response of the flat microplate is a hardening behavior, which is then softened with the increase of initial imperfection for both considered profiles that ultimately converts to softening behavior for certain value of initial imperfection. Similar softening effect due to the initial curvature for completely free plates was reported by Alijani and Amabili [71] for large amplitude vibration. Lin and Chen [68] has also remarked about the conversion of hardening behavior to softening one depending on initial curvature.

We also investigate the transition of hardening behavior of the microplate to the softening behavior with the DC voltage load. We apply a small $V_{ac} = 1\text{V}$ superimposed to V_{dc} and capture the frequency response curves for various values of DC voltage. Figure 5.7 shows that the nonlinear dynamic response of the microplate converts to softening when $V_{dc} = 55\text{V}$ is applied for both profiles at $w_{0\max} = 0.2$.

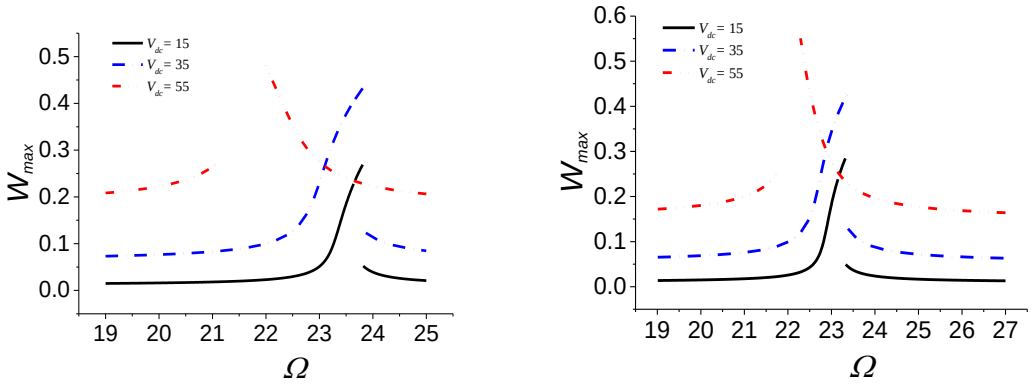

(a) w_{01}, $w_{0\max} = 0.2$ (b) w_{02}, $w_{0\max} = 0.2$

Figure 5.7: Frequency response curves depicting the transition from hardening to softening response of the microplate with increasing V_{dc} with $V_{ac} = 1$.

Chapter 6

Initially Curved Microplates under Electrostatic Actuation: Experimental Case Study and Model Validation

We adopt the dynamic analog of the von-Karman governing equations of imperfect plates to model and simulate the nonlinear mechanical behavior of an initially curved microplate made of silicon nitride. The static behaviour of the microplate is investigated when applying a DC voltage, V_{dc}. Then, the dynamic behaviour of the microplate is examined under the application of a harmonic AC voltage, V_{ac}, superimposed to V_{dc}. Simulation results show good agreement with the experimentally measured responses.

6.1. Introduction

In this chapter we investigate the nonlinear mechanical behavior of an initially deflected CFCF microplate experimentally. Such microplates are fabricated with the same procedure as in clamped-clamped microbeams. However, they offer the advantage of bigger surface area, for instance, which is of an advantage for surface functionalization in mass sensing applications. Also they offer larger flow rates in micropumping applications.

A silicon nitride microplate is fabricated using the micro-fabrication process detailed in [92]. The fabrication has been done by Dr. Mohammed L. Bellaredj at the KAUST Advanced Nano Fabrication (ANIC) laboratory. These microplates have acquired initial curvature during fabrication process due to residual stresses. These have been tested in collaboration with Dr. M. L. Bellaredj and Dr. A. Ramini. Both the static and dynamic analysis are performed and results are compared with the simulation results for the model validation purpose.

6.2. Experiment

First, we used optical interferometry profiler to characterize the dimensions and geometry of the microplate without any electrostatic load. We found that the microplate has an initial deflection due to residual stresses caused by the micro fabrication process (Figure 6.1). The maximum initial deflection w_0 at the center of the microplate is recorded to be $w_{0\max} = 0.47\mu m$. The length and width of the microplate are $a = 250\mu m$ and $b = 125\mu m$, respectively. The thickness of the microplate is $h = 1.75\mu m$ and the gap d is found to be $d = 2.25\mu m$.

Since the silicon nitride (Si_3N_4) is a dielectric material with a dielectric constant $\varepsilon_{rSiNx} = 7$, a conductive layer of gold is applied on top of the microplate. The equivalent capacitor gap is thus the air gap plus the contribution from the silicon nitride microplate. Equivalent capacitor gap d_{eq} for the parallel plate capacitor is calculated by using the formula $d_{eq} = d + \frac{t_{SiNx}}{\varepsilon_{rSiNx}}$ [93] and is found to be $d_{eq} = 2.464\mu m$.

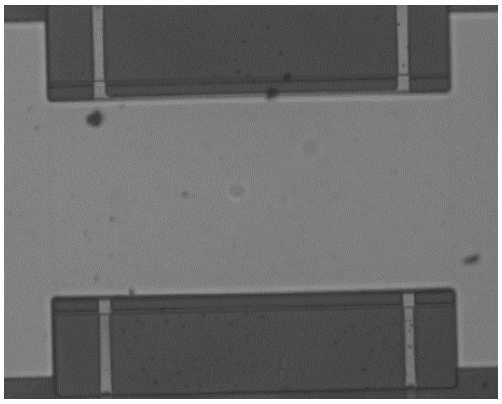

(a)

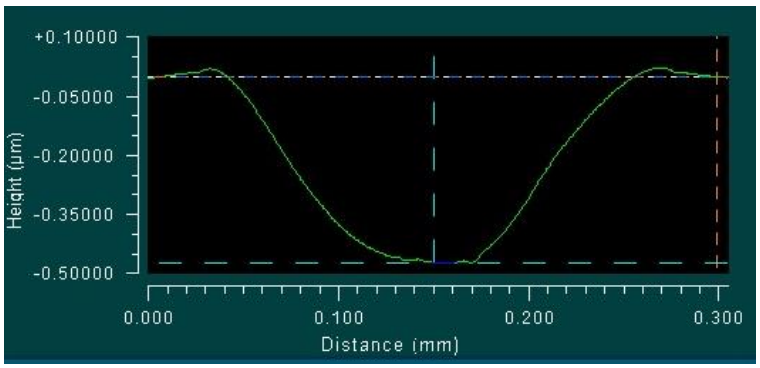

(b)

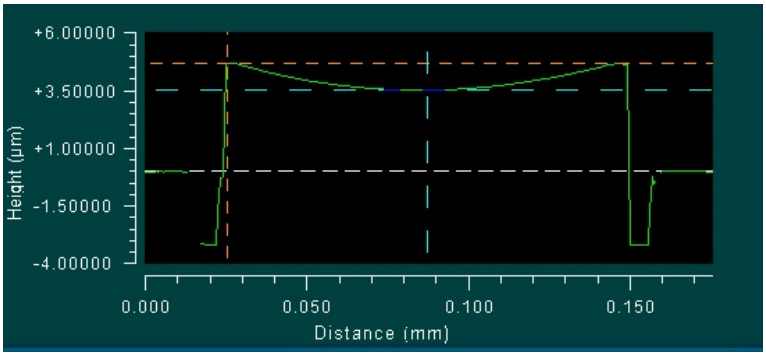

(c)

Figure 6.1: (a) Optical microscope view of the fabricated microplate, (b) deflection profile along the length of the microplate, and (c) deflection profile along the width of the microplate.

Figure 6.2 shows the used experimental setup. It consists of a Micro System Analyzer [94] which is a laser Doppler vibrometer, a vacuum chamber; which houses the microplate, a vacuum pump to reduce the pressure, and a data acquisition system DAQ.

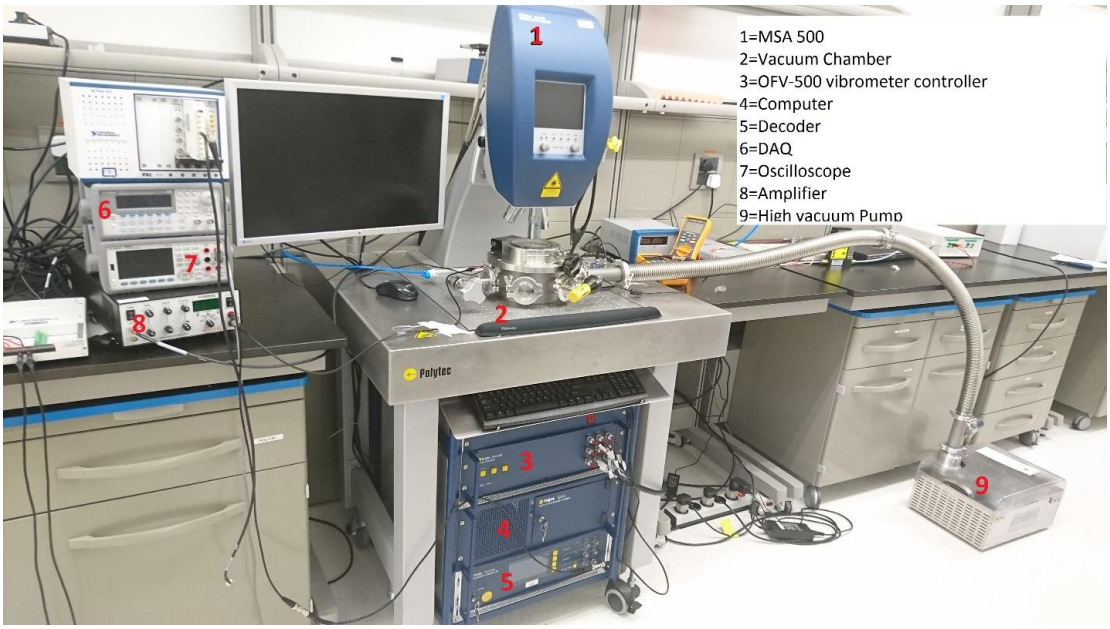

Figure 6.2: Experimental setup showing the Micro-System Analyzer MSA-500, a vacuum chamber, a vacuum pump and data acquisition system DAQ.

To measure the static response of the plate under electrostatic loads, we apply a DC load V_{dc} and capture the deflection at the center of the microplate using also the optical interferometry profiler. Figure 6.3 shows the maximum deflections $W_{\max}$ measured at the center of the microplate against V_{dc} until the plate pulls onto the stationary electrode. The measured pull-in voltage V_{pull} is found near 75V.

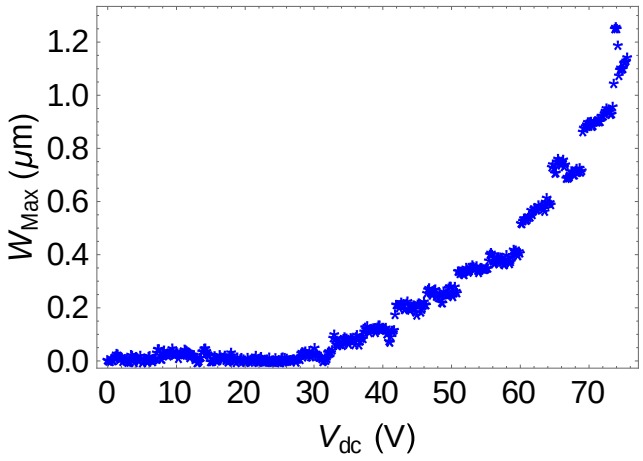

Figure 6.3: The maximum deflection $W_{\max}$ measured at the center of the microplate against V_{dc} until pull-in, at a 3.3 mTorr chamber pressure.

To investigate the dynamic response, first we actuated the microplate by applying a white noise signal to identify the linear resonance frequencies. Figure 6.4 shows the velocity responses of the microplate to a white noise signal. The figure shows a primary resonance somewhere near 250 kHz along with some higher mode resonances.

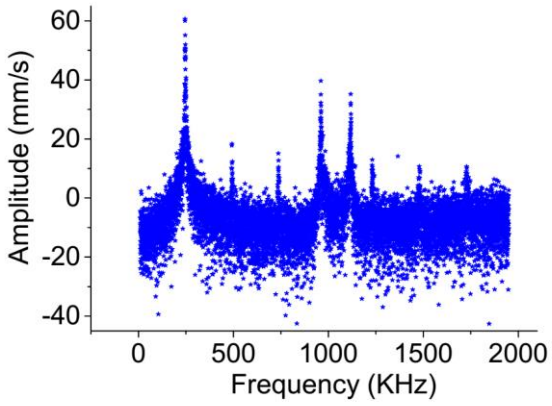

Figure 6.4: The velocity response of the microplate to the white noise actuation signal at V_{dc}=5V, V_{ac}=10V and 3.3 mTorr chamber pressure.

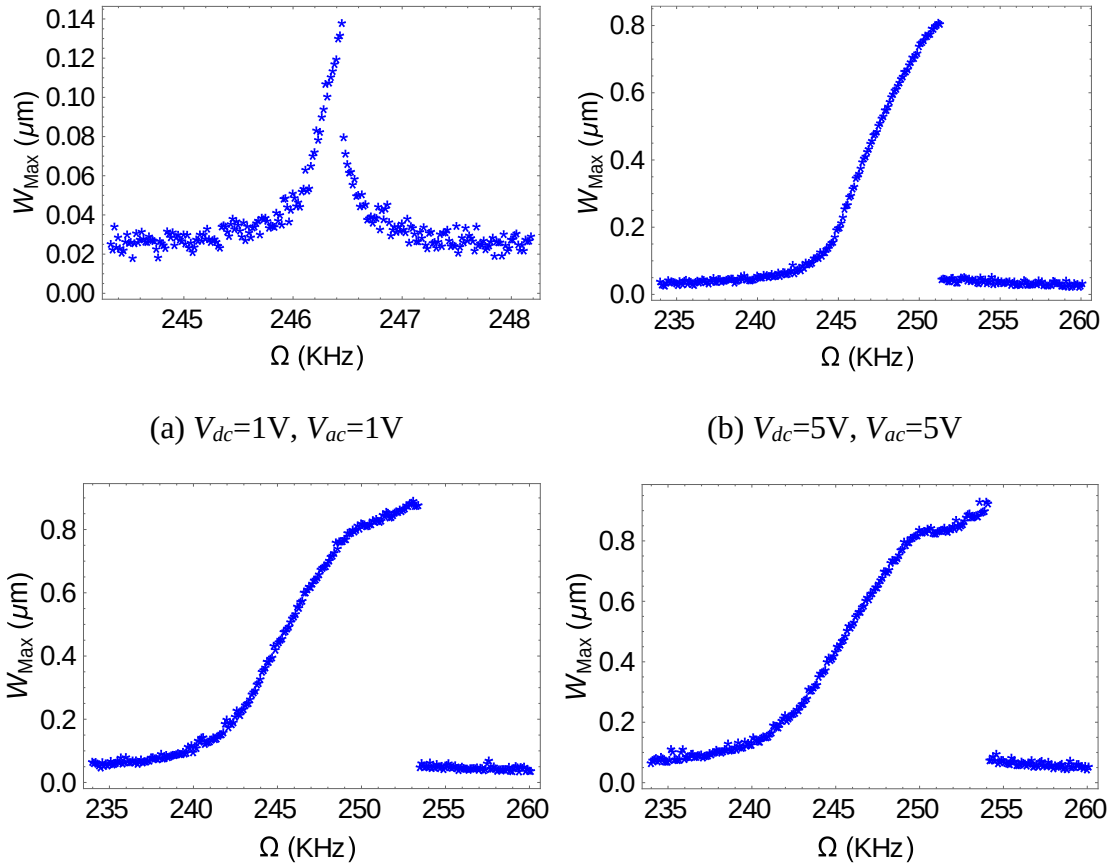

(a) V_{dc}=1V, V_{ac}=1V

(b) V_{dc}=5V, V_{ac}=5V

(c) V_{dc}=10V, V_{ac}=5V

(d) V_{dc}=15V, V_{ac}=5V

Figure 6.5: Frequency response plots in the neighborhood of the fundamental natural frequency of the microplate at various combinations of applied loads at a 3.3 mTorr chamber pressure.

Next, to find the forced response, a harmonic load of amplitude V_{ac} superimposed to V_{dc} was applied to the microplate, i.e., $V(\mathrm{t}) = V_{dc} + V_{ac} Sin(\Omega \mathrm{t})$. We performed frequency sweeps in the neighborhood of the fundamental natural frequency at various applied voltages. First we applied small voltages to capture the linear response. We could capture a nearly linear response at $V_{ac} = 1\mathrm{V}$ and $V_{ac} = 1\mathrm{V}$ (Figure 6.5a). The fundamental natural frequency of the microplate f is found to be around 246.3 KHz. Afterwards nonlinear

responses at various higher voltages were captured (Figure 6.5b-c). The microplate shows the nonlinear hardening response due to midplane stretching. Nevertheless the hardening response has been weakened due to the initial imperfection. This weakening effect will be further explained in the next section when we compare the theoretical results of a flat plate with the experimental results of the initially deflected microplate. Figure 6.5d shows a strange behavior near $\Omega = 250\text{KHz}$, where the maximum deflection seems to be reduced slightly. This can be because of the laser beam getting somewhat away from the center of the microplate and hence recording a lower deflection.

6.3. Theory

In this section we present the theoretical static and dynamic results calculated by reduced order model of Chapter 5 and compare with the experimentally measured data for model validation. We use the plate parameters found by experiment along with the material parameters $E = 160\text{GPa}$, $\nu = 0.25$ and $\rho = 2500\text{Kg/m}^3$. The initial imperfection profile of the microplate is approximated by the function $w_0 = \chi\left[\left\{1 - Cos^4(\pi x)\right\} Sin(\pi\, \text{y})\right]$, where χ is the parameter that controls the maximum initial deflection at the center of the microplate. Figure 6.6 shows plots of the assumed profile of initial curvature imperfection along the length and the width of the plate respectively.

To calculate the static deflection of the microplate under a DC load, we drop the time derivatives in the reduced order model; and the time dependent unknown coefficients $q_i(t)$ are replaced with constant coefficients q_i, and $V(\text{t})$ is replaced with V_{dc}. This

results in a system of nonlinear algebraic equations, which is numerically solved for q_i. Then equation (5.14) is used to find the transversal deflection.

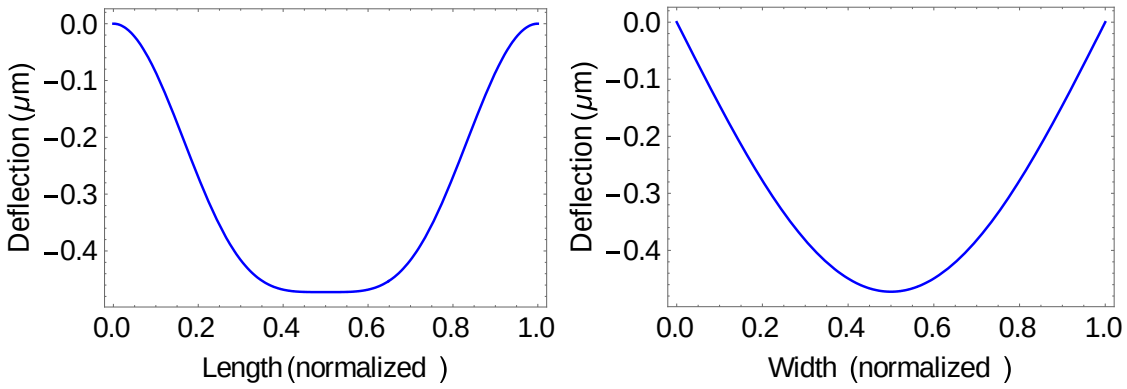

(a) (b)

Figure 6.6: Plots of the assumed profile passing through the center of the microplate, (a) along the length of the microplate, (b) along the width of the microplate.

The static response is calculated using various values of DC voltage V_{dc} until the pull-in. The results are compared with the static responses measured experimentally in Figure 6.7. The results show excellent agreement with the experimentally measured data thus validating the reduced order model.

The dynamic response of the microplate is calculated by applying a V_{ac} superimposed to V_{dc}, i.e., $V(\mathrm{t}) = V_{dc} + V_{ac} Sin(\Omega \mathrm{t})$. The quality factor Q is approximated from the experimental frequency response at $V_{ac} = 1\mathrm{V}$ and $V_{dc} = 1\mathrm{V}$ (Figure 6.5a) and is found to be around 785. This value is used in the simulations.

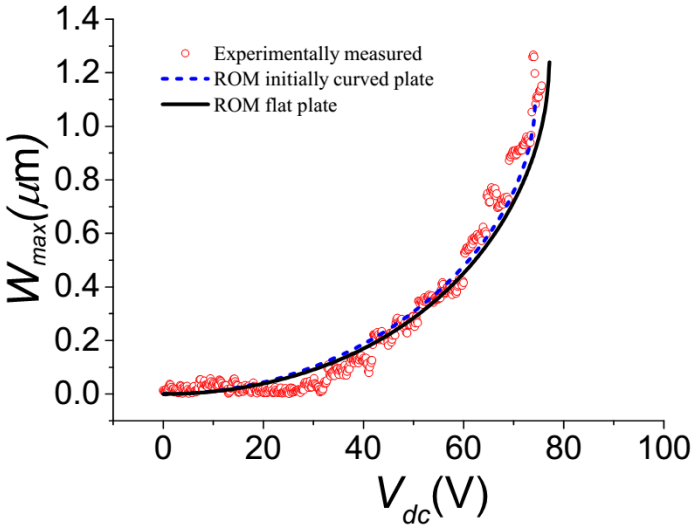

Figure 6.7: The maximum deflection $W_{\max}$ at the center of the microplate against V_{dc} until the pull-in; calculated by the reduced order model accounting for initial curvature and measured experimentally. Results calculated by reduced order model for the flat plat are also shown for comparison.

An in-plane tensile force $N_{xx} = 0.7\text{N/m}$ was applied to match the experimentally measured fundamental natural frequency. The initial imperfection parameter χ is set such that the maximum initial imperfection at the center of the microplate is $w_{0\max} = 0.4718\mu m$. Figure 6.8 shows the comparison of the dynamic responses calculated by the reduced order model with the experimentally measured results in the neighborhood of the fundamental natural frequency at various combinations of applied voltages. We note the results calculated by reduced order model show good agreement with the experimentally measured response.

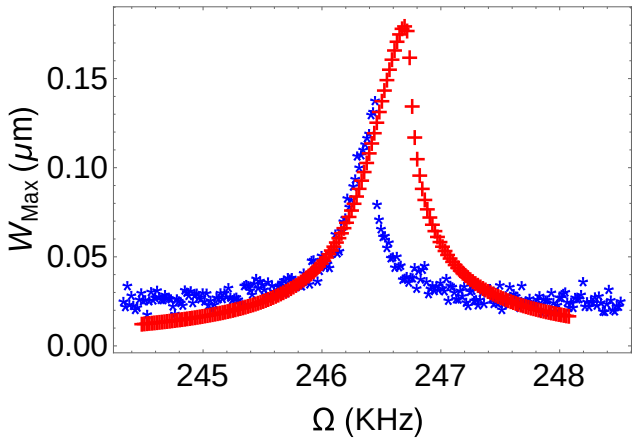

(a) V_{dc}=1V, V_{ac}=1V

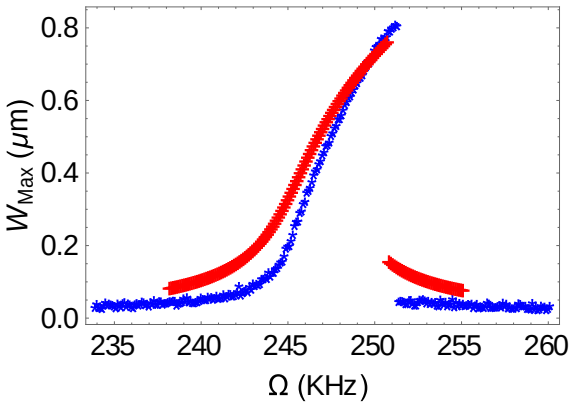

(b) V_{dc}=5V, V_{ac}=5V

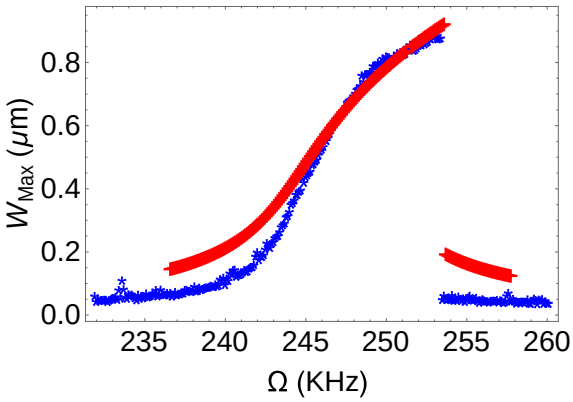

(c) V_{dc}=10V, V_{ac}=5V

Figure 6.8: Comparison of the dynamic responses in the neighborhood of the fundamental natural frequency, calculated by the reduced order model '+' with the experimentally measured results '*' at various combinations of applied voltages.

Next, we compare the dynamic response of a flat plate with the experimentally measured response of the initially deflected microplate. Towards this we set the initial imperfection $w_0 = 0$, and capture the frequency response curve near the fundamental natural frequency. Figure 6.9 shows that the flat plate exhibits stronger hardening nonlinear response as compared to the experimentally measured response of the

fabricated microplate. Figure 6.9 reveals that the reduced order model without taking into account the effects of initial imperfection produces erroneous results. This is because the initial imperfection introduces softening effects due to the quadratic nonlinearity, which weakens the hardening behavior. Similar softening effect due to initial curvature imperfection was also captured experimentally by Alijani and Amabili [71] for completely free rectangular plates for large amplitude vibrations. Lin and Chen [68] remarked that large amplitude behavior may change drastically from hardening to softening depending on initial imperfection. Ostiguy et al. [69] stated that a plate with initial imperfection may exhibit a soft spring behavior.

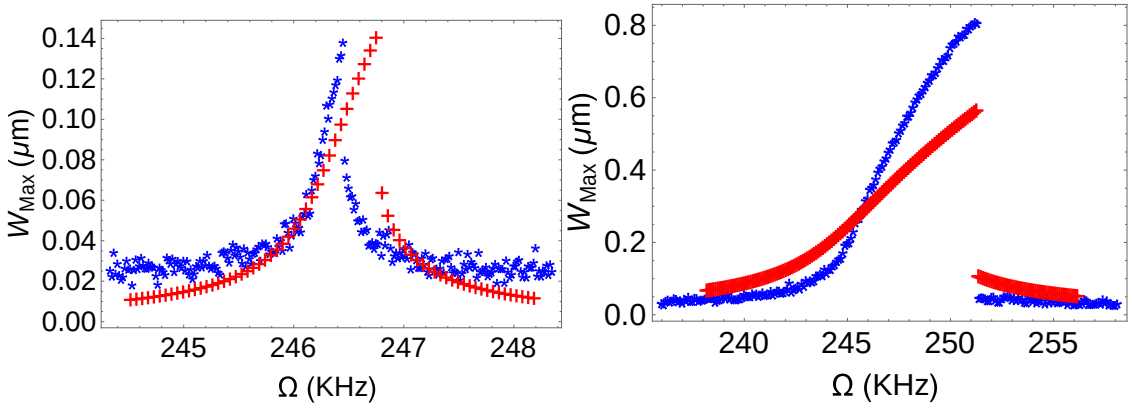

(a) V_{dc}=1V, V_{ac}=1V (b) V_{dc}=5V, V_{ac}=5V

Figure 6.9: Comparison of the simulated dynamic response of a flat microplate '+' with the experimentally measured response of the microplate '*', which has initial curvature imperfection.

Chapter 7

Summary, Conclusions, and Future Work

In this chapter we summarize the dissertation and present the main conclusions and recommendations for the future works.

7.1. Summary and Conclusions

7.1.1. Approaches for Reduced Order Modeling of Electrically Actuated von-Karman Microplates

We presented various approaches to develop a reduced order model for the nonlinear von-Karman microplates actuated electrically to study the static and dynamic behavior. We used different types of basis functions in conjunction with the Galerkin method to discretize the governing equations.

First the convergence of static response was investigated with the number of modes used in the ROM for the different approaches. Then for validation purpose we compared the static response calculated by the models under investigation with the results calculated by FE model implemented in COMSOL. The comparison has indicated that all the models show an excellent agreement with the FE model results except model III, which was shown to represent poorly the cubic nonlinearity due to midplane stretching due to the used shape functions. Eigen frequency analysis was performed using the approaches

presented in the models II-V, in conjunction with linearized equations for initially deflected microplate under DC load V_{dc} .

Eigen frequency results calculated by the current models are compared with the FE results, which show an excellent agreement except model III. This agrees with the static results and confirms the remark that model III does not account accurately for the cubic nonlinearity and that the shape functions used to represent the in-plane displacements are not accurate enough to capture the full effect of midplane stretching.

Next we compared the dynamic response through frequency response curves at a small and large harmonic exciting force for the models II-V, since model I is not suitable for dynamic studies due to its iterative nature it's excluded from the dynamic analysis. We noted that for linear vibrations analysis all the models show an excellent agreement except model II, which show a slight difference from the other models. For the large nonlinear vibrations, model III deviate from the other models, which was also the case in the static and Eigen frequency analysis and ratifies the remark that model III does not account accurately for the cubic nonlinearity. Models II, IV and V show very good agreement at large amplitude vibrations.

As a conclusion, although it sounds appropriate to use any of them for investigation of large amplitude vibrations of microplates, we believe that model V is the most accurate one since it calculates the exact solution for midplane stretching while for all the other models we approximate the in-plane displacements using some kind of shape functions. Moreover it can be used with confidence for microplates with other boundary conditions for example a clamped-free-clamped-free (CFCF) microplate. For such a case the other

models may not be used with the same shape functions. So we conclude that model V is more rigorous and versatile and can be used for a microplate with any kind of boundary condition.

7.1.2. An Investigation of the Static and Dynamic Behavior of Electrically Actuated Rectangular Microplates

We used a reduced order model for the investigation of the static as well as the dynamic behavior of electrically actuated rectangular microplates. First convergence of the static results with the number of mode shapes retained in the ROM was studied. We found that four modes are sufficient for convergence. We investigated the effect of different non-dimensional parameters on the static behavior. Increasing the plate aspect ratio α decreases the voltage parameter at pull-in while increasing the gap to thickness ratio α_1 increases the voltage parameter.

The dynamic behavior of the microplate was investigated near primary and super-harmonic resonances using long time numerical integration. We captured the stable solutions using forward and backward frequency sweeps. The microplate actuated near primary resonance shows a strong hardening behavior due to the cubic nonlinearity, which comes into play due to midplane stretching. Increasing V_{ac} further widens the gap between the two stable solutions captured by forward and backward frequency sweeps and pull-in instability occurs at a lower vibration amplitude. Interesting phenomena are revealed when the microplate is actuated at $\frac{\omega_1}{3}$ super-harmonic. We found when increasing the applied DC load that there is a transition from hardening behavior to

softening behavior. We also investigated the response of imperfect square microplates at the second symmetric-symmetric mode. Breaking the geometrical symmetry by slightly varying the value of α results in distinct neighboring resonances, which can be employed for developing mass sensing MEMS devices.

7.1.3. Initially Curved Micro-plates under Electrostatic Actuation

We presented a reduced order model based on the Galerkin procedure for initially curved rectangular plates under electrostatic actuation to simulate the static and dynamic behavior. First, we performed a convergence study for the reduced order model and found that three transversal modes retained in the model produce sufficiently accurate results. Then, we investigated the effect of the curvature profile on the static behavior of the microplate. We found that the considered profiles have significantly different effects on the static behavior. For validation purpose, we compared the static results calculated by reduced order model with the similar results calculated by a FE model and found a good agreement.

Next, we investigated the free and forced dynamic responses of the microplate. We found that the considered profiles have considerably different effects on the natural frequency of the microplate. We also compared the natural frequency results calculated by the model with the similar results obtained by a FE model implemented in COMSOL Multiphysics, which show an excellent agreement thus validating the model.

Then, we investigated the effect of the curvature profile on the forced dynamic behavior of the microplate. Large amplitude vibrations seem to show similar behavior, for which

the microplate shows a transition from hardening to softening at certain value of initial curvature for both profiles. Transition from hardening to softening behavior at a higher DC voltage was noted also in a similar manner for both profiles.

Thus, we conclude that the curvature profile has significant effect on the static and dynamic behavior of the microplate. Eigen frequency may rise significantly or drop depending on the curvature profile. Large amplitude vibration behavior of the microplates converts from hardening to softening depending on the level of initial curvature.

7.1.4. Initially Curved Microplates under Electrostatic Actuation: Experimental Case Study and Model Validation

We presented experimental investigations on initially curved Si_3N_4 microplates to validate the reduced order model. We compared the results obtained by the reduced order model with the experimentally measured data. The comparison showed excellent agreement. Thus we conclude that the reduced order model based on the governing equations presented in Chapter 2, which accounts for the effects of initial curvature imperfection, is an accurate model. On the contrary, it was revealed in Figure 6.9 that the reduced order model without taking into account the effects of initial curvature imperfection produces erroneous results.

7.2. Future Work Directions

The following is a list of recommendations for future work directions.

- The presented investigation of the mechanical behavior of fully clamped rectangular microplates is conducted considering a constant quality factor. The work should be extended to include squeeze film damping effects into the model to simulate the behavior at various air pressure.

- One interesting future research direction would be to extend the present work to model the fluid-structure interaction in micropump applications like drug delivery and manipulation in microfluidics.

- It would be interesting to investigate the mechanics of structure of other geometrical shapes for example circular and semicircular. Also present work, which is limited to electrostatic actuation should be extended to other actuation techniques, e.g., electromagnetic, electrothermal, and piezoelectric.

- Presented models can be tweaked to model the Graphene structures. Graphene is very promising to develop resonators having high quality factors to realize high sensitivity sensing application for example mass/gas sensors.

- The presented reduced order model can be used to implement more sophisticated numerical techniques like shooting to simulate both stable and unstable branches of response and to clearly identify the dynamic pull-in of the microplate.

- The present work can be extended to design new microplate based MEMS devices, such as micropumps and mass/gas sensors.

- Work needs to be extended to model the MEMS devices operating in liquid mediums.

- The present work can be extended to model and simulate the behavior of electrostatically coupled microplates, where both sides of the parallel plate capacitor are flexible plates undergoing deflection when an electrostatic load is applied.

REFERENCES

1. Tsai, N.-C. and C.-Y. Sue, *Review of MEMS-based drug delivery and dosing systems.* Sensors and Actuators A: Physical, 2007. **134**(2): p. 555-564.
2. Nisar, A., N. Afzulpurkar, B. Mahaisavariya, and A. Tuantranont, *MEMS-based micropumps in drug delivery and biomedical applications.* Sensors and Actuators B: Chemical, 2008. **130**(2): p. 917-942.
3. Grayson, A.R., R.S. Shawgo, A.M. Johnson, N.T. Flynn, Y. Li, M.J. Cima, and R. Langer, *A BioMEMS review: MEMS technology for physiologically integrated devices.* Proceedings of the IEEE, 2004. **92**(1): p. 6-21.
4. Chang, S.-C.S., *MEMS in Automobiles*, in *Microsystems and Nanotechnology*. 2012, Springer. p. 721-757.
5. Weinberg, H., *MEMS sensors are driving the automotive industry.* Sensors, 2002. **19**(2): p. 36-41.
6. Varadan, V.K., K.J. Vinoy, and K.A. Jose, *RF MEMS and their applications*. 2003: John Wiley & Sons.
7. Younis, M.I., *MEMS Linear and Nonlinear Statics and Dynamics*. Vol. 20. 2011: Springer.
8. Batra, R.C., M. Porfiri, and D. Spinello, *Review of modeling electrostatically actuated microelectromechanical systems.* Smart Materials and Structures, 2007. **16**(6): p. R23.
9. Tetteh, E.A., M.A. Boatemaa, and E.O. Martinson. *A review of various actuation methods in micropumps for drug delivery appliactions*. in *Electronics, Computer and Computation (ICECCO), 2014 11th International Conference on*. 2014. IEEE.
10. Zhang, W.-M., H. Yan, Z.-K. Peng, and G. Meng, *Electrostatic pull-in instability in MEMS/NEMS: A review.* Sensors and Actuators A: Physical, 2014. **214**: p. 187-218.
11. Younis, M.I., E.M. Abdel-Rahman, and A. Nayfeh, *A reduced-order model for electrically actuated microbeam-based MEMS.* Microelectromechanical Systems, Journal of, 2003. **12**(5): p. 672-680.
12. Ng, T.Y., T.Y. Jiang, H. Li, K.Y. Lam, and J.N. Reddy, *A coupled field study on the non-linear dynamic characteristics of an electrostatic micropump.* Journal of Sound and Vibration, 2004. **273**(4–5): p. 989-1006.
13. Machauf, A., Y. Nemirovsky, and U. Dinnar, *A membrane micropump electrostatically actuated across the working fluid.* Journal of Micromechanics and Microengineering, 2005. **15**(12): p. 2309-2316.
14. Chuang, W.C., H.L. Lee, P.Z. Chang, and Y.C. Hu, *Review on the modeling of electrostatic MEMS.* Sensors, 2010. **10**(6): p. 6149-6171.
15. Zengerle, R., J. Ulrich, S. Kluge, M. Richter, and A. Richter, *A bidirectional silicon micropump.* Sensors and Actuators A: Physical, 1995. **50**(1): p. 81-86.
16. Lintel, H.v., v.d.F. Pol, and S. Bouwstra, *A piezoelectric micropump based on micromachining of silicon.* Sensors and actuators, 1988. **15**(2): p. 153-167.

17. Maillefer, D., H. van Lintel, G. Rey-Mermet, and R. Hirschi. *A high-performance silicon micropump for an implantable drug delivery system*. in *Micro Electro Mechanical Systems, 1999. MEMS'99. Twelfth IEEE International Conference on*. 1999. IEEE.
18. Nguyen, N.-T., X. Huang, and T.K. Chuan, *MEMS-micropumps: a review.* Journal of fluids Engineering, 2002. **124**(2): p. 384-392.
19. Takahashi, H., A. Suzuki, E. Iwase, K. Matsumoto, and I. Shimoyama, *MEMS microphone with a micro Helmholtz resonator.* Journal of Micromechanics and Microengineering, 2012. **22**(8): p. 085019.
20. Je, C.H., J. Lee, W.S. Yang, J. Kim, and Y.-H. Cho, *A surface-micromachined capacitive microphone with improved sensitivity.* Journal of Micromechanics and Microengineering, 2013. **23**(5): p. 055018.
21. Zhou, Z., L. Rufer, E. Salze, P. Yuldashev, S. Ollivier, and M. Wong, *Bulk micro-machined wide-band aero-acoustic microphone and its application to acoustic ranging.* Journal of Micromechanics and Microengineering, 2013. **23**(10): p. 105006.
22. Hu, Z., J. Hedley, N. Keegan, J. Spoors, W. Waugh, B. Gallacher, F.-X. Boillot, J. Collet, and C. McNeil, *Design, fabrication and characterization of a piezoelectric MEMS diaphragm resonator mass sensor.* Journal of Micromechanics and Microengineering, 2013. **23**(12): p. 125019.
23. Suresh, K., G. Uma, and M. Umapathy, *Design of a resonance-based mass sensor using a self-sensing piezoelectric actuator.* Smart Materials and Structures, 2012. **21**(2): p. 025015.
24. Alsaleem, F.M., M.I. Younis, and H.M. Ouakad, *On the nonlinear resonances and dynamic pull-in of electrostatically actuated resonators.* Journal of Micromechanics and Microengineering, 2009. **19**(4): p. 045013.
25. Faris, W.F., E.M. Abdel-Rahman, and A.H. Nayfeh. *Mechanical behavior of an electrostatically actuated micropump*. in *43 rd AIAA/ASME/ASCE/AHS/ASC Structures, Structural Dynamics, and Materials Conference, Denver, CO*. 2002-1303.
26. Amirouche, F., Y. Zhou, and T. Johnson, *Current micropump technologies and their biomedical applications.* Microsystem Technologies, 2009. **15**(5): p. 647-666.
27. Bertarelli, E., R. Ardito, R. Ardito, A. Corigliano, and R. Contro, *A plate model for the evaluation of pull-in instability occurrence in electrostatic micropump diaphragms.* International Journal of Applied Mechanics, 2011. **3**(01): p. 1-19.
28. Tong, P. and W. Huang, *Large Deflection of Thin Plates in Pressure Sensor Applications.* Journal of Applied Mechanics, 2002. **69**(6): p. 785-789.
29. Eaton, W.P. and J.H. Smith, *Micromachined pressure sensors: review and recent developments.* Smart Materials and Structures, 1997. **6**(5): p. 530.
30. Mestrom, R., R. Fey, J. Van Beek, K. Phan, and H. Nijmeijer, *Modelling the dynamics of a MEMS resonator: simulations and experiments.* Sensors and Actuators A: Physical, 2008. **142**(1): p. 306-315.
31. Samaali, H., F. Najar, S. Choura, A.H. Nayfeh, and M. Masmoudi, *A double microbeam MEMS ohmic switch for RF-applications with low actuation voltage.* Nonlinear Dynamics, 2011. **63**(4): p. 719-734.

32. Jia, X.L., J. Yang, and S. Kitipornchai, *Pull-in instability of geometrically nonlinear micro-switches under electrostatic and Casimir forces.* Acta mechanica, 2011. **218**(1-2): p. 161-174.
33. Chao, P.C., C.-W. Chiu, and C. Tsai, *A novel method to predict the pull-in voltage in a closed form for micro-plates actuated by a distributed electrostatic force.* Journal of Micromechanics and Microengineering, 2006. **16**(5): p. 986-998.
34. Nayfeh, A.H. and M.I. Younis, *A new approach to the modeling and simulation of flexible microstructures under the effect of squeeze-film damping.* Journal of Micromechanics and Microengineering, 2004. **14**(2): p. 170-181.
35. Zand, M.M. and M. Ahmadian, *Characterization of coupled-domain multi-layer microplates in pull-in phenomenon, vibrations and dynamics.* International Journal of Mechanical Sciences, 2007. **49**(11): p. 1226-1237.
36. Pursula, A., P. Råback, S. Lähteenmäki, and J. Lahdenperä, *Coupled FEM simulations of accelerometers including nonlinear gas damping with comparison to measurements.* Journal of Micromechanics and Microengineering, 2006. **16**(11): p. 2345-2354.
37. Telukunta, S. and S. Mukherjee, *Fully Lagrangian modeling of MEMS with thin plates.* IEEE/ASME Journal of Microelectromechanical Systems, 2006. **15**(4): p. 795-810.
38. Wang, B., S. Zhou, J. Zhao, and X. Chen, *Pull-in instability analysis of electrostatically actuated microplate with rectangular shape.* International Journal of Precision Engineering and Manufacturing, 2011. **12**(6): p. 1085-1094.
39. Mohammadi, V., R. Ansari, M.F. Shojaei, R. Gholami, and S. Sahmani, *Size-dependent dynamic pull-in instability of hydrostatically and electrostatically actuated circular microplates.* Nonlinear Dynamics, 2013. **73**(3): p. 1515-1526.
40. Zhao, X., E.M. Abdel-Rahman, and A.H. Nayfeh, *A reduced-order model for electrically actuated microplates.* Journal of Micromechanics and Microengineering, 2004. **14**(7): p. 900-906.
41. Vogl, G.W. and A.H. Nayfeh, *A reduced-order model for electrically actuated clamped circular plates.* Journal of Micromechanics and Microengineering, 2005. **15**(4): p. 684-690.
42. Batra, R.C., M. Porfiri, and D. Spinello, *Reduced-order models for microelectromechanical rectangular and circular plates incorporating the Casimir force.* International Journal of Solids and Structures, 2008. **45**(11–12): p. 3558-3583.
43. Nayfeh, A.H., M.I. Younis, and E.M. Abdel-Rahman, *Reduced-order models for MEMS applications.* Nonlinear Dynamics, 2005. **41**(1-3): p. 211-236.
44. Ahmad, B. and R. Pratap, *Elasto-electrostatic analysis of circular microplates used in capacitive micromachined ultrasonic transducers.* Sensors Journal, IEEE, 2010. **10**(11): p. 1767-1773.
45. Porfiri, M., *Vibrations of parallel arrays of electrostatically actuated microplates.* Journal of Sound and Vibration, 2008. **315**(4): p. 1071-1085.
46. Srinivas, D., *Electromechanical Dynamics of simply-supported micro-plates.* International Journal of Computational Engineering Research, 2012. **2**(5): p. 2012.

47. Vogl, G.W. and A.H. Nayfeh. *A reduced-order model for electrically actuated clamped circular plates*. in *ASME 2003 International Design Engineering Technical Conferences and Computers and Information in Engineering Conference*. 2003. American Society of Mechanical Engineers.
48. Younis, M.I. and A.H. Nayfeh, *Simulation of squeeze-film damping of microplates actuated by large electrostatic load.* Journal of Computational and Nonlinear Dynamics, 2007. **2**(3): p. 232-241.
49. Faris, W.F., *Nonlinear dynamics of annular and circular plates under thermal and electrical loadings (PhD Dissertation).* https://vtechworks.lib.vt.edu/handle/10919/11100, 2003.
50. Asghari, M., *Geometrically nonlinear micro-plate formulation based on the modified couple stress theory.* International Journal of Engineering Science, 2012. **51**: p. 292-309.
51. Gholipour, A., H. Farokhi, and M.H. Ghayesh, *In-plane and out-of-plane nonlinear size-dependent dynamics of microplates.* Nonlinear Dynamics, 2014. **79**(3): p. 1771-1785.
52. Mukherjee, S., Z. Bao, M. Roman, and N. Aubry, *Nonlinear mechanics of MEMS plates with a total Lagrangian approach.* Computers & Structures, 2005. **83**(10): p. 758-768.
53. Zand, M.M. and M. Ahmadian, *Vibrational analysis of electrostatically actuated microstructures considering nonlinear effects.* Communications in Nonlinear Science and Numerical Simulation, 2009. **14**(4): p. 1664-1678.
54. Fu, Y. and J. Zhang, *Active control of the nonlinear static and dynamic responses for piezoelectric viscoelastic microplates.* Smart Materials and Structures, 2009. **18**(9): p. 095037.
55. Karimzade, A., H. Moeenfard, and M.T. Ahmadian. *Nonlinear Analysis of Pull-In Voltage for a Fully Clamped Microplate With Movable Base*. in *ASME 2012 International Mechanical Engineering Congress and Exposition*. 2012. American Society of Mechanical Engineers.
56. Farokhi, H. and M.H. Ghayesh, *Nonlinear dynamical behaviour of geometrically imperfect microplates based on modified couple stress theory.* International Journal of Mechanical Sciences, 2015. **90**: p. 133-144.
57. Ghayesh, M.H. and H. Farokhi, *Nonlinear dynamics of microplates.* International Journal of Engineering Science, 2015. **86**: p. 60-73.
58. Rahaeifard, M., M. Ahmadian, and K. Firoozbakhsh, *Vibration analysis of electrostatically actuated nonlinear microbridges based on the modified couple stress theory.* Applied Mathematical Modelling, 2015.
59. Vangbo, M., *An analytical analysis of a compressed bistable buckled beam.* Sensors and Actuators A: Physical, 1998. **69**(3): p. 212-216.
60. Ouakad, H.M. and M.I. Younis, *The dynamic behavior of MEMS arch resonators actuated electrically.* International Journal of Non-Linear Mechanics, 2010. **45**(7): p. 704-713.
61. Krylov, S., B.R. Ilic, D. Schreiber, S. Seretensky, and H. Craighead, *The pull-in behavior of electrostatically actuated bistable microstructures.* Journal of Micromechanics and Microengineering, 2008. **18**(5): p. 055026.

62. Ruzziconi, L., A.M. Bataineh, M.I. Younis, W. Cui, and S. Lenci, *Nonlinear dynamics of an electrically actuated imperfect microbeam resonator: experimental investigation and reduced-order modeling.* Journal of Micromechanics and Microengineering, 2013. **23**(7): p. 075012.
63. Celep, Z., *Free flexural vibration of initially imperfect thin plates with large elastic amplitudes.* ZAMM-Journal of Applied Mathematics and Mechanics/Zeitschrift für Angewandte Mathematik und Mechanik, 1976. **56**(9): p. 423-428.
64. Celep, Z., *Shear and rotatory inertia effects on the large amplitude vibration of the initially imperfect plates.* Journal of Applied Mechanics, 1980. **47**(3): p. 662-666.
65. Yamaki, N. and M. Chiba, *Nonlinear vibrations of a clamped rectangular plate with initial deflection and initial edge displacement—Part I: Theory.* Thin-Walled Structures, 1983. **1**(1): p. 3-29.
66. Yamaki, N., K. Otomo, and M. Chiba, *Nonlinear vibrations of a clamped rectangular plate with initial deflection and initial edge displacement—Part II: Experiment.* Thin-Walled Structures, 1983. **1**(2): p. 101-119.
67. Marín, J., N.C. Perkins, and W. Vorus, *Non-linear response of predeformed plates subject to harmonic in-plane edge loading.* Journal of Sound and Vibration, 1994. **176**(4): p. 515-529.
68. Lin, C. and L. Chen, *Large-amplitude vibration of an initially imperfect moderately thick plate.* Journal of Sound and Vibration, 1989. **135**(2): p. 213-224.
69. Ostiguy, G.L. and S. Sassi, *Effects of initial geometric imperfections on dynamic behavior of rectangular plates.* Nonlinear Dynamics, 1992. **3**(3): p. 165-181.
70. Liu, W. and F. Yeh, *Non-linear vibrations of initially imperfect, orthotropic, moderately thick plates with edge restraints.* Journal of Sound and Vibration, 1993. **165**(1): p. 101-122.
71. Alijani, F. and M. Amabili, *Theory and experiments for nonlinear vibrations of imperfect rectangular plates with free edges.* Journal of Sound and Vibration, 2013. **332**(14): p. 3564-3588.
72. Chen, C.S., W.S. Cheng, and A.H. Tan, *Non-linear vibration of initially stressed plates with initial imperfections.* Thin-Walled Structures, 2005. **43**(1): p. 33-45.
73. Chen, C.S. and C.Y. Hsu, *Imperfection sensitivity in the nonlinear vibration oscillations of initially stressed plates.* Applied mathematics and computation, 2007. **190**(1): p. 465-475.
74. Huang, H., *Large-Amplitude Vibration of Imperfect Rectangular, Circular and Laminated Plate with Viscous Damping (PhD Dissertation).* http://scholarworks.uno.edu/td/1924/, 2014.
75. Sundararajan, P. and S. Noah, *Dynamics of forced nonlinear systems using shooting/arc-length continuation method—application to rotor systems.* Journal of vibration and acoustics, 1997. **119**(1): p. 9-20.
76. Nayfeh, A.H. and B. Balachandran, *Applied nonlinear dynamics: analytical, computational and experimental methods*. 2008: John Wiley & Sons.
77. Nayfeh, A.H. and D.T. Mook, *Nonlinear oscillations*. 2008: John Wiley & Sons.
78. Nayfeh, A.H. and P.F. Pai, *Linear and nonlinear structural mechanics*. 2008: John Wiley & Sons.

79. Ventsel, E. and T. Krauthammer, *Thin plates and shells: theory: analysis, and applications*. 2001: CRC press.
80. Salmon, R., *Practical use of Hamilton's principle.* Journal of Fluid Mechanics, 1983. **132**: p. 431-444.
81. Mathematica Documentation, *(https://reference.wolfram.com/language/tutorial/NDSolveMethodOfLines.html#1699661144).*
82. COMSOL Multiphysics, *(http://www.comsol.com).*
83. Lobitz, D., A. Nayfeh, and D. Mook, *Non-linear analysis of vibrations of irregular plates.* Journal of Sound and Vibration, 1977. **50**(2): p. 203-217.
84. Nayfeh, A.H., M.I. Younis, and E.M. Abdel-Rahman, *Dynamic pull-in phenomenon in MEMS resonators.* Nonlinear Dynamics, 2007. **48**(1-2): p. 153-163.
85. Alsaleem, F.M., M. Younis, and L. Ruzziconi, *An experimental and theoretical investigation of dynamic pull-in in MEMS resonators actuated electrostatically.* Microelectromechanical Systems, Journal of, 2010. **19**(4): p. 794-806.
86. Nayfeh, A.H. and M.I. Younis, *Dynamics of MEMS resonators under superharmonic and subharmonic excitations.* Journal of Micromechanics and Microengineering, 2005. **15**(10): p. 1840.
87. Younis, M. and A. Nayfeh, *A study of the nonlinear response of a resonant microbeam to an electric actuation.* Nonlinear Dynamics, 2003. **31**(1): p. 91-117.
88. Leissa, A.W., *Vibration of plates*. Nasa Sp-160. 1969, Washington, Springfield: National Aeronautics and Space Administration ;National Technical Information Service. 353 p.
89. Warburton, G., *The vibration of rectangular plates.* Proceedings of the Institution of Mechanical Engineers, 1954. **168**(1): p. 371-384.
90. Caldersmith, G. and T.D. Rossing, *Determination of modal coupling in vibrating rectangular plates.* Applied Acoustics, 1984. **17**(1): p. 33-44.
91. Waller, M.D., *Vibrations of free rectangular plates.* Proceedings of the Physical Society. Section B, 1949. **62**(5): p. 277-281.
92. Saghir, S., M. Bellaredj, A. Ramini, and M. Younis, *Initially curved microplates under electrostatic actuation: theory and experiment.* Journal of Micromechanics and Microengineering, 2016. **26**(9): p. 095004.
93. Grove, T.T., M.F. Masters, and R.E. Miers, *Determining dielectric constants using a parallel plate capacitor.* American Journal of Physics, 2005. **73**(1): p. 52-56.
94. Polytec, *(http://www.polytec.com/us/products/vibration-sensors/microscope-based-systems/msa-500-micro-system-analyzer).*

APPENDIX

Mode Shapes and in-Plane Shape Functions

The COMSOL Multiphysics FEM software [82] has been used for the extraction of mode shapes and the in-plane displacement shape functions. Towards this, we first performed a mesh convergence test. The FEM model consists of a square plate of side length $100\mu\mathrm{m}$ and thickness of $2\mu\mathrm{m}$. Figure A-1 shows the convergence of the first natural frequency with increasing the number of elements. We conclude from the figure that using a mapped mesh with 100 elements along each side of the square microplate is a reasonable compromise between accuracy and computational effort, since further increase of accuracy comes at much higher computational cost.

In Figure A-2 are shown the in-plane shape functions ψ_u and ψ_v. These shape functions are extracted using the FEM software COMSOL [82]. A square microplate is deflected by applying a uniform transverse pressure. Then the in-plane displacements $u(x,y)$ and $v(x,y)$ are extracted when the deflection at the center of the plate is nearly equal to half the thickness of the microplate. We normalize these displacements to use as shape functions ψ_u and ψ_v to be used in the model IV. Next the eigenvalue problem of the linear undamped square microplate was solved. The first six non-dimensional frequencies $\lambda = \omega a^2\sqrt{\frac{\rho}{D}}$ of the symmetric-symmetric mode shapes are given in Table A-1 and corresponding mode shapes are shown in Figure A-3.

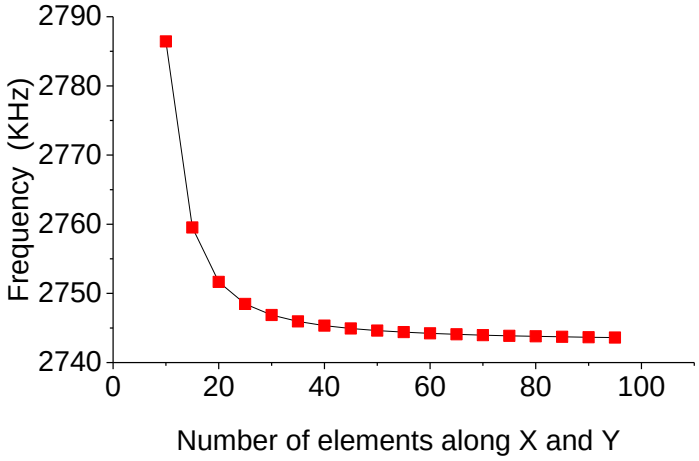

Figure A- 1: Mesh convergence study; convergence of the first natural frequency with increasing the number of elements.

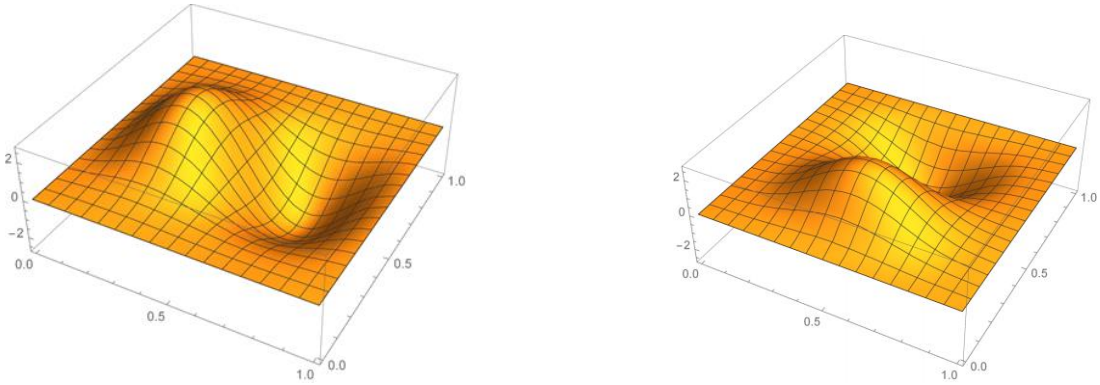

(a) (b)

Figure A- 2: In-plane displacement shape functions for model IV, (a) $\psi_u(x,y)$, (b) $\psi_v(x,y)$.

Table A- 1: Frequency parameter $\lambda = \omega a^2 \sqrt{\frac{\rho}{D}}$ for first six symmetric-symmetric mode shapes of a square microplate calculated using the FEM software COMSOL.

Mode (ϕ_i)	Non-dimensional frequency parameter, (λ)
ϕ_1	35.89
ϕ_2	130.98
ϕ_3	216.54
ϕ_4	302.87
ϕ_5	383.58
ϕ_6	545.7

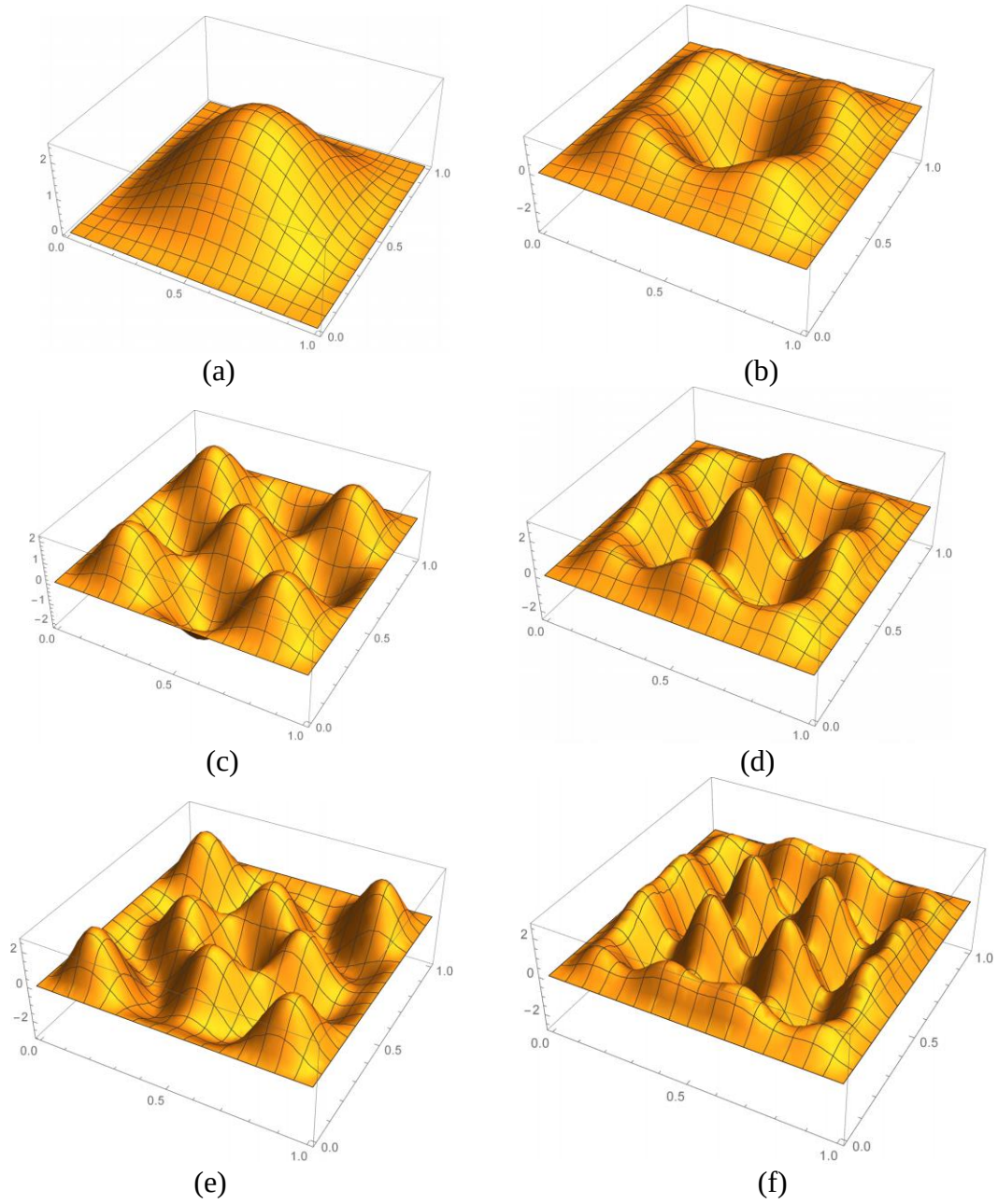

Figure A- 3: The first six symmetric-symmetric transversal mode shapes of a square microplate.